

MASTER OF SCIENCE THESIS

# AN IMPROVED ROTOR DESIGN FOR A DIFFUSER AUGMENTED WIND TURBINE

IMPROVEMENT OF THE DONQI URBAN WINDMILL

F.A. VAN DORST B.ENG

JANUARY 10 2011, DELFT

WIND ENERGY RESEARCH GROUP - FACULTY OF AEROSPACE ENGINEERING – DELFT UNIVERSITY OF TECHNOLOGY  
SUSTAINABLE ENERGY TECHNOLOGY



MASTER OF SCIENCE THESIS

---

# AN IMPROVED ROTOR DESIGN FOR A DIFFUSER AUGMENTED WIND TURBINE

---

IMPROVEMENT OF THE DONQI URBAN WINDMILL

For obtaining the degree Master of Science in Sustainable Energy Technology at  
Eindhoven University of Technology

F.A. VAN DORST B.ENG

JANUARY 10 2011, DELFT

Graduation Committee:

Chairman:	Prof.dr.drs. G.J.W. van Bussel
Member:	Prof.dr.ir. J.G.M. Kuerten
Member:	Ir. W.A. Timmer
Member:	Ir. B.M. Geurts

Front image taken during tests in OJF

Supervisor DONQI: Ir. K. van der Heijden

WIND ENERGY RESEARCH GROUP - FACULTY OF AEROSPACE ENGINEERING – DELFT UNIVERSITY OF TECHNOLOGY  
SUSTAINABLE ENERGY TECHNOLOGY



*"The answer, my friend, is blowing in the wind..."*

Bob Dylan



## ABSTRACT

The polluting fossil fuels are diminishing and becoming more and more expensive. The trias energetica, Figure 1, states that besides reducing the energy demand and using fossil fuels cleaner, renewable energy technologies are the solution to this problem. One of these renewable energy technologies is small-scale wind energy. The DONQI URBAN WINDMILL is a so-called urban turbine, a small roof mounted wind turbine. Moreover, the DONQI URBAN WINDMILL is a diffuser augmented wind turbine (DAWT), a wind turbine embedded in annular wing shaped diffuser. This diffuser has the function of augmenting the flow through the wind turbine.

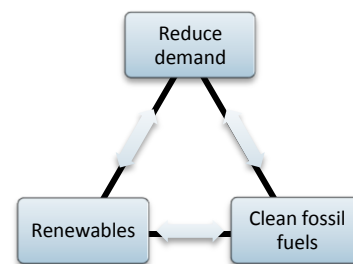


FIGURE 1: TRIAS ENERGETICA

The motivation for this research came from wind tunnel tests done in 2009 by Ten Hoopen for his Master of Science project [1]. He measured a velocity distribution in the diffuser, which was not in agreement with the distribution that was calculated by NLR. Their CFD based calculated velocity distribution provided the basis of the old blade design of the DONQI URBAN WINDMILL. Therefore, the question arose whether an improved blade geometry could be designed for the DONQI URBAN WINDMILL.

The research described in this report deals with the rotor design for such a DAWT, more specific for the DONQI URBAN WINDMILL. In order to get to a full blade design, a fast numerical model was made for which the start off was a 1D axial momentum balance for DAWTs, to obtain the optimal conditions for the design. The optimal rotor loading was comparable to that of a bare turbine. The optimal rotor loading served as a basis for the strength of a vortex cylinder, which was used to represent the rotor blades in the numerical model with an actuator disk. The wake rotation was incorporated by a root vortex. An axisymmetric surface vorticity model calculated the self-induction of the diffuser, the induction of the wake on the rotor and the influences on one another. All together, this provided a tool to obtain the velocity distribution at the optimal rotor loading through a specific DAWT. This velocity distribution was the basis for a developed blade element momentum code that calculated the optimal chord and twist distribution for, in this case, the three bladed rotor. In addition, a linearized blade was obtained from this optimal geometry to reduce significant amounts of material and reduce the production costs. Both types of blades were produced through rapid prototyping followed by aluminum sand-casting to end up with smooth blades that could be tested in a production turbine in the Open Jet Facility of the Delft University of Technology.

Verification of the computational model shows that the developed model resembles the theory well by comparing some runs of the computational model with bare turbine conditions. The validation however shows that only for some conditions the model is comparable to the measurements. It shows that for high solidity rotors the model approximates the measurements well, but for the low solidity rotors the model is quite off. The error is mainly due to replacing the rotor by an actuator disk, to reduce the computational time.

The test results showed that the new blade designs outperformed the old blade in the DONQI URBAN WINDMILL by 15% leading to an increase of annual performance by almost 70%. The measurement results raises to believe a better blade can be designed if the numerical model is developed further. This because the current model provides a velocity distribution that is higher than the actual measured velocity distribution, and thus produces a blade that is not optimized for the real, reduced, velocity distribution.



---

## FOREWORD

---

The awareness of the climate change consequences has increased over the past years. This has resulted in an increase in the demand of sustainable energy solutions, consequently resulting in the development of educational programs on sustainable energy. One of these programs is the Master of Science program in Sustainable Energy Technology at Eindhoven and Delft Universities of Technology which I am enrolled in since 2007. The research described in this report is the final project for my specialization in Wind Energy and results in my graduation.

The research was done for the company DONQI INDEPENDENT ENERGY, a small Dutch company that developed their own wind turbine. The research involved improvement of a commercial product, therefore the work described in this report is confidential and should be treated accordingly. For reproduction of this work, approval of FA van Dorst or DONQI INDEPENDENT ENERGY is required.

---

## ACKNOWLEDGEMENTS

---

I would like to take this opportunity to thank my supervisors of DONQI INDEPENDENT ENERGY, Kasper van der Heijden and Paul ten Hoopen for this interesting research assignment. It would not have been able to finish this project without their assistance during the modeling, the test preparation and the experiments.

From the Delft University of Technology I want to thank Gerard van Bussel and Ben Geurts for their guidance during this project and keeping me on track. My colleagues of the wind energy department I would like to thank as well, since they have all been helpful in his or her own way during my research. The persons whom I owe the succeeding of the experiments to are Stephan Bernardy and Nico van Beek.

The work presented in this paper would not have been possible without my parents who offered me the opportunity for doing a Masters degree, for which I am very grateful. At last, but certainly not the least I want to thank my family, girlfriend and friends for motivating me, standing by me and giving me a great college experience! In special I would like to thank Stephanie, Edward and Jurjen for their assistance with the blade production.

Delft, The Netherlands

F.A. van Dorst B.Eng.

January 10, 2011



---



---

## CONTENTS

---

Abstract.....	7
Foreword.....	9
Acknowledgements.....	9
Contents.....	11
Nomenclature.....	15
1 Introduction.....	17
2 Diffuser augmented wind turbines.....	19
2.1 The donQi Urban Windmill.....	20
2.2 Problem Analysis and Objective.....	21
2.2.1 Project assignment.....	22
2.2.2 Boundary conditions for the blade.....	23
3 Model description.....	25
3.1 DAWT Physics.....	25
3.1.1 Van Bussel.....	25
3.1.2 Werle and Presz.....	28
3.1.3 Jamieson.....	29
3.1.4 Results of the DAWT axial momentum balance.....	29
3.2 Axisymmetric surface vorticity model.....	31
3.3 Full Velocity distribution model.....	32
3.3.1 Geometry.....	33
3.3.2 Modeling the rotor blades.....	34
3.3.3 Self induction of diffuser and Hub.....	35
3.3.4 Vortex cylinder and root vortex induced velocities.....	37
3.4 Blade design Code.....	41
3.5 Model verification.....	43
3.5.1 Velocity verification.....	43
3.5.2 Thrust verification.....	43
3.5.3 Pressure Validation.....	44
3.6 The new rotor blade design.....	45
3.6.1 Velocity distributions.....	45
3.6.2 Blade geometry.....	46
3.6.3 Performance of the new blades.....	48
4 Experiments.....	51
4.1 Experimental set-up.....	51

---

4.1.1	The turbine .....	51
4.1.2	The force measurements .....	52
4.1.3	The velocity measurements.....	54
4.2	Test outline.....	55
4.2.1	Power measurements .....	55
4.2.2	Velocity measurements .....	56
4.3	Blockage corrections .....	57
4.3.1	Nozzle blockage .....	58
4.3.2	Solid blockage.....	59
4.3.3	Collector blockage.....	59
4.3.4	Total blockage .....	59
4.4	Experiment accuracy considerations .....	60
5	Experimental results.....	63
5.1	Performance of the blades .....	63
5.1.1	Power curves old blade .....	63
5.1.2	Power curves optimal blade.....	64
5.1.3	Power Curves linear blade .....	68
5.1.4	PV-Curves of the Three blades .....	70
5.1.5	Annual Estimated Production.....	73
5.1.6	Comparison with numerical model .....	74
5.1.7	Discussion power measurements .....	75
5.2	Model validation.....	78
5.2.1	Force measurements .....	78
5.2.2	Velocity measurements .....	81
5.3	Discussion Experiments.....	89
6	Conclusions and recommendations.....	91
	List of figures .....	95
	List of tables .....	97
	References.....	99
	Appendices .....	103
	Appendix A: Problem of decoupling the diffuser from the rotor design.....	104
	Appendix B: 5 hole pitot tube.....	105
	Appendix C: Axial momentum model for bare turbines .....	107
	Appendix D: Test overview .....	110
	Appendix E: Generator test.....	111

---

Appendix F: More test results ..... 113



## NOMENCLATURE

### Latin symbols

$a$	Axial induction factor	[-]	$q_u$	Uncorrected dynamic pressure	[N/m <sup>2</sup> ]
$A$	Cross sectional area	[m <sup>2</sup> ]	$r$	local radius	[m]
$B$	Number of blades	[-]	$R$	hydraulic radius	[m]
$c$	chord length	[m]	$s$	panel length	[m]
$C_d$	Drag coefficient	[-]	$S$	surface area	[m <sup>2</sup> ]
$C_F$	Force coefficient	[-]	$t$	time of 1 rotation	[s]
$C_l$	Lift coefficient	[-]	$T$	Thrust	[N]
$C_p$	Pressure coefficient	[-]	$u$	induced axial velocity	[m/s]
$C_P$	Power coefficient	[-]	$U$	Axial velocity	[m/s]
$C_T$	Thrust coefficient	[-]	$U_{duct}$	Axial velocity through duct	[m/s]
$D$	Drag	[N]	$v$	induced velocity	[m/s]
$E$	Energy	[J]	$V_{ind}$	Tangential induced velocity	[m/s]
$E(k)$	Elliptic integral of second kind	[-]	$V_{rel}$	Relative wind speed	[m/s]
$F$	Force	[N]	$x$	X-coordinate pivotal point	[-]
$F_{ax}$	Axial force	[N]	$X$	X-coordinate panel	[-]
$F_{tan}$	Tangential force	[N]	$Y$	Y-coordinate panel	[-]
$I$	Coefficient for induced velocities	[-]	$Y$	Y-coordinate pivotal point	[-]
$II(k)$	Elliptic integral of third kind	[-]	<b>Greek symbol</b>		
$K$	integrals	[-]	$\alpha$	Angle of attack	[rad]
$K$	Turbine resistance factor	[-]	$\beta$	Profile slope	[rad]
$K$	Coupling matrix	[-]	$\gamma$	Strength vorticity element	[m/s]
$K(k)$	Elliptic integral of first kind	[-]	$\varepsilon$	area ratio	[-]
$l$	length	[m]	$\varepsilon_c$	Collector blockage	[-]
$L$	Path length vortex	[m]	$\varepsilon_n$	Nozzle blockage factor	[-]
$L$	Lift	[N]	$\varepsilon_s$	Solid blockage factor	[-]
$m$	Mass	[kg]	$\theta_p$	Pitch angle	[rad]
$M$	Momentum	[Ns]	$\theta_T$	Twist angle	[rad]
$\dot{m}$	Mass flow	[kg/s]	$\mu$	back pressure coefficient	[-]
$n$	coefficient for elliptic integrals	[-]	$\rho$	density	[kg/m <sup>3</sup> ]
$n$	rotational speed	[rpm]	$\tau$	Solid blockage constant	[-]
$p$	Pressure	[N/m <sup>2</sup> ]	$\varphi$	Angle of relative wind	[rad]
$P$	Power	[W]	$\Omega$	Rotational speed	[rad/s]
$q_c$	Corrected dynamic pressure	[N/m <sup>2</sup> ]	$\Gamma$	Vortex strength	[m <sup>2</sup> /s]
$Q_s$	Source strength	[m <sup>3</sup> /s]			

**Subscripts**

$\infty$	free stream condition
<i>atm</i>	atmospheric condition
<i>c</i>	induced by vortex cylinder
<i>diffuser</i>	applied on diffuser
<i>gen</i>	generator
<i>hub</i>	applied on hub
<i>in</i>	condition at entrance
<i>ind</i>	induced
<i>kin</i>	kinetic
<i>m</i>	location m
<i>max</i>	maximum value
<i>mech</i>	mechanical
<i>mn</i>	from m to n
<i>n</i>	location n
<i>nozzle</i>	applied on nozzle
<i>out</i>	condition at exit
<i>rotor</i>	condition at rotor
<i>total</i>	force on complete turbine
<i>turbine</i>	applied on turbine
<i>u</i>	uncorrected
<i>wake</i>	condition in the far wake

**Abbreviations**

<i>AEP</i>	Annual estimated production
<i>CFD</i>	Computational fluid dynamics
<i>DAWT</i>	Diffuser augmented wind turbine
<i>GHG</i>	Green house gasses
<i>lin</i>	linear blade
<i>NLR</i>	Nationaal lucht- en ruimtevaartlaboratorium
<i>OJF</i>	Open jet facility
<i>opt</i>	optimal blade

## 1 INTRODUCTION

Sustainable energy solutions can be divided into solutions for large and small-scale applications. Examples of large-scale applications are Megawatt wind turbines, biomass powered power plants and concentrated solar power plants. Small-scale applications can be solar panels, solar collectors and small wind turbines; with a maximum capacity of 100kW.

Small-scale wind energy is becoming more attractive to the public for various reasons. One of them is that the cost of fossil fuel energy became more expensive over the years, Figure 2. This increase in the cost of energy gives an incentive for urban wind energy. Placing a wind turbine near or on top of buildings is considered urban wind energy. When a customer is using the generated electricity directly, he will not have to get this electricity from the grid, whereas if a customer is not able to do this and delivers the generated power to the grid he will receive a financial compensation, which is lower than the cost of energy<sup>1</sup>. Besides, with an own turbine the customer will be less dependent on future price fluctuations in the electricity market [2].

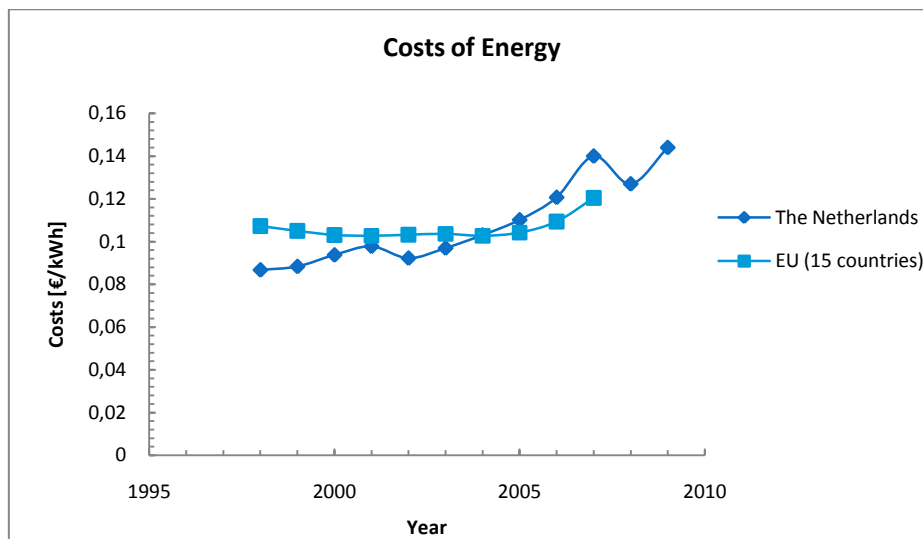


FIGURE 2: COSTS OF ENERGY IN THE NETHERLANDS [3]

Another driver for small-scale wind are the commitments that regional, national and international governments have made to the growth of renewable energy. The European Union has set the 20-20-20 goals; involving a 20% green house gas emission (GHG) reduction and a 20% share of renewable energy generation by 2020 [4]. The Dutch government and the city of Rotterdam have set even higher goals, a GHG reduction of 30% and 50% respectively [5] [6]. Small scale wind can contribute to realizing these targets.

A challenge for urban wind energy are the lower mean wind speeds in the urban environment. This is due to an increased surface roughness of the free stream winds and reduced installation heights of small wind turbines; Figure 3. Next to lower mean wind speeds, the incoming wind will have a higher turbulence intensity. Nevertheless, when well sited the acceleration of flows around buildings can be harvested with the wind turbine. This can yield a 70% power increase in the best case [7].

<sup>1</sup> Example: savings own production in 2010: 23cts/kWh including transport and taxes; compensation is 10,7 cts/kWh=> own production is 12cts more advantageous.

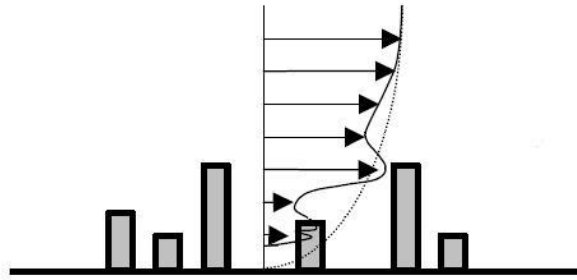


FIGURE 3: WIND DISTRIBUTION URBAN ENVIRONMENT VS GRASS LAND (DOTTED LINE); FIGURE ADAPTED FROM [7]

These opportunities for urban wind energy are translated into a growth of the small-scale wind energy market over the last years [8] [9]; Table 1 and Figure 4. It is expected that the market will grow even further, since the financial crisis is delaying the purchase by customers [9], the fifteen leading manufacturers even predict an exponential growth rate over the coming years [8].

2009 US Sales	2009 Global Sales
20.3 MW	42.5 MW
15% growth over 2008	10% growth over 2008
9,800 units	21,000 units
\$83 million in sales	\$189 million in sales

TABLE 1: US AND GLOBAL SMALL WIND TURBINE SALES IN 2009 [9]

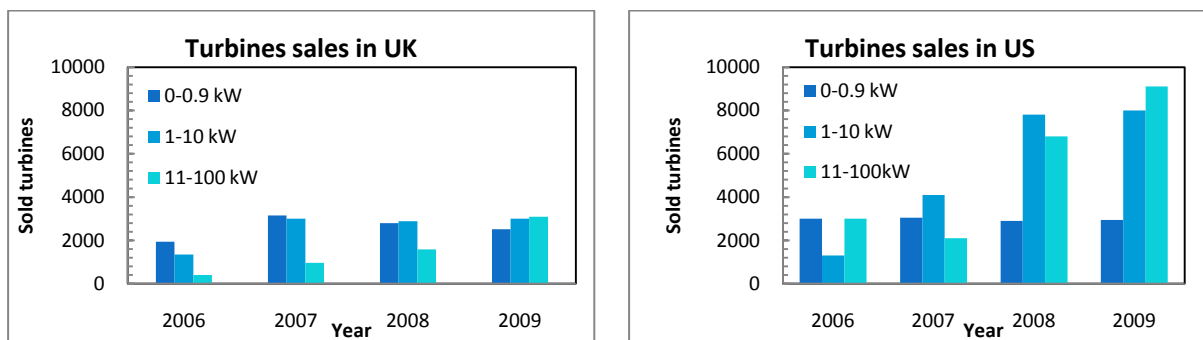


FIGURE 4: UK AND US SMALL WIND TURBINE SALES [8] [9]

The Dutch company DONQI INDEPENDENT ENERGY has jumped into this niche market and developed their small-scale wind turbine, the DONQI URBAN WINDMILL, Figure 5. This wind turbine is a so-called Diffuser Augmented Wind Turbine (DAWT) and is the focus in this research.

A deeper background on DAWTs is given in the next chapter. This chapter provides the research objectives as well. Chapter 3 deals with the developed models required to simulate the flow through the DAWT and design new rotor blades for the DONQI URBAN WINDMILL. The fourth chapter describes the experiments performed in the Open Jet Facility of Delft University of Technology. The results from these tests are presented in the fifth chapter. This thesis will be finalized with the conclusions in the sixth chapter.



FIGURE 5: DONQI URBAN WINDMILL

## 2 DIFFUSER AUGMENTED WIND TURBINES

The performance of wind turbines can be increased by various ways. Phillips [10] describes the various research that has been done on the power augmentation of wind turbines. Examples of the augmentation attempts are the application of tip vanes on the rotor blades, cylindrical obstruction concentrators, diffusers in which the rotor is located and vortex type augmentation devices. Phillips shows that the DAWT exhibits advantages compared to the other augmentation solutions.

Research on DAWTs has started in the 50's when researchers were trying to improve wind turbines. Extensive research has been done in these years by De Vries [11], Igra [12] and Foreman and co-authors [13] [14]. They have developed several models for DAWT's and performed tests with these DAWT's, Figure 6. In the 1980's it was decided that DAWT's were not the future and the research was abandoned.



FIGURE 6: IMPRESSIONS OF DAWT'S; GRUMMAN AEROSPACE, VORTEC 7 AND DONQI URBAN WINDMILL

It took another decade before the research on DAWTs continued, a company in New Zealand, Vortec, build their own turbine and tried to put it into the wind energy market in 1997, Figure 6. Experiments with the Vortec 7 showed a power coefficient,  $C_p$ , of 1.0 over the rotor swept area<sup>2</sup> [10]. This is about the same moment when Van Bussel [15] [16] picked up the research on DAWT's which was reviewed by Hansen [17], Werle and Presz [18] and Jamieson [19] in 2008. More recent work was done by Lawn [20], Ten Hoopen [1] and Widnall [21]. The researchers opt for the use of a diffuser around a wind turbine because of the following aspects:

- Less sensitive to turbulence [10];
- Better spatial coherence [10];
- Better resistant to fatigue [10];
- Same power generation at lower torque [10];
- Lower fluctuating blade loads [11];
- Less sensitive to yaw [11];
- Less noise [11];
- Higher possible rotational speed, so reduced gear ratio [13];
- Reduction of tip losses [12];
- Less noise [22];
- Enhanced mass flow [17] [11];

<sup>2</sup> Maximum theoretical  $C_p$  of a bare turbine is 16/27 [39]

Power extraction by a wind turbine happens at the rotor surface. The power extraction is a result of a pressure drop over the rotor plane, which will cause a force of the rotor on the incoming flow, thrust, Figure 7.

The increase of the mass flow through a DAWT can be explained according to Figure 8 where it is shown that the result of the diffuser is a lift force is exerted on the flow. This lift force is a result of a pressure difference between the upper and lower part of the diffuser, which can be numerically modeled as a ring vortex. With the Biot-Savart law this is coupled to an induced velocity at the rotor plane, yielding an enhanced mass flow [17] [11]. This is described in more detail in paragraph 3.1.

At the trailing edge of the diffuser the wake of the turbine and the external flow will be mixed at sub-ambient pressure, which results into an increase of energy extraction per unit of mass flow, also called the ejector process of the DAWT [10].

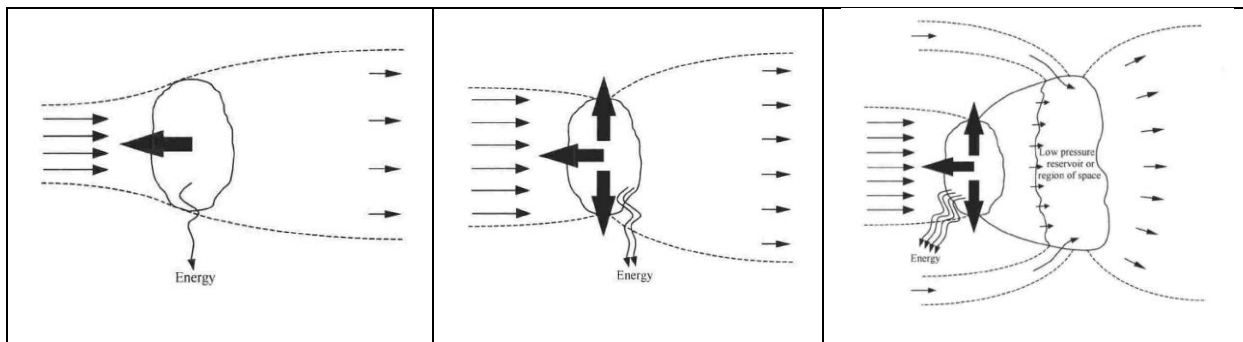


FIGURE 7: BARE WIND TURBINE [23]

FIGURE 8: DIFFUSER [23]

FIGURE 9: EJECTOR [23]

The disadvantage of the use of a diffuser is that it increases the costs of a wind turbine significantly [22]. Other disadvantages that have been mentioned are that its performance is highly affected by environmental conditions [10] and the additional weight and drag at the top of the tower [20].

As will be shown in paragraph 3.1 the gain in power of a DAWT is a function of the area ratio of the diffuser exit area and the energy extraction area, the external shape and the inlet contraction [10]. To obtain the highest performance each trick to avoid flow separation in the diffuser is allowed according to [13].

## 2.1 THE DONQI URBAN WINDMILL

Van der Heijden has developed the DONQI URBAN WINDMILL [24], Figure 5, since his solar panels did not deliver sufficient power to cover his (low) domestic energy demand. Since there was no qualitative satisfying small wind turbine available on the Dutch market, he decided to build his own turbine, the first prototype of the DONQI URBAN WINDMILL. In cooperation with NLR<sup>3</sup> [25] [26], DONQI started developing the turbine in 2008. The wind energy department of Delft University of Technology also assisted in developing the turbine by allowing students to graduate on the DONQI URBAN WINDMILL. DONQI has sold turbines in various countries and is on the verge of upscaling their production to be able to meet demands. Before upscaling they would like to know whether they designed and developed an optimal turbine.

<sup>3</sup> Nationaal Lucht- en Ruimtevaartlaboratorium, National Aerospace Laboratory

Several wind tunnel tests are done in the past with the DONQI URBAN WINDMILL [22] [1]. The tests show discrepancies between measured data and CFD-calculated data used to design the DONQI URBAN WINDMILL. This gives rise to the question whether the design can be improved. The research described in this thesis is focused on the rotor design of a DAWT with the DONQI URBAN WINDMILL as a reference, to increase the power output of this type of wind turbines and develop a fast numerical design tool to arrive at an improved rotor blade.

The DONQI URBAN WINDMILL is a DAWT with an annular wing as a diffuser, with the suction side pointed inwards so the lift force is directed inwards. This lift force is a result of the circulation around the annular wing, caused by the pressure difference between the pressure and suction side<sup>4</sup>. This circulation contributes to an increase of the velocity through the duct according to the Biot-Savart law. The outer ring is equipped with a gurney flap to enhance the bound vorticity, which will lead to an increase in the local velocity, reduce the static pressure, which leads to an increase in the performance of the DAWT. Table 2 gives an overview of some of the specifications of the turbine.

<b>Rated power [kW]</b>	1.75
<b>Maximum power [kW]</b>	2.25
<b>Rated wind speed [m/s]</b>	12.5
<b>Cut-in wind speed [m/s]</b>	2,5
<b>Cut-out wind speed [m/s]</b>	30
<b>Blades</b>	3 Nylon glass fiber reinforced
<b>Rotor diameter [m]</b>	1.5
<b>Diffuser diameter [m]</b>	2
<b>Design tip speed ratio</b>	6.2 (based on free stream)

TABLE 2: SPECIFICATION DONQI URBAN WINDMILL

## 2.2 PROBLEM ANALYSIS AND OBJECTIVE

The motivation for the current study of a rotor blade design for the DONQI URBAN WINDMILL is based on comparing the two graphs in Figure 10. Both graphs show the normalized axial velocity at the rotor position for an empty diffuser. The red-square marked curve is based on CFD calculations of the NLR [26] and is the basis of the old rotor design. The other velocity distribution is obtained from wind tunnel tests by Ten Hoopen. This plot shows there is a strong discrepancy between the two graphs. It is obvious that the augmentation was highly overestimated by the NLR CFD-calculations. This is the motivation to argue the old blade design and develop an improved design. The blade element forces are depending on the incoming velocities and are the basics of designing the geometry of a blade. So whenever the augmentation effect is overestimated, the predicted forces turn out to be higher, so a slender blade than required was designed by NLR. Therefore, it is expected that the newly designed blades, based on the correct velocity distribution will be thicker than the original blades.

<sup>4</sup> Kutta Joukowski

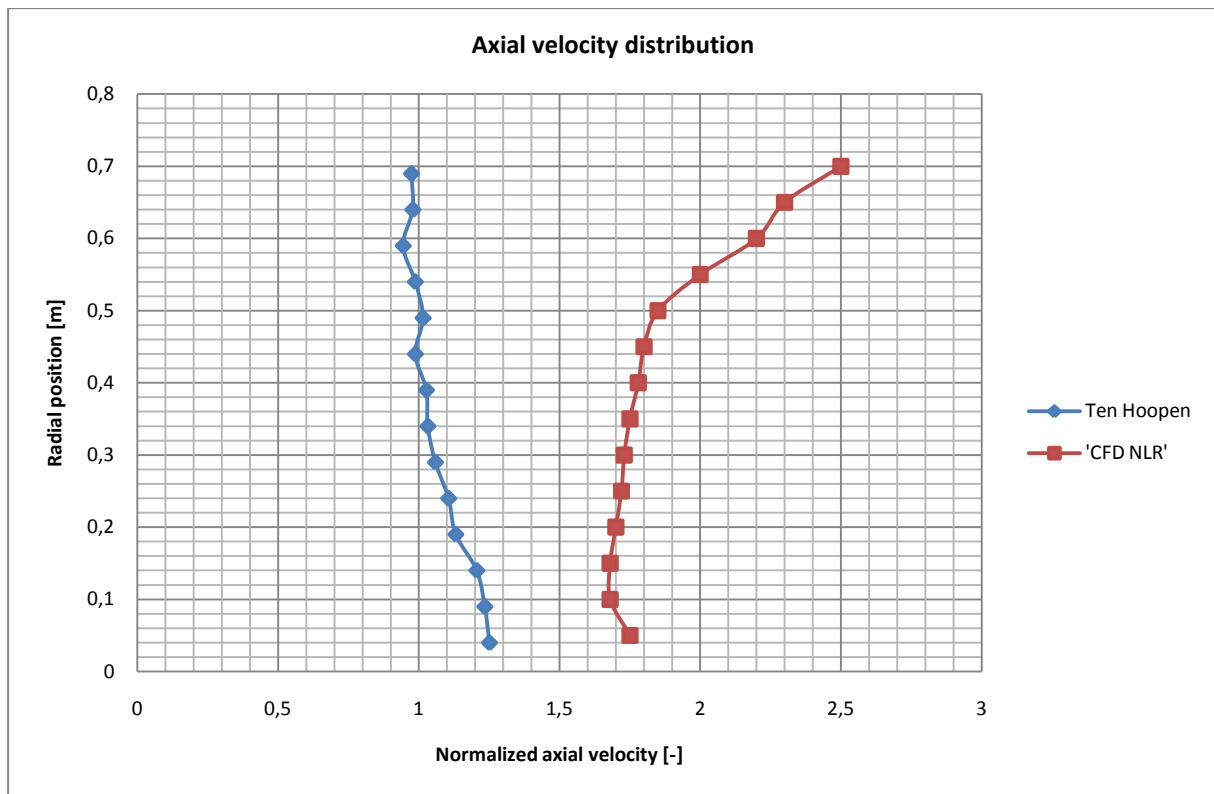


FIGURE 10: AXIAL VELOCITY AT THE ROTOR POSITION [26] AND ADAPTED FROM [1]

In this sense, the following research question was defined:

*"How to design an improved rotor for the DONQI URBAN WINDMILL?"*

An answer to this question was found by:

1. Developing a fast numerical design tool. This tool incorporates the diffuser and rotor interaction.
2. Designing two new blades for the existing diffuser of the DONQI URBAN WINDMILL.
3. Building and testing of these new blades in the Open Jet Facility of the Delft University of Technology.

---

### 2.2.1 PROJECT ASSIGNMENT

---

The title of this research assignment is:

*AN IMPROVED ROTOR DESIGN FOR THE DONQI URBAN WINDMILL*

This title already suggests that it is possible to develop a method that will lead to an improved rotor design for the DONQI URBAN WINDMILL. Based on the graphs in Figure 10 it can be stated that an improved design can be achieved, resulting in higher power output.

---

## 2.2.2 BOUNDARY CONDITIONS FOR THE BLADE

---

The boundary conditions set by DONQI INDEPENDENT ENERGY are:

- The new blade design will lead to a higher power output.
- A tip clearance of 1.5cm; the distance between blade tip and surface of diffuser. The tip clearance was tested in earlier wind tunnel tests by DONQI INDEPENDENT ENERGY. A tip clearance of 1.5cm showed the highest power output.
- A maximum blade thickness of 7mm. Since a NACA 2207 airfoil is used, this leads to a maximum chord length of 10cm. This restriction is due to the production method of the blades: they are injection molded, and if the mold is 7mm thick it can solidify faster and the mold can be filled in one go.
- The rotor is located at 25cm from the leading edge of the diffuser.
- The design should be esthetical appealing as well. For this, two type of blades will be designed, an optimal one and a blade that looks more appealing.
- The rotor length is 67cm when taking the tip clearance and the hub into account.
- The numerical model should be a fast design code.



### 3 MODEL DESCRIPTION

To be able to design a new blade for the DONQI URBAN WINDMILL a numerical model is created. This model calculates the velocity distribution on the rotor plane. These velocities influence the forces on the rotor blade, leading to an optimal blade geometry.

The input parameters come from an axial momentum balance, the velocity distribution is calculated using an axisymmetric surface vorticity model and the blade dimensions are calculated with a blade element momentum method. These three models are dealt with successively in this chapter. The last paragraph is devoted to the blade design and its production.

#### 3.1 DAWT PHYSICS

The physics described in literature on DAWTs often is based on the axial momentum model developed for bare turbines, which can be found in appendix C. The axial momentum theory for a DAWT is presented in this paragraph.

Several momentum theories have been developed for DAWTs. This chapter will deal with some of them and in more detailed with the ones that form the basis of the numerical model developed in this report. For all the theories isentropic flow was assumed.

##### 3.1.1 VAN BUSSEL

A figure of the control volume for the DAWT momentum theory assists in explaining the other theories.

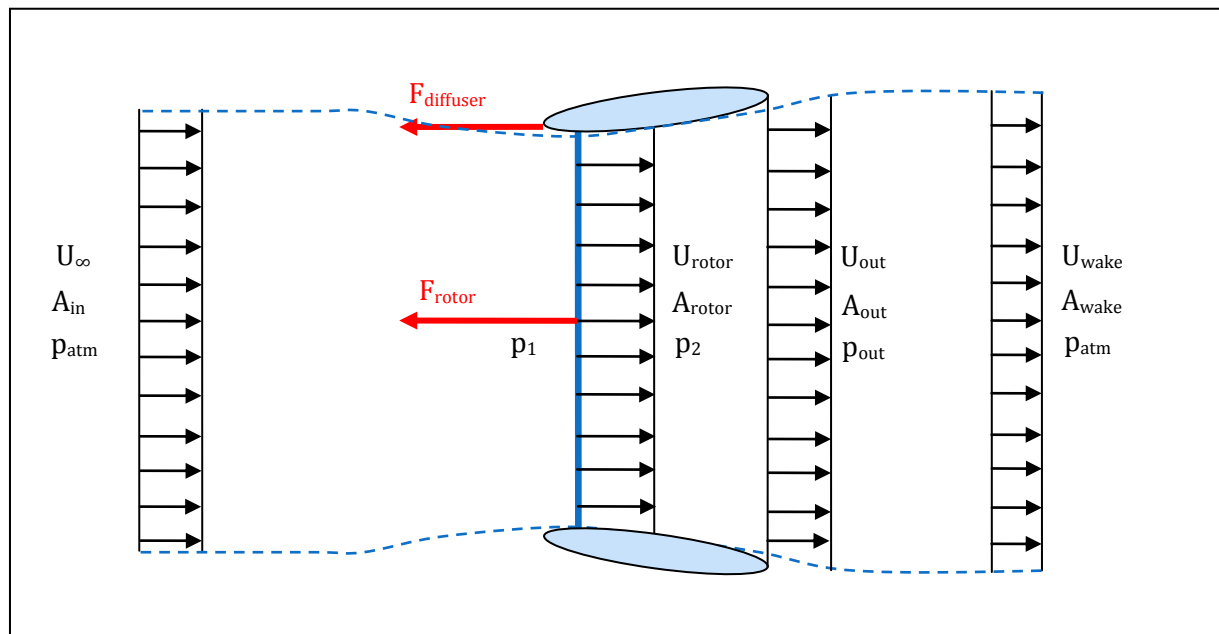


FIGURE 11: CONTROLE VOLUME AS USED BY VAN BUSSEL AND WERLE&PRESZ

Van Bussel [15] [16] starts off with the continuity equations for an empty diffuser:

$$U_\infty A_{in} = U_{rotor} A_{rotor} = U_{out} A_{out} \quad \text{EQUATION 3.1}$$

$$U_{rotor} = \frac{A_{out}}{A_{rotor}} U_{out} = \varepsilon U_{out} \quad \text{EQUATION 3.2}$$

In which

$$\varepsilon = \frac{A_{out}}{A_{rotor}} \quad \text{EQUATION 3.3}$$

The pressure at the rotor location, without including any back pressure ( $U_{in} = U_{out}$ ), according to Bernoulli, is equal to:

$$p_{tot} = p_1 + \frac{1}{2} \rho (\varepsilon U_{\infty})^2 = p_{atm} + \frac{1}{2} \rho (U_{\infty})^2 \quad \text{EQUATION 3.4}$$

$$p_1 = p_{atm} + \frac{1}{2} \rho U_{\infty}^2 - \frac{1}{2} \rho (\varepsilon U_{\infty})^2 = p_{atm} + (1 - \varepsilon^2) \frac{1}{2} \rho U_{\infty}^2 \quad \text{EQUATION 3.5}$$

So whenever the area ratio,  $\varepsilon$ , is bigger than 1, an under pressure will exist at the rotor plane. By taking a back pressure coefficient into account to correct for the fact that the velocity at the diffusers exit is not equal to the undisturbed velocity, yields:

$$U_{out} = \mu U_{\infty} \quad \text{EQUATION 3.6}$$

The velocity at the diffuser exit and the undisturbed velocity are not equal since the flow is not flowing in just an axial direction out of the diffuser, but has radial components, since continuity applies. Combining Equation 3.6 and Equation 3.5 gives:

$$p_1 = p_{atm} + (1 - \mu^2 \varepsilon^2) \frac{1}{2} \rho U_{\infty}^2 \quad \text{EQUATION 3.7}$$

When including a rotor in the analysis, the velocity relations change. The velocity at the diffusers exit will be reduced compared to the undisturbed velocity and the velocity in the wake will even be further reduced. Comparing this to the bare turbine case, Van Bussel introduces an axial induction factor and defines the velocity at the exit of the diffuser as:

$$U_{out} = U_{\infty}(1 - a) \quad \text{EQUATION 3.8}$$

Then:

$$U_{wake} = U_{\infty}(1 - 2a) \quad \text{EQUATION 3.9}$$

The pressure drop at the exit of the diffuser caused by the rotor can be calculated. Including the area ratio and the back pressure coefficient results in:

$$U_{rotor} = U_{\infty} \mu \varepsilon (1 - a) \quad \text{EQUATION 3.10}$$

Applying Bernoulli's law just in front and behind the rotor yields:

$$p_1 = p_{atm} + (1 - \mu^2 \varepsilon^2 (1 - a)^2) \frac{1}{2} \rho U_{\infty}^2 \quad \text{EQUATION 3.11}$$

$$p_2 = p_{atm} + ((1 - 2a)^2 - \mu^2 \varepsilon^2 (1 - a)^2) \frac{1}{2} \rho U_{\infty}^2 \quad \text{EQUATION 3.12}$$

Subtracting Equation 3.12 from Equation 3.11 gives

$$(p_1 - p_2) = 4a(1 - a) \frac{1}{2} \rho U_{\infty}^2 \quad \text{EQUATION 3.13}$$

So the thrust coefficient for the rotor is:

$$C_{T,rotor} = 4a(1 - a) \quad \text{EQUATION 3.14}$$

This is the same relation as was found for the bare turbine case. This means that the pressure drop is independent of area ratio, back pressure and location in the diffuser.

From Equation 3.13 the power and thrust coefficients can be derived based on the rotor area and the diffuser exit area respectively:

$$C_{P,rotor} = \mu \varepsilon 4a(1 - a)^2 \quad \text{EQUATION 3.15}$$

$$C_{T,total} = \mu \varepsilon 4a(1 - a) \quad \text{EQUATION 3.16}$$

$$C_{P,out} = \mu 4a(1 - a)^2 \quad \text{EQUATION 3.17}$$

The optimal power coefficient can be found with a induction factor of  $\frac{1}{3}$  as holds for the bare turbine case.

A breakdown of the thrust coefficient shows:

$$C_{T,diffuser} = C_{T,total} - C_{T,rotor} = (\mu \varepsilon - 1) 4a(1 - a) \quad \text{EQUATION 3.18}$$

So the optimal rotor loading according to Van Bussel is  $\frac{8}{9}$  and a corresponding diffuser loading of  $\frac{8}{9}(\mu \varepsilon - 1)$ .

### 3.1.2 WERLE AND PRESZ

Werle and Presz [18] developed a comparable momentum theory, but with the influence of the diffuser incorporated by an axial force exerted on the incoming flow,  $F_{diffuser}$ . This means that:

$$\sum M = F_{rotor} + F_{diffuser} \quad \text{EQUATION 3.19}$$

$$\rho A_{rotor} U_{rotor} (U_{\infty} - U_{wake}) = A_{rotor} (p_2 - p_1) + F_{diffuser} \quad \text{EQUATION 3.20}$$

Bernoulli gives:

$$(p_2 - p_1) = \frac{1}{2} \rho (U_{\infty}^2 - U_{wake}^2) \quad \text{EQUATION 3.21}$$

The force on the diffuser can be calculated from the pressure distribution on the duct, which follows from the vorticity distribution, explained in paragraph 3.3.4.2 :

The force on the diffuser can be normalized as follows:

$$C_{F,diffuser} = \frac{F_{diffuser}}{\frac{1}{2} \rho A_{rotor} (U_{wake}^2 - U_{\infty}^2)} \quad \text{EQUATION 3.22}$$

This means that the velocity at the rotor can be found by substituting Equation 3.22 in Equation 3.20 and rewriting Equation 3.21:

$$U_{rotor} = \frac{1}{2} (1 + C_{F,diffuser}) (U_{wake} + U_{\infty}) \quad \text{EQUATION 3.23}$$

When defining the relation between the free stream velocity and the velocity in the wake as:

$$\frac{U_{wake}}{U_{\infty}} = 1 - 2a \quad \text{EQUATION 3.24}$$

This gives

$$U_{rotor} = U_{\infty} (1 + C_{F,diffuser}) (1 - a) \quad \text{EQUATION 3.25}$$

Therefore the axial momentum balance will give:

$$F_{thrust} = \frac{1}{2} \rho A_{rotor} (1 + C_{F,diffuser}) (U_{wake}^2 - U_{\infty}^2) \quad \text{EQUATION 3.26}$$

With induction factors:

$$F_{thrust} = \frac{1}{2}\rho A_{rotor} U_{\infty}^2 (4a(1-a) + C_{F,diffuser}) \quad \text{EQUATION 3.27}$$

The power is then given by:

$$P = \frac{1}{2}\rho A_{rotor} U_{\infty}^3 (4a(1-a)^2 (1 + C_{F,diffuser})) \quad \text{EQUATION 3.28}$$

As can be seen in Equation 3.27 that if there is no diffuser present, this yields the regular equation for the axial momentum balance of a bare turbine ( $C_{F,diffuser}=0$ ). This total thrust is thus equal to the thrust on the diffuser and on the rotor blades. The maximum power is produced again at an induction factor of  $\frac{1}{3}$  yielding a thrust coefficient of  $\frac{8}{9}$  with respect to the rotor area.

---

### 3.1.3 JAMIESON

---

Jamieson [19] decouples the diffuser from the total system. The diffuser is taken into account by assuming an induction factor at zero thrust,  $a_0$ . This decoupling is not ideal, since a diffuser performance is influenced by the thrust exerted by the rotating blades; this is shown in appendix A. He concludes that a DAWT operates optimal at the same circumstances as a bare turbine; with a thrust coefficient of  $\frac{8}{9}$ .

---

### 3.1.4 RESULTS OF THE DAWT AXIAL MOMENTUM BALANCE

---

The three previous paragraphs validate the use of an optimal thrust coefficient of  $\frac{8}{9}$  over the rotor area. This is also backed by Hansen [17]. However recent papers claim that optimal operation conditions occur at lower thrust coefficients [22] [27]<sup>5</sup>. In the latter Konijn has developed a one dimensional flow theory based on the work of Lawn [20] and states that the theories of Van Bussel [15] [16], Werle and Presz [18] and Jamieson [19] are invalid. By doing so he made some mathematical mistakes in the comparison, as well in validating his theory with Lawn's theory. Nevertheless the work of Lawn is applicable if it is assumed that the diffuser exit area ratio is allowed to be as big as possible, there is no back flow and an infinite inflow of air available. In practice this cannot be reached. The reason to work with a lower thrust coefficient is obtaining higher velocities at the rotor plane and lower pressures at the exit plane [20]. As Lawn notes himself, there is a significant difference between theory and practice, and there is a limit to a lower thrust coefficient. He shows Figure 12 in his paper. It shows that for different exit area ratios, diffuser inlet efficiencies and turbine efficiencies there is a certain optimal turbine resistance factor defined as:

$$K = \frac{\Delta p}{\frac{1}{2}\rho U_{rotor}^2} = C_T \left( \frac{U_{\infty}}{U_{rotor}} \right)^2 \quad \text{EQUATION 3.29}$$

---

<sup>5</sup> Not published yet, obtained from F. Jaarsma

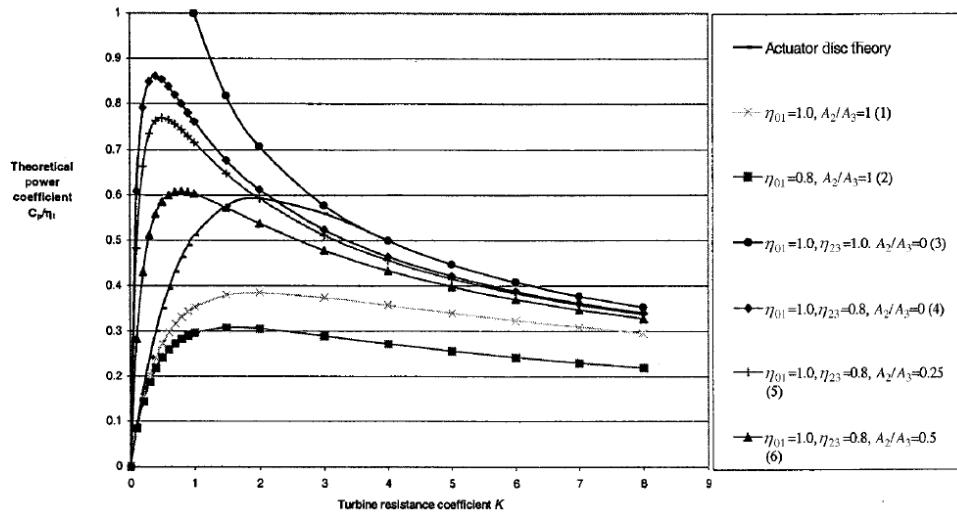


FIGURE 12: MAXIMUM POWER AS FUNCTION OF TURBINE RESISTANCE [20]

Figure 12 shows as well that for lower turbine resistance a higher theoretical power coefficient can be obtained. In the chapter on the tests, a comparison is made between power measurements at different thrust coefficients. Checking the optimal turbine resistance for the DONQI URBAN WINDMILL in Figure 12 with an exit area ratio of 0.75 is about 1.0. Calculating the thrust coefficient with Equation 3.29 and Figure 10 gives an optimal thrust coefficient of 1.2. Based on the fact that multiple literature provide an optimal thrust coefficient of  $\frac{8}{9}$  in consultation with supervisors it was decided to design a rotor blade based on a thrust coefficient of  $\frac{8}{9}$ .

The thrust coefficient is used to model the rotor blades in the full blade design model which is developed in this thesis research. The rotor blades in the DAWT can be replaced by an actuator disk exerting a thrust on the incoming flow. How the actuator disk is modeled in the blade design routine, is shown in the next paragraph.

### 3.2 AXISYMMETRIC SURFACE VORTICITY MODEL

The used model to calculate the velocity distribution on the rotor location as a result of induced velocities by the diffuser, the hub and the wake can be divided into separate parts [28] [1] [21]<sup>6</sup>. At first the self induction of the diffuser and the hub have to be taken into account. The free stream velocity leads to a certain circulation around the diffuser and hub, which induces velocities on the rotor plane. The second part of the model is replacing the rotor blades by an actuator disk, which is modeled as a vortex cylinder in combination with a root vortex, of which the strength depends on the rotor thrust and the incoming velocity. This decreases the computational requirements significantly. The vortex cylinder and the root vortex both induce velocities on the rotor plane, but also on the collocation points of the diffuser.

The basis of the surface vorticity model as developed by Martensen [28] is to cover the body surface with a finite number of surface vorticity panels of unknown strength, Figure 13. On each panel a control point is chosen, to apply the surface flow boundary condition: a Dirichlet boundary condition<sup>7</sup>. The induced velocity at a certain point  $m$ , by a vortex element of length  $l_n$  and strength  $\Gamma_n$  per unit length at a radial distance  $r_{mn}$  is given by the Biot-Savart equation:

$$dv_{mn} = \frac{\Gamma_n dl_n \times r_{mn}}{4\pi r_{mn}^3} \quad \text{EQUATION 3.30}$$

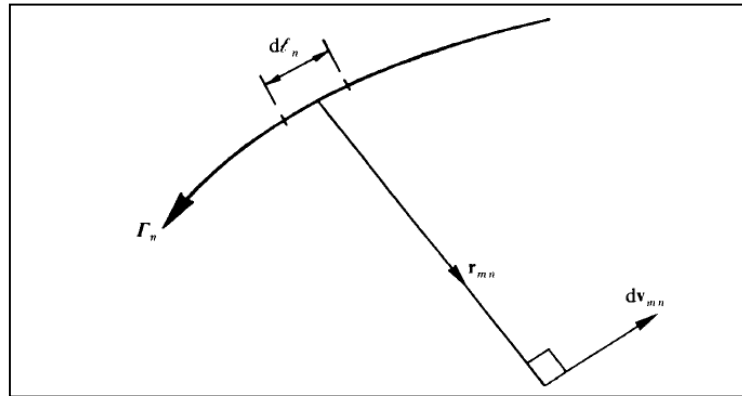


FIGURE 13 BIOT-SAVART LAW

This is the equation that needs to be solved for a single line element. However, the surfaces of the diffuser and hub will be covered with an area density of distributed sheet vorticity elements, with strength  $\gamma_m$ . A general equation that links the free stream velocity  $U_\infty$  to the induced velocity and a velocity discontinuity (first term) is given by Lewis [28]:

$$-\frac{1}{2}\gamma_m + \frac{1}{4\pi} \iint_S \frac{l_m \times ((\gamma_n \times r_{mn}) \times l_m) dS}{r_{mn}^3} + l_m \times (U_\infty \times l_m) = 0 \quad \text{EQUATION 3.31}$$

With this equation the vorticity distributions and the induced velocities can be calculated.

<sup>6</sup> The model is developed by applying the relations given for annular airfoils and ducted propellers, provided by Lewis (chapter 4 and 5).

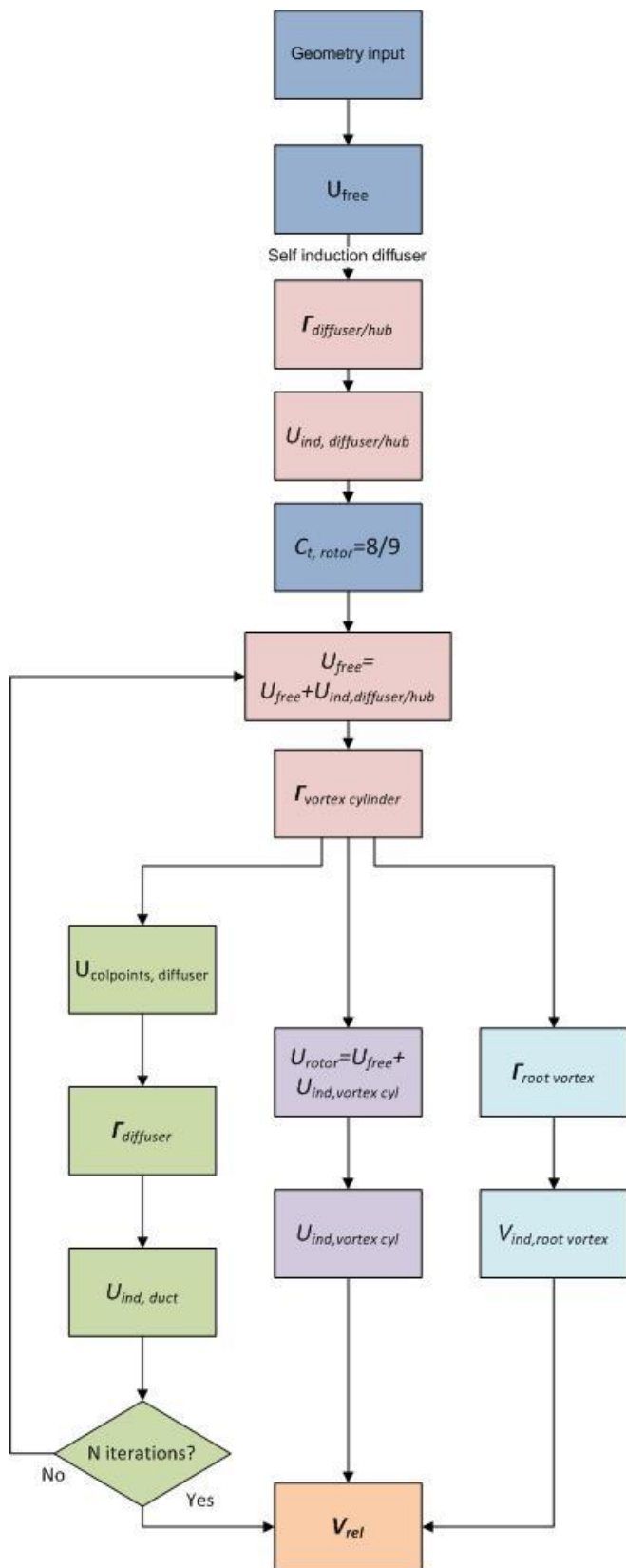
<sup>7</sup> Flow velocity on and parallel to the surface of zero

### 3.3 FULL VELOCITY DISTRIBUTION MODEL

On the right the full potential flow model is shown.

The model starts with the geometry input. In combination with the free stream velocity the vorticity on the diffusers collocation points are calculated, which induce a velocity on the rotor collocation points. Together with a chosen thrust coefficient the strength of the vortex cylinder and the root vortex can be calculated. The induced velocities by the vortex cylinder and the root vortex on the rotor collocation points are calculated. Simultaneously the influence on the diffuser collocation points can be calculated, and from this also the influence of the diffuser and hub on the rotor collocation point is calculated. A new induced axial velocity leads to a new strength of the vortex cylinder and this again to new induced velocities. This process is iterated until convergence is obtained. For this five iteration steps were required.

The rest of this chapter will describe the steps taken to arrive at the final model. Each paragraph will show a part of the models flow chart, to keep track.



### 3.3.1 GEOMETRY

To be able to apply the axisymmetric surface vorticity model first a panel distribution is created over the geometry of the diffuser and the hub. The coordinates have to be moving clockwise around the profiles starting at the leading edge and the last and first point have to be coinciding to obtain a closed profile [28] [21]. Applying this on the diffuser and hub of the DONQI URBAN WINDMILL produces Figure 15, showing the applied mesh of panels.

Geometry input

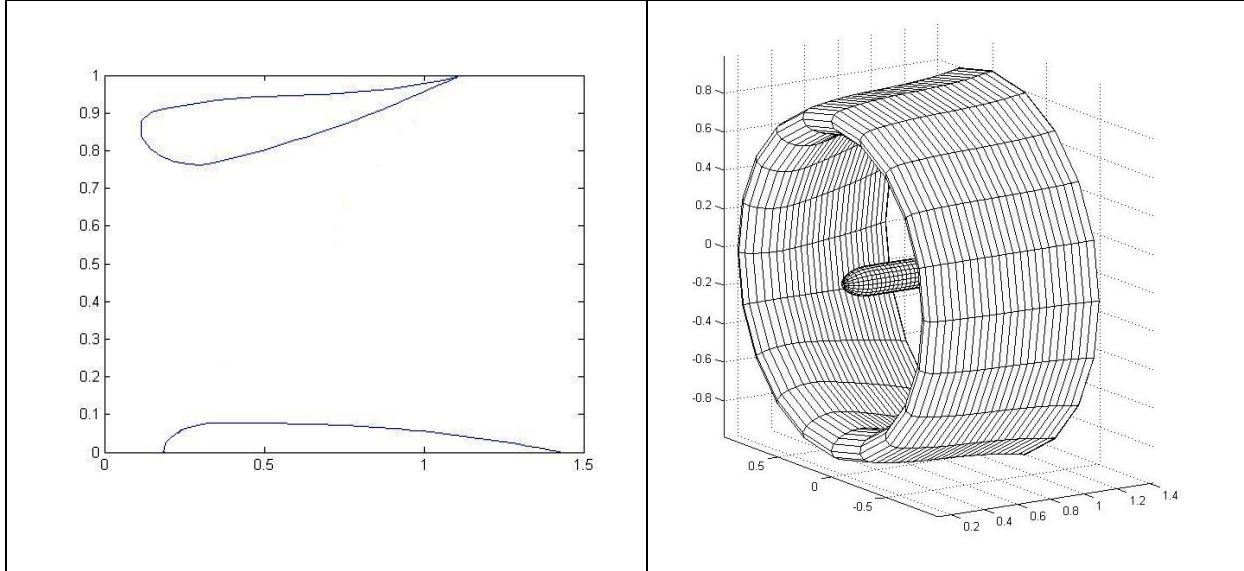


FIGURE 14: DIMENSIONS OF DIFFUSER

FIGURE 15: PANEL DISTRIBUTION DIFFUSER AND HUB

The image in Figure 15 is produced by preparing the geometrical data as panel length, slope and pivotal points.

The panel lengths are calculated with:

$$\Delta s_n = \sqrt{(X_{n+1} - X_n)^2 + (Y_{n+1} - Y_n)^2} \quad \text{EQUATION 3.32}$$

The profile slopes follow from:

$$\arctan \beta = \frac{y_{n+1} - y_n}{x_{n+1} - x_n} \quad \text{EQUATION 3.33}$$

By applying a formula in the model<sup>8</sup>, it is assured that the right quadrant was taken by obtaining the slopes.

The pivotal points of each panel have to be obtained, in which induced velocities and the vorticity strength can be calculated:

$$x_n = \frac{1}{2}(X_{n+1} - X_n) \quad \text{EQUATION 3.34}$$

<sup>8</sup> In Matlab: `atan2(β)`

$$y_n = \frac{1}{2}(Y_{n+1} - Y_n) \quad \text{EQUATION 3.35}$$

With these geometrical data, a coupling matrix can be created, resembling the influence of the pivotal points on one another:

$$K(s_m, s_n) = \frac{(y_m - y_n) \cos \beta_m - (x_m - x_n) \sin \beta_m}{(x_m - x_n)^2 + (y_m - y_n)^2} \quad \text{EQUATION 3.36}$$

Until now a general procedure has been followed for the surface vorticity model. Since in this case the diffuser and the hub are both axisymmetric, a two dimensional approach can be followed. The full equation to be solved corrects for this and is provided in the following paragraphs.

### 3.3.2 MODELING THE ROTOR BLADES

The blades are replaced by an actuator disk, to decrease the computation time. In fact an actuator disk is a combination of a finite amount of blades. These blades are assumed to have a radial uniform bound circulation. The bound vortices are shed from the blade tips, creating helical vortices. Since the actuator disk has a high solidity, so will the vortices, and thus the helical vortices can be combined to an expanding vortex cylinder or a continuous tubular vortex sheet, Figure 16 and Figure 17. Since expansion cannot be modeled by momentum theory, it is assumed to be cylindrical [28] [29].

Geometry input

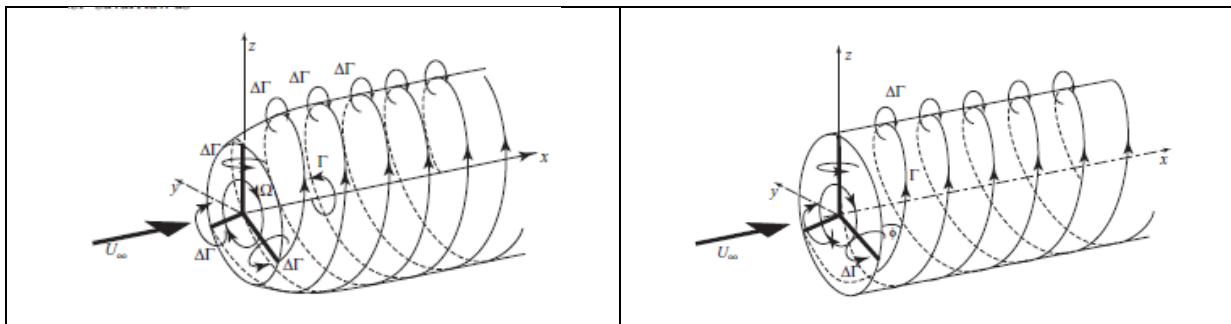


FIGURE 16: REAL MODELING ACTUATOR DISK

FIGURE 17: ACTUAL MODELING ACTUATOR DISK [29]

Lewis developed a procedure for ducted propellers and annular airfoils in which the propellers are modeled by a semi-infinite<sup>9</sup> vortex cylinder emanating from the propeller location. Widnall [21] developed a similar model, but with a vortex cylinder emanating from the trailing edge of the diffuser. In the model both locations were incorporated, a vortex cylinder from the rotor location showed the most satisfying results when it was expanding along the chord of the diffuser in combination with a root vortex, to incorporate the wake rotation. Figure 18 and Figure 19 visualizes the applied vortex cylinder and root vortex configuration.

<sup>9</sup> According to Helmholtz 2<sup>nd</sup> and 3<sup>rd</sup> theorem a vortex tube is of continuous strength and cannot start or end in a fluid

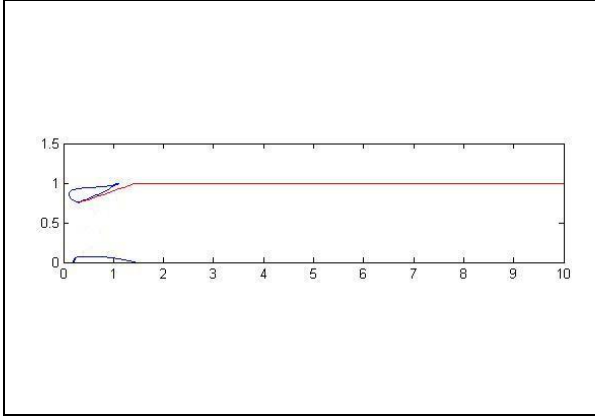


FIGURE 18: 2D VISUALISATION OF VORTEX CYLINDER

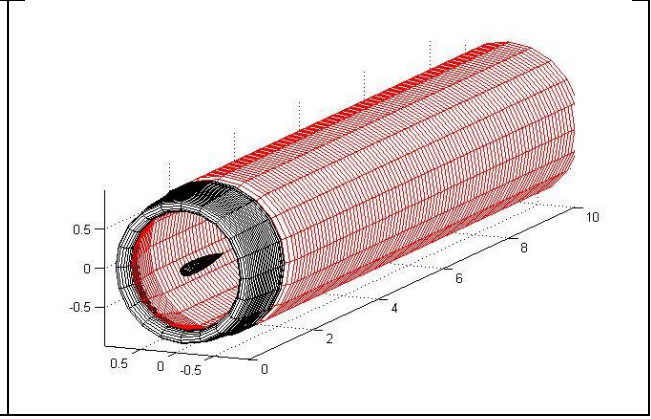


FIGURE 19: 3D VISUALISATION OF VORTEX CYLINDER AND ROOT VORTEX

The strength of the bound vortex is calculated with the velocities that act on the actuator disk as a result of the free stream velocity and the velocity induced by the diffuser and the hub [30] [31] [29]:

$$\Gamma_{\text{vortex cylinder}} = \frac{\pi U_{\text{rotorplane}}^2 C_T}{\Omega} \quad \text{EQUATION 3.37}$$

The strength of the root vortex is equal to the strength of the vortex cylinder.

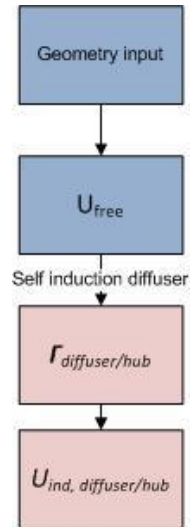
### 3.3.3 SELF INDUCTION OF DIFFUSER AND HUB

All the preparations are taken to start with the actual computational model.

It begins with the flow through an empty diffuser, to be able to calculate the strength of the vortex cylinders, as presented in Equation 3.37.

In the first run of the numerical model, the only velocity influence on the diffuser is that of the free stream. This means that there will be a self-induction of the duct, causing a vorticity around the duct. The strength of this vorticity is calculated with Equation 3.38.

Comparing this equation to the basic equation, Equation 3.31, shows that the free stream velocity has been isolated. The coupling matrix is built up according Equation 3.36, with the order shown in Equation 3.39.



$$K(s_m, s_n) \gamma(s_n) \Delta s_n = -(U_\infty \cos \beta_m) \quad \text{EQUATION 3.38}$$

With  $K$  the influence matrix:

$$K = \begin{bmatrix} K_{hub,hub} & K_{duct,hub} \\ K_{hub,duct} & K_{duct,duct} \end{bmatrix} \quad \text{EQUATION 3.39}$$

In order to create a non-singular matrix, the self induction for airfoil curvature<sup>10</sup>, a back diagonal correction<sup>11</sup> and the Kutta condition<sup>12</sup> have to be taken into account. Relative simple linear algebra can solve Equation 3.38 and provide a value for the vorticity distribution around the diffuser and the hub. This can be then used to calculate the velocities at the rotor plane.

The outcome of the previous equations is a certain vorticity distribution around the duct and hub, which can be used to calculate the velocity field on the rotor plane, as shown in Figure 20.

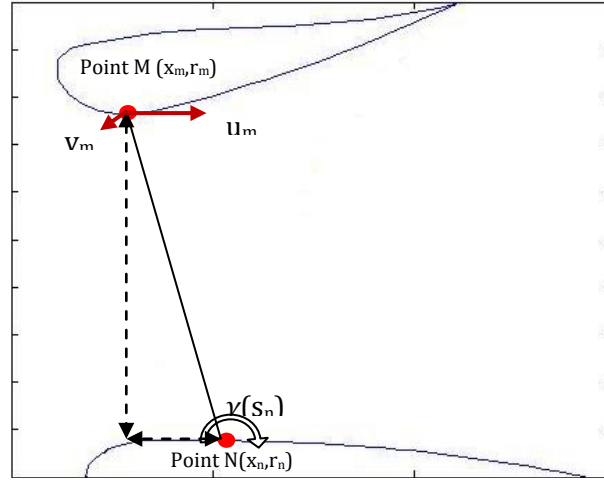


FIGURE 20: CALCULATION OF AXIAL AND TANGENTIAL VELOCITY

The induced velocities can be calculated with:

$$u_{mn} = -\frac{1}{2\pi r_n \sqrt{x^2 + (r+1)^2}} \left[ K(k) - \left( 1 + \frac{2(r-1)}{x^2 + (r-1)^2} E(k) \right) \right] \quad \text{EQUATION 3.40}$$

$$v_{mn} = \frac{x/r}{2\pi r_n \sqrt{x^2 + (r+1)^2}} \left[ K(k) - \left( 1 + \frac{2r}{x^2 + (r-1)^2} E(k) \right) \right] \quad \text{EQUATION 3.41}$$

In these equations  $K(k)$  and  $E(k)$  are the elliptic integrals of respectively the first and second kind. The other variables are:

$$x = \frac{x_m - x_n}{r_n} \quad \text{EQUATION 3.42}$$

$$r = \frac{r_m}{r_n} \quad \text{EQUATION 3.43}$$

<sup>10</sup> Since  $K(s_m, s_m) = 0$

<sup>11</sup> Since  $\gamma(s_m) \Delta s_m = 0$

<sup>12</sup> Since  $\gamma(s_{te}) = -\gamma(s_{te+1})$

$$k = \sqrt{\frac{4r}{x^2 + (r+1)^2}} = \sin\varphi \quad \text{EQUATION 3.44}$$

Solving Equation 3.40 and Equation 3.41 for each of the collocation points on the rotor blades, will give the diffusers induced velocities. So the total velocities on the rotor plane are:

$$U_{rotorplane} = U_{\infty} + u\gamma \quad \text{EQUATION 3.45}$$

And

$$V_{rotorplane} = \Omega r + v\gamma \quad \text{EQUATION 3.46}$$

### 3.3.4 VORTEX CYLINDER AND ROOT VORTEX INDUCED VELOCITIES

The strength of the vortex cylinder and the root vortex is calculated with Equation 3.37. Paragraph 3.1 shows sufficient proof to assume an optimal thrust coefficient of  $\frac{8}{9}$  as a basis for a blade design. The vortex cylinder and the root vortex induce velocities on the rotor collocation points and on the diffuser and hub collocation points. The first part of this paragraph gives the equations for the rotor collocation points and the second part for the diffuser collocation points. The rotor collocation points were chosen more densely distributed at the root and tip, the diffusers collocation points were equally distributed.

#### 3.3.4.1 INDUCED VELOCITIES ROTOR COLLOCATION POINTS

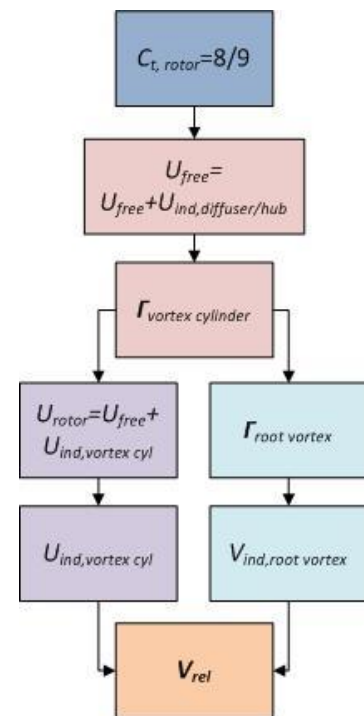
The vortex cylinder induces velocities on the rotor plane and on the diffuser/hub. The induced velocities at the rotor collocation points can be compared with the induction at the rotor plane for a bare turbine. This induction can be calculated with [31] [29]:

$$U_{ind,rotorplane,vortex\ cyl} = \frac{\gamma}{2} \quad \text{EQUATION 3.47}$$

Where:

$$\gamma = \frac{\Gamma}{L} \quad \text{EQUATION 3.48}$$

Where  $L$  is the distance a tip vortex travels in one rotation of the blades.



$$L = U_{rotor}t \quad \text{EQUATION 3.49}$$

$$t = \frac{2\pi}{\Omega} \quad \text{EQUATION 3.50}$$

For a DAWT the velocity at the rotor is equal to the free stream velocity with the velocity induced by the diffuser minus the velocity induced by the vortex cylinder, since for a bare turbine the free stream wind speed is used. This means that this part has to be included in the iteration as well. The velocity distributions at the rotor location can be calculated depending on a certain thrust coefficient [31].

The tangential velocity induced by the wake rotation is not taken into account yet. This is calculated with a root vortex. The strength of the root vortex is equal to the strength of the vortex cylinder [29]. A drawing of the root vortex inducing a velocity on the rotor collocation points is shown in Figure 21.

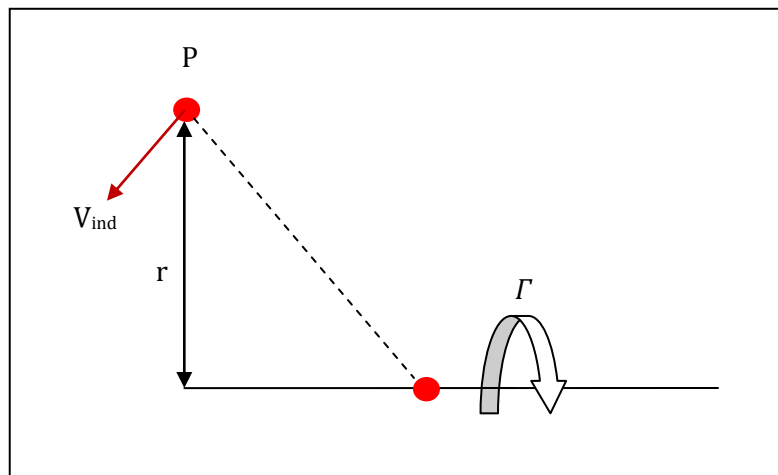


FIGURE 21: ROOT VORTEX

Since it is a straight line vortex, only a tangential velocity will be induced on the rotor plane, which can be calculated with [32]:

$$V_{ind} = \frac{\Gamma}{4\pi r} \quad \text{EQUATION 3.51}$$

### 3.3.4.2 INDUCED VELOCITIES ON DIFFUSER COLLOCATION POINTS

Lewis provides two equations to calculate the induced velocities by the vortex cylinder on the diffuser and hub collocation points. The induced velocities can be calculated with:

$$U_c = \frac{\Gamma}{2\pi} \left[ I + \frac{x}{\sqrt{x^2 + (r+1)^2}} \left( K(k) - \left( \frac{r-1}{r+1} \right) \Pi(n, k) \right) \right] \quad \text{EQUATION 3.52}$$

$$V_c = \left[ \frac{2\Gamma}{\pi k^2 \sqrt{x^2 + (r+1)^2}} \left( E(k) - \left( 1 - \frac{k^2}{2} \right) K(k) \right) \right] \quad \text{EQUATION 3.53}$$

With:

$$\begin{aligned} I &= \pi \text{ if } r < 1 \\ I &= \pi/2 \text{ if } r = 1 \\ I &= 0 \text{ if } r > 1 \end{aligned}$$

And:

$$n = \frac{4r}{(1+r)^2} \quad \text{EQUATION 3.54}$$

In these formulas  $\Pi(n, k)$  is the elliptic integral of the third kind.

There is one problem, since  $\Pi(n, k)$  is singular at  $r=1$ . Lewis shows:

$$\lim_{r \rightarrow 1} \left( \left( \frac{r-1}{r+1} \right) \Pi(n, k) \right) = 0 \quad \text{EQUATION 3.55}$$

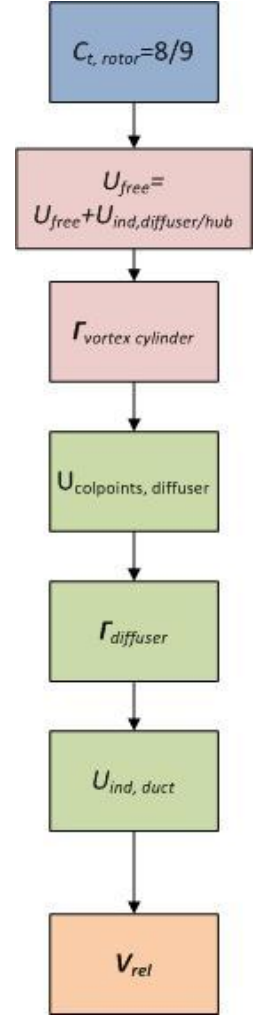
The alternative expression for  $U_c$  in that case is [28]:

$$U_c = \Gamma \left[ \frac{1}{4} + \frac{xK(k)}{2\pi\sqrt{x^2 + 4}} \right] \quad \text{EQUATION 3.56}$$

Like this the influence of the panels of the vortex cylinder on the panels of the diffuser can be calculated, and thus the induced velocities on the diffuser and hub collocation points are found.

From here on the equations used in the previous paragraph can be used with the exception that the first equation, Equation 3.38, changes into:

$$K(s_m, s_n) \gamma(s_n) \Delta s_n = -(U_\infty \cos \beta_m + U_c \cos \beta_m + V_c \sin \beta_m) \quad \text{EQUATION 3.57}$$



Solving Equation 3.57 gives a certain vorticity around the diffuser and with Equation 3.40 and Equation 3.45 the new velocities on the rotors collocation points are found.

If the steps are iterated the final velocity distribution on the rotor plane can be found. The total axial velocity at the rotor plane is equal to:

$$U_{rotor} = U_{\infty} + U_{ind,Diffuser/hub} + U_{ind,vortex\ cyl} \quad \text{EQUATION 3.58}$$

From the vorticity distribution around the diffuser the pressure distribution can be obtained, from which the thrust of the diffuser can be calculated, which can be used for the validation of the model:

$$C_p = 1 - \left( \frac{\gamma(s_n)}{U_{\infty}} \right) \quad \text{EQUATION 3.59}$$

$$C_{t,diffuser} = \oint C_p \cos \beta \, dx \quad \text{EQUATION 3.60}$$

### 3.4 BLADE DESIGN CODE

To able to design a blade from the velocity distribution obtained through the previous described numerical model a Blade Element Momentum (BEM) approach is followed. It comes down to dividing a full blade into  $N$  sections and equating for each of the blade elements the blade element forces to the momentum changes calculated for them. Paragraph 3.1 about the DAWT physics describes how these momentum changes are calculated.

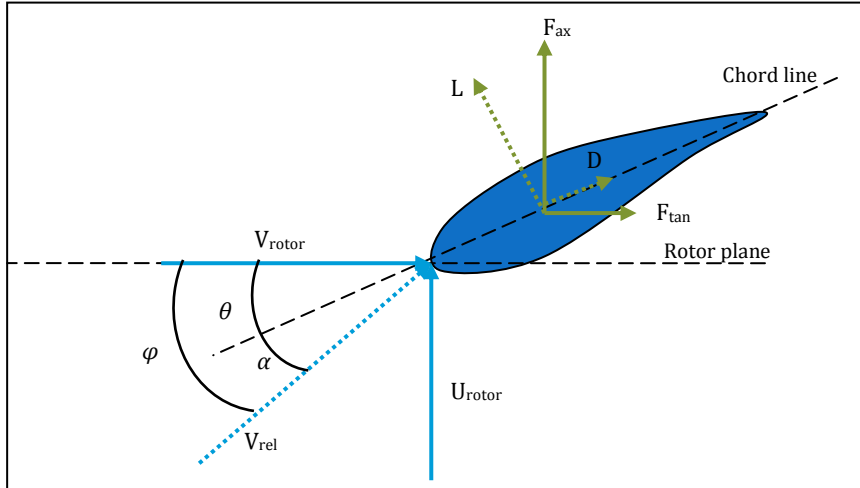


FIGURE 22: BLADE ELEMENT FORCES

Figure 22 shows a blade element with the forces working on it. The incoming free wind speed combined with induced velocities form the rotor velocity,  $U_{rotor}$  acting on the blade element. The rotational speed combined with tangential induced velocities by the wake form the tangential velocity,  $V_{rotor}$ . These two velocities combined form the relative velocity approaching the blade element ( $V_{rel}$ ) which is under an angle  $\varphi$  with the rotor plane. This angle consists of the angle of attack  $\alpha$ , the angle between the relative velocity and the chord line, and the twist and the pitch angle  $\theta$ , the angle between the chord line and the rotor plane.

The combination of the relative velocity and the angle of attack yield a lift and drag force on the blade element.

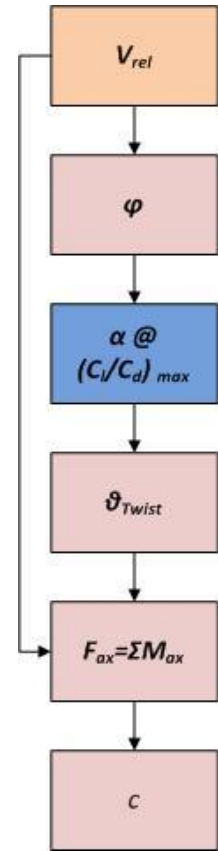
$$dL = C_l \frac{1}{2} \rho V_{rel}^2 c dr \quad \text{EQUATION 3.61}$$

$$dD = C_d \frac{1}{2} \rho V_{rel}^2 c dr \quad \text{EQUATION 3.62}$$

From the lift and the drag force the tangential and axial forces can be calculated.

$$dF_{ax} = dL \cos \varphi + dD \sin \varphi \quad \text{EQUATION 3.63}$$

$$dF_{tan} = dL \sin \varphi - dD \cos \varphi \quad \text{EQUATION 3.64}$$



Since the turbine is a three bladed turbine, the total force on a radial shell is found by multiplying the forces in Equation 3.63 and Equation 3.64 by the number of blades,  $B$ . So the axial force is equal to:

$$dF_{ax} = Bc \frac{1}{2} \rho V_{rel}^2 (C_l \cos \varphi + C_d \sin \varphi) dr \quad \text{EQUATION 3.65}$$

The result from the momentum balance described in paragraph 3.1 is that this axial force is equal to the thrust on the blade.

$$T = \frac{1}{2} \rho C_T U_{rotorplane}^2 A \quad \text{EQUATION 3.66}$$

Per blade element that means:

$$dT = \pi \rho U_{rotorplane}^2 C_T r dr \quad \text{EQUATION 3.67}$$

The wake rotation causes a decrease in wake pressure yielding an additional axial force, which is equal to the increase of the dynamic head [29]. This brings the total axial momentum change to:

$$M_{ax} = \pi \rho r dr (U_{rotorplane}^2 C_T + (2V_{ind})^2) \quad \text{EQUATION 3.68}$$

Equating Equation 3.68 to Equation 3.65 gives a relation to calculate the optimal chord for each blade element:

$$c = \frac{2\pi r}{B} \frac{1}{C_l \cos \varphi + C_d \sin \varphi} \frac{C_T U_{rotorplane}^2 + (2V_{ind})^2}{V_{rel}^2} \quad \text{EQUATION 3.69}$$

In Equation 3.69  $\varphi$  can be calculated since the axial and tangential velocities are known. The lift and drag coefficient are determined by their maximum ratio, also giving the angle of attack for a certain airfoil<sup>13</sup>. With a set pitch angle, the twist angle can be calculated through:

$$\theta_T = \varphi - \alpha_{(C_l/C_d)_{max}} - \theta_P \quad \text{EQUATION 3.70}$$

<sup>13</sup> In this case NACA 2207 with 6% nose drop

### 3.5 MODEL VERIFICATION

The developed numerical model can be verified by comparing obtained velocity distributions with a bare turbine case, by comparing the thrust coefficients of the diffuser and the rotor and by comparing the obtained pressure distributions with pressure measurements by Ten Hoopen [1].

#### 3.5.1 VELOCITY VERIFICATION

The core part in the model is obtaining the velocity distribution at the optimal thrust coefficient. This can serve as verification for the model is well, since the velocity distributions for a bare turbine are known. Expanding the diffusers diameter to infinitely large or reducing the diffusers chord to almost nil and run the model for these configurations yield the velocity distributions displayed in Figure 23 and Figure 24.

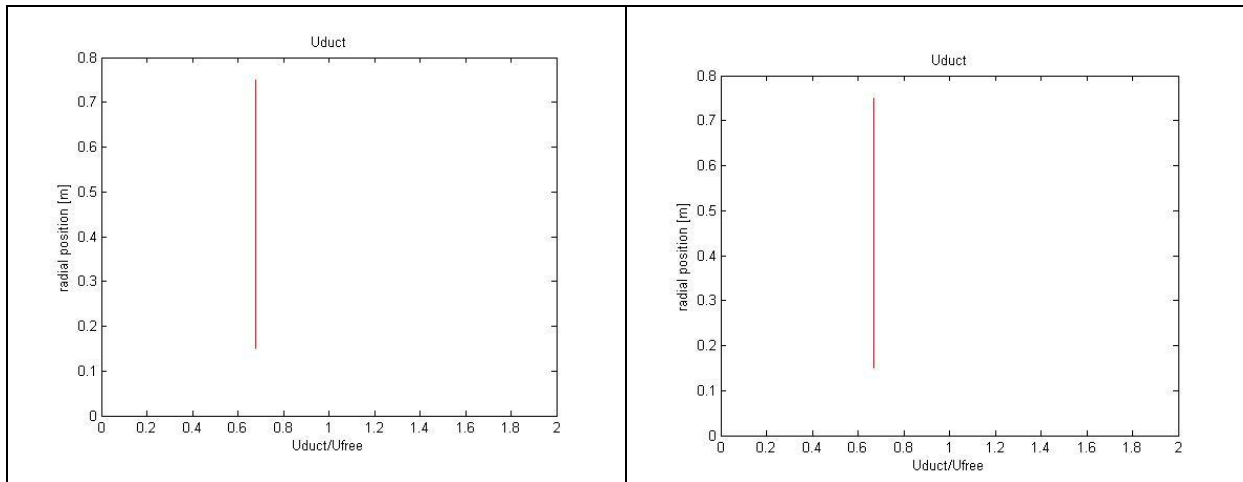


FIGURE 23: VELOCITY DISTRIBUTION WITH INCREASED DIAMETER

FIGURE 24: VELOCITY DISTRIBUTION WITH REDUCED CHORD

It is known from literature that the velocity at the rotor location for a bare turbine is equal to:

$$U_{rotor} = U_{\infty}(1 - a) \quad \text{EQUATION 3.71}$$

When the thrust coefficient is set to its most optimal value,  $\frac{8}{9}$ , at an axial induction factor of  $\frac{1}{3}$ , this gives that the normalized velocity at the rotor plane is equal to  $\frac{2}{3}$ . Both Figure 23 and Figure 24 show this. This is partly a verification of the model.

#### 3.5.2 THRUST VERIFICATION

Another way to check the model is to look at the thrust coefficients of the diffuser and the rotor respectively. They should have about the same value [15] [1]. The thrust coefficient on the rotor

is an input value, and the thrust coefficient on the diffuser can be calculated with Equation 3.62, this gives Table 3.

$C_{t,rotor}$	0	$\frac{1}{18}$	$\frac{2}{18}$	$\frac{3}{18}$	$\frac{4}{18}$	$\frac{5}{18}$	$\frac{6}{18}$	$\frac{7}{18}$	$\frac{8}{18}$	$\frac{9}{18}$	$\frac{10}{18}$	$\frac{11}{18}$	$\frac{12}{18}$	$\frac{13}{18}$	$\frac{14}{18}$	$\frac{15}{18}$	$\frac{16}{18}$
$C_{t,diffuser}$	0.12	0.19	0.26	0.32	0.39	0.45	0.51	0.56	0.61	0.67	0.72	0.76	0.81	0.85	0.89	0.93	0.97

TABLE 3: THRUST COEFFICIENTS OF ROTOR AND DIFFUSER

Having a close look at Table 3 it can be concluded that the thrust coefficients are in the same order of magnitude, with the force on the diffuser being a bit higher.

### 3.5.3 PRESSURE VALIDATION

Figure 25 shows the pressure distributions over the surface of the diffuser obtained from Ten Hoopen's tests [1] and the numerical model respectively. The pressure distributions are for a case without a rotor present in the diffuser. The figure shows that both graphs have the same trend, however the measured pressure distribution shows a strong peak at 0.3 chord, this is mainly caused by a silencer which is installed in the diffuser of the DONQI URBAN WINDMILL, and is not fully aligned with the diffusers surface, creating a peak in the  $C_p$ -graph. Due to this bump in the diffuser, the flow will separate resulting a sudden pressure increase. When looking at the trailing edge, the model and the measurements show a discrepancy, however the overall picture shows that the model is quite good at simulating the real world.

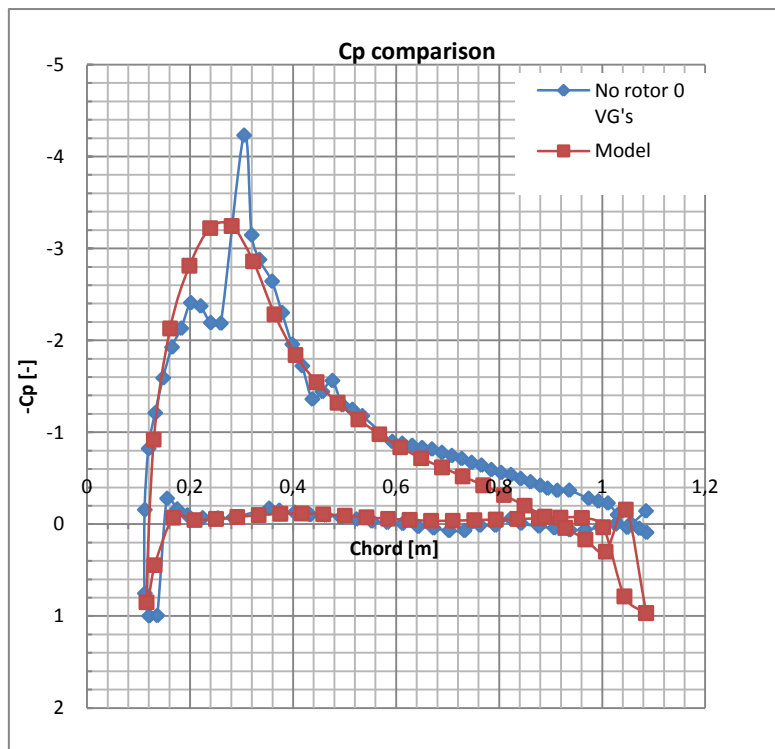


FIGURE 25: CP VERIFICATION

The provided figures in this paragraph provides sufficient support that the developed model will calculate the correct velocity distribution in the diffuser at the rotor location.

### 3.6 THE NEW ROTOR BLADE DESIGN

With the numerical model provided in paragraph 3.2 to 3.5 the velocity distributions are calculated and the blade geometry can be found. This paragraph starts with the obtained velocity distributions. The velocity distributions are the basis of the new blade geometry, which will be provided in this paragraph as well.

#### 3.6.1 VELOCITY DISTRIBUTIONS

The velocity distributions are obtained from the model described in paragraph 3.2. Figure 26 shows the induced velocities which are acting on the collocation points of the rotor. The total velocities acting on the rotor collocation points are the shown velocities increased with the free stream velocity and the rotational speed to obtain the axial and tangential velocities respectively.

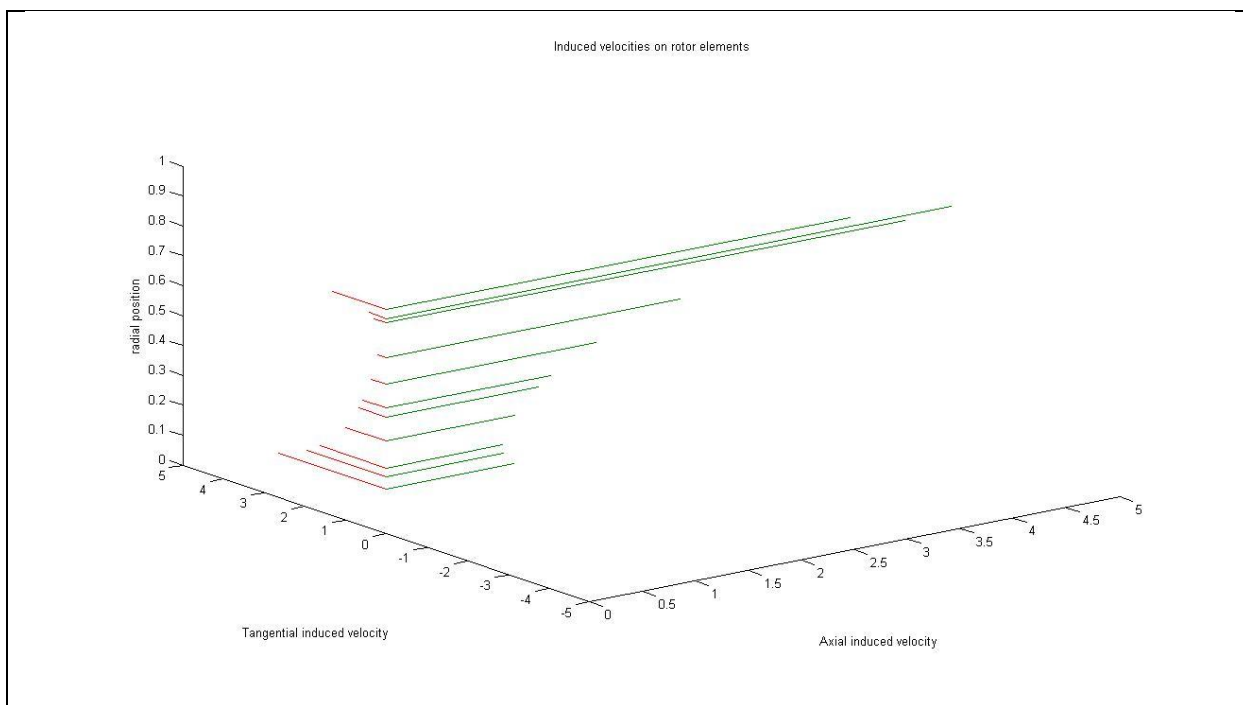


FIGURE 26: INDUCED VELOCITIES, TANGENTIAL(RED) AND AXIAL (GREEN)

The normalized axial velocity distribution at the optimal thrust coefficient of  $\frac{8}{9}$  is shown in Figure 27. For different thrust coefficients the velocity distribution is displayed in the graph. At zero thrust, an empty diffuser, the first line on the right is obtained, increasing the thrust results in a shift to the left, ending at a thrust coefficient of  $\frac{8}{9}$  for the red line. As coming closer to the diffuser wall the velocity is increasing, which is in accordance with Hansen [17], stating that the velocities at the diffuser wall should be higher to energize the boundary layer of the diffuser.

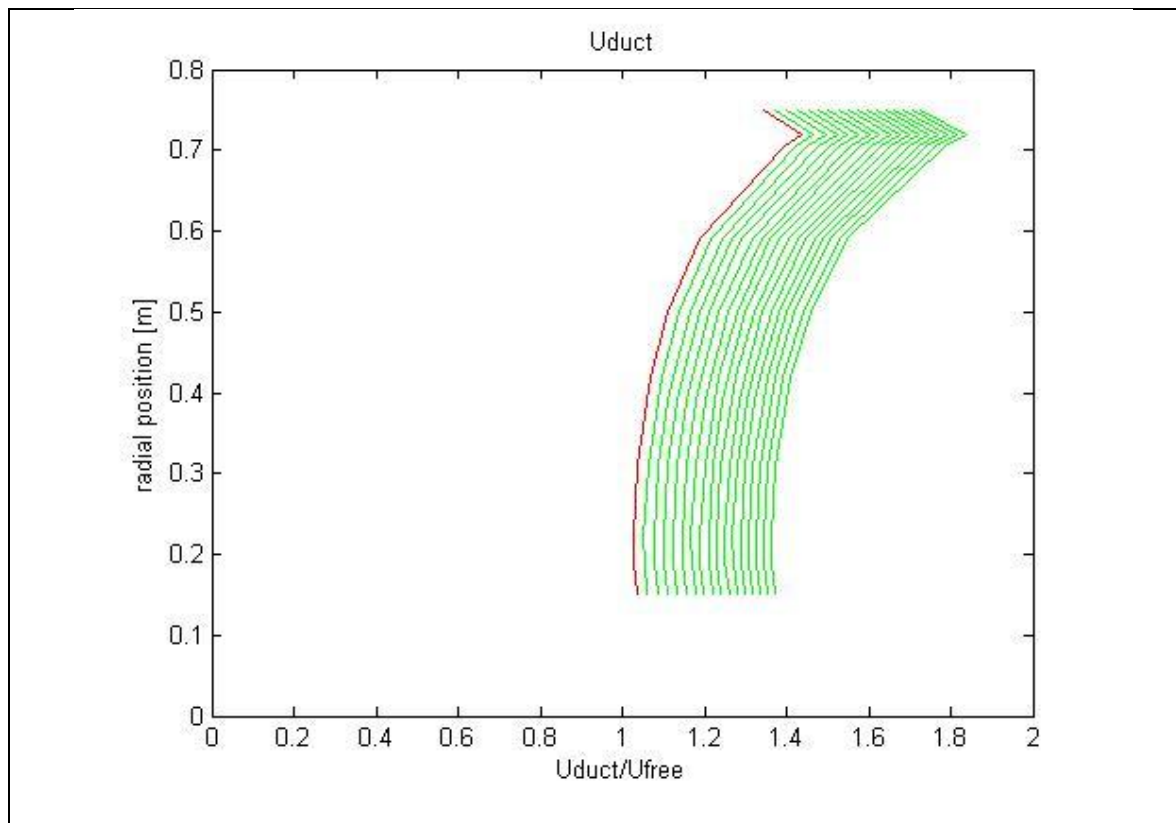


FIGURE 27: AXIAL VELOCITIES ON ROTOR ELEMENTS FOR VARIOUS CT'S

### 3.6.2 BLADE GEOMETRY

The red line in Figure 27 combined with Equation 3.69 and Equation 3.70 provides the optimal blade geometry for the DONQI URBAN WINDMILL. As can be seen in Figure 28, the optimal blade has a very wide root section compared the old blade of the DONQI URBAN WINDMILL, the green line in Figure 28. The increased root section causes some limitations for manufacturing the blade, to reduce these limitations the design was linearized. This was done in consultation with DONQI. Figure 28 shows that the chord length at the root is reduced to 130mm and at the blade tip to 105mm. The blade design starts at 150mm radius in the throat of the diffuser, since the radius of the hub is 150mm. The maximum thickness of the blade has exceeded its boundary condition. Since the extra thickness provided extra power extraction, it was allowed by DONQI, also since they were looking for different production methods.

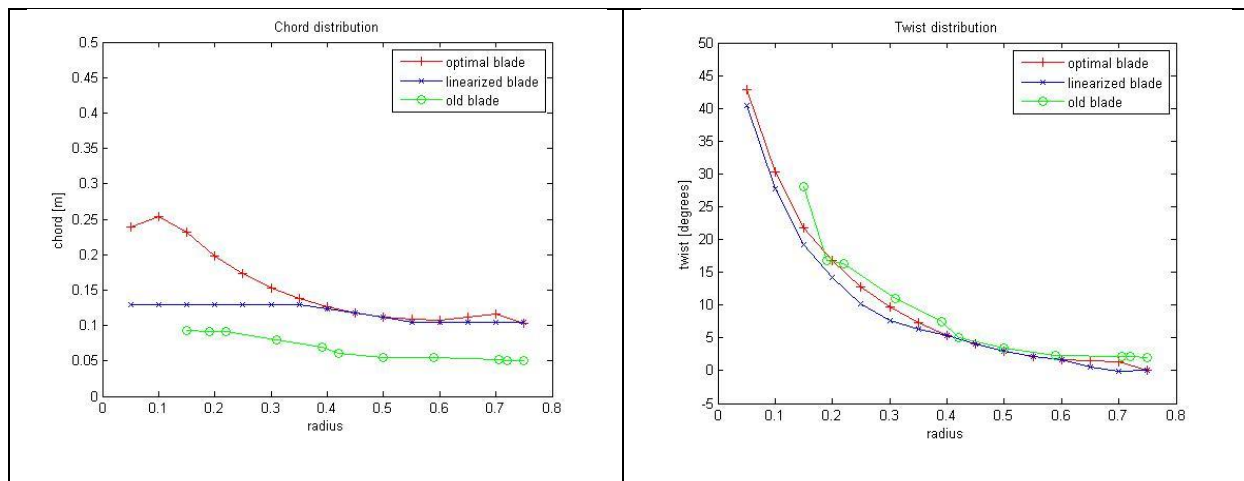


FIGURE 28: CHORD DISTRIBUTIONS

FIGURE 29: TWIST DISTRIBUTIONS

What is very clear is that the new blades are, almost, twice as wide as the old blade used in the DONQI URBAN WINDMILL. Having a glance at Figure 10 and comparing that to Figure 27 can explain this. The axial velocities are almost twice as low as was calculated with the CFD model of NLR [25], which was the basis of the old blade design. The twist distributions are shown in Figure 29. The twist distribution for the linearized blade is corrected for the reduced chord, to get comparable axial and tangential forces, leading to a reduced twist since the angle of attack has to be increased.

In consultation with the engineers of DONQI it was decided to align the optimal blade at the hub as much as possible, to improve the aesthetics of the blade. Since the model calculated the optimal blade geometry from 50mm radius on, this could be used to enlarge the blade and cut a cylinder through this to obtain a 15mm clearance between the blade and the hub.

To be able to produce the blades for testing them in a wind tunnel, drawings were made in a 3D CAD program, Figure 30. The drawings were obtained by importing the airfoil coordinates from XFOIL as the basis for the shape of each blade element. The blade elements were scaled and rotated according the calculated chord and twist distribution. A smooth connection between the blade elements provided the blade.

The prototypes of the blades were produced by the rapid prototype technique FDM<sup>14</sup>, where a temperature controlled head extrudes thermoplastic material layer by layer. The prototype served as a model to create a sand cast mold. The positive is pressed in two boxes filled with sand, and leaves a negative mold. The mold is filled with aluminum and a sand casted aluminum blade is the result. The surface roughness of the aluminum blade is still too high to test it in the wind tunnel. To achieve a smooth surface on the blades, they were sanded with a grinder, disc blades, sanding paper and steel wool, all with a different roughness. The results of the different stages are shown in Figure 30 till Figure 33. For both type of blades these steps were done.

In these same figures, the hub connection can be seen. This is a plug that will be enclosed in the hub. Since it is a circular plug, the pitch angles of the blade can be adjusted during testing. More about this can be found in the next chapter.

<sup>14</sup> Fused deposition modeling

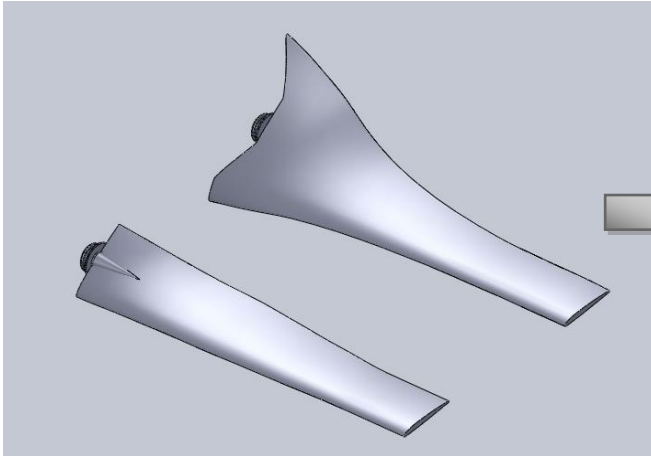


FIGURE 30: 3D CAD DRAWINGS



FIGURE 31: FDM MODEL



FIGURE 32: VARIOUS STAGES IN GRINDING AND SANDING



FIGURE 33: RAW SAND-CASTED BLADE

### 3.6.3 PERFORMANCE OF THE NEW BLADES

With the new blade designs their performance can be calculated as well, to check whether they will perform better than the old blade design. Figure 34 shows these PV-curves. It is clear that the new designed blades significantly outperform the old blade. The data for the old blade were obtained from the tests done by Ten Hoopen in 2009 [1]. As expected, the optimal blade is performing better than the linearized blade. Whether this will hold in the wind tunnel test can be questioned because of the wide chord length at the root, which can cause extra drag on the blade and reduce the power output at higher velocities. Nevertheless, it is clear that the new blades will outperform the old blade design.

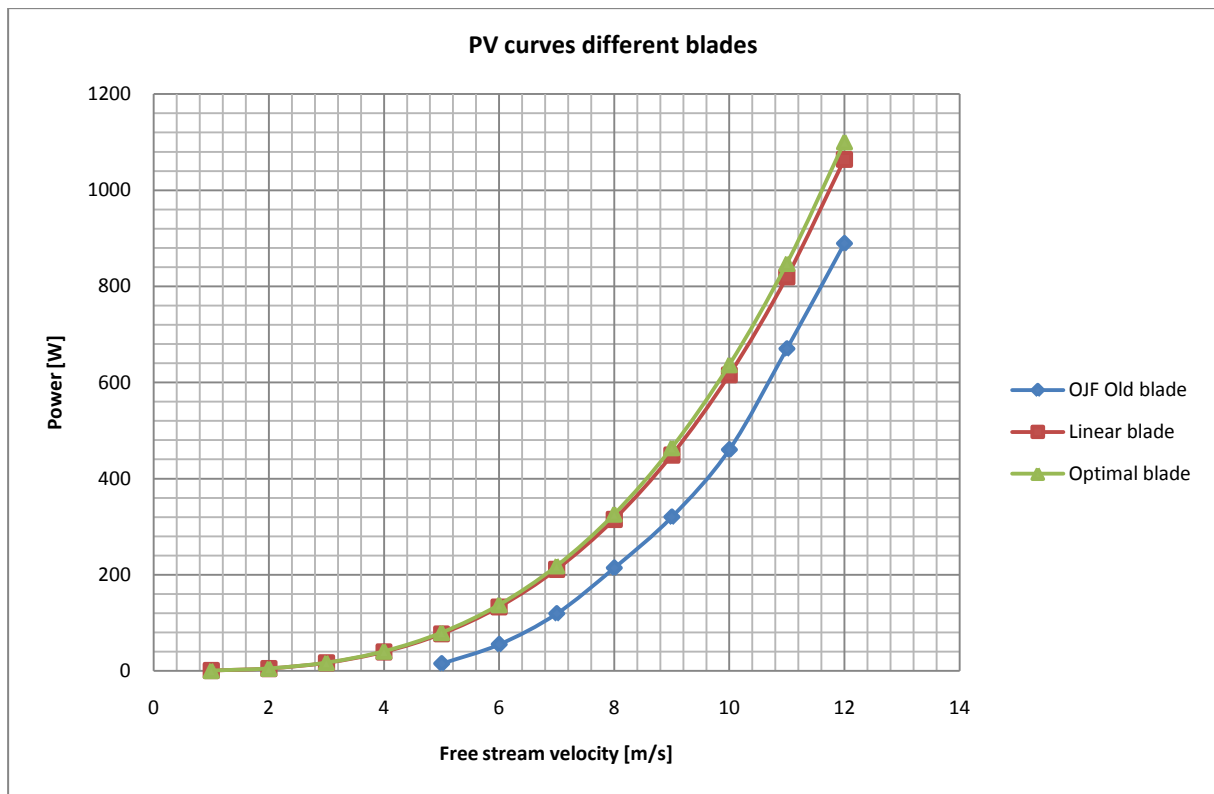


FIGURE 34: PV CURVES OF NEW BLADES

Comparing the power coefficients of the blades with each other shows that the optimal blade has a  $C_p$  of 0.68 and the linear blade of 0.65. The  $C_p$  of the old blade varies from 0.17 to 0.49. Where the  $C_p$  is calculated based on the rotor area and the atmospheric and tested conditions respectively.



## 4 EXPERIMENTS

The designed blades were tested in the Open Jet Facility, OJF, of Delft University of Technology. This wind tunnel has a test section where the full DONQI URBAN WINDMILL can be installed with its old and the new blades mounted.

The tests were done to be able to validate the design procedure and check whether the new designed blades outperform the old blade.

### 4.1 EXPERIMENTAL SET-UP

This paragraph describes the set-up of the experiments that were done to obtain the desired data. Minor adjustments to the hub of the DONQI URBAN WINDMILL were made and custom-made parts were produced.

#### 4.1.1 THE TURBINE

A regular production turbine was used for the tests. Only a new generator was used in the tests, the so called 3D-skewed variation, which should require a lower starting torque. The blades are fixed in the hub by enclosing the plug of the blades in the hub, as shown in Figure 35. The picture shows as well the bolts that are used to fix the blades in a certain pitch angle. By changing the pitch angle and performing power measurements, the optimal pitch angle can be found, and checked whether it is in agreement with the inputs of the numerical model.

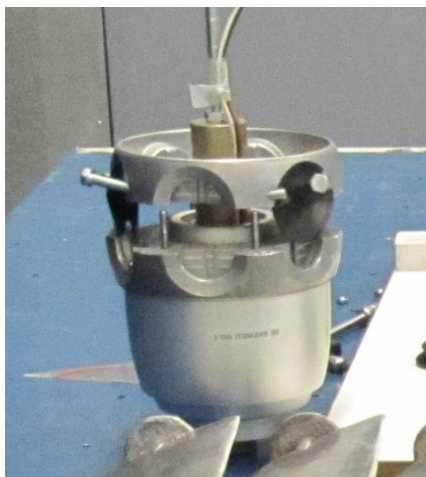


FIGURE 35: GENERATOR AND HUB



FIGURE 36: GENERATOR

The pitch angles could be measured with an aluminum bar connected to the generator, Figure 37. When removing the front cone of the generator, a flat surface is seen, this is used as a reference. The aluminum bar was jointed to the generator with a bolt. The bar had a rectangular cross sectional area, so the sides of the bar could be used to serve as a reference to measure the angle between blade and a surface perpendicular to the rotor swept area. This was done at a fixed radial position with an adjustable angle and a protractor, taking the local twist angle into

account. When the desired pitch angle was found, the bolts were fastened and the blade was fixed, Figure 38.



FIGURE 37: PITCH MEASURING

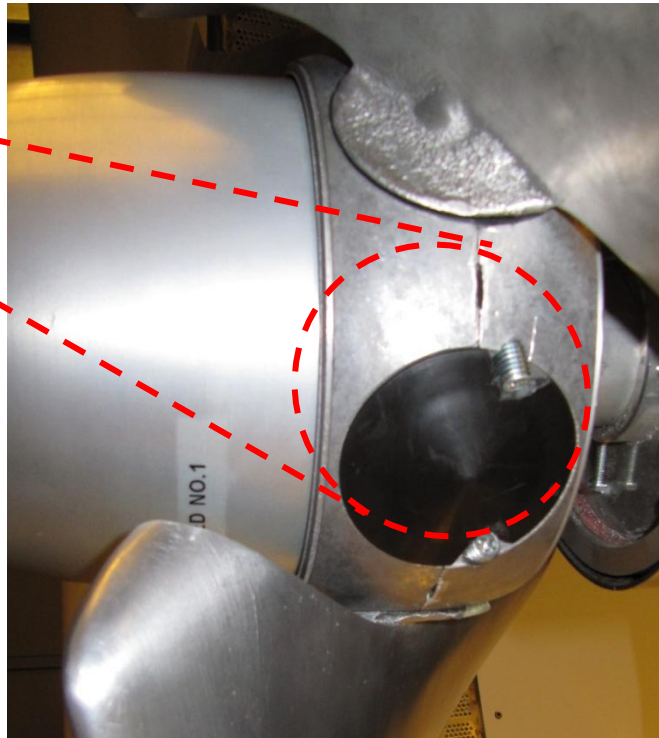


FIGURE 38: SETTING THE PITCH ANGLE

#### 4.1.2 THE FORCE MEASUREMENTS

The axial forces acting on the rotor and on the turbine are measured as well, to be able to check the thrust on the diffuser and on the blades. The thrust on the blades was measured with a custom-made tool. An aluminum tube was slid over the stator shaft of the generator, as shown in Figure 36. A 1mm aluminum sheet is clamped between two busses, which are bolted to the tube. The busses are glued and bolted to the sheet. Gluing prevails shear displacement, allowing the aluminum sheet only to have an axial displacement. In the outer side of the sheet similar busses are mounted and riveted to the hub, so the generator is connected to the hub. On the last aluminum sheet strain gauges are attached, which can measure the axial displacement. When well calibrated with standard weights and an amplifier it can be linked to axial forces. This is shown in Figure 39 and Figure 40.



FIGURE 39: BUILT UP THRUST MEASUREMENT

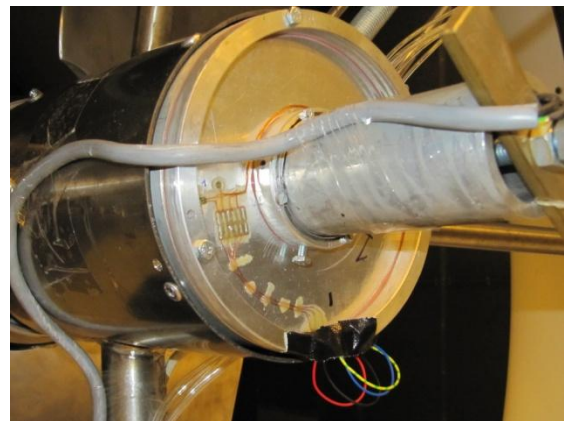


FIGURE 40: THRUST MEASUREMENT

The total thrust on the turbine is measured with a custom-made scale. The scale is comparable to a hammock chair. The turbine is installed on a steel frame, which hangs in another frame, linked to each other by thin steel strips, enabling the turbine to swing almost frictionless in axial direction. On the rear side of the steel frame on which the turbine is installed, a load cell is installed, which can measure the total axial force. See Figure 41 and Figure 42.

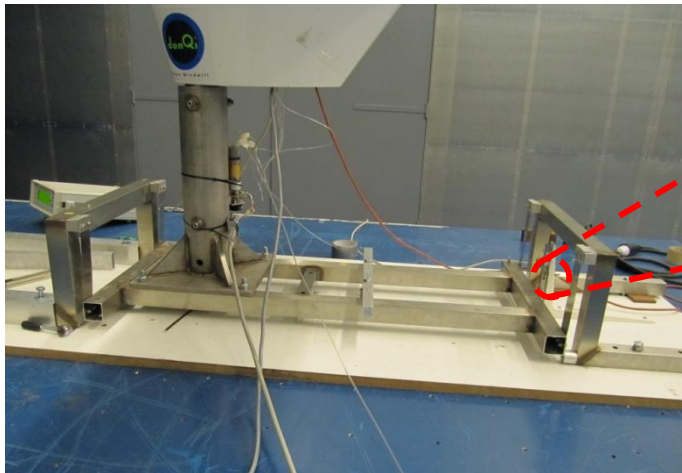


FIGURE 41: THE HAMMOCK

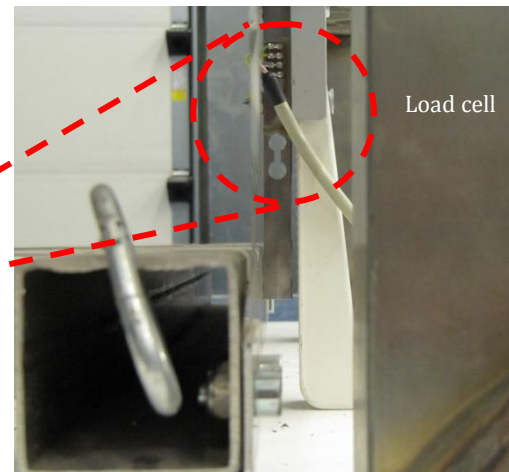


FIGURE 42: LOAD CELL

To make sure the force measurements resemble the actual forces, between each test run the load cells were calibrated with weights. A piece of rope gliding over a pulley was attached to the balance or the rotor thrust measurement tool, with weights tied to it, Figure 43 and Figure 44

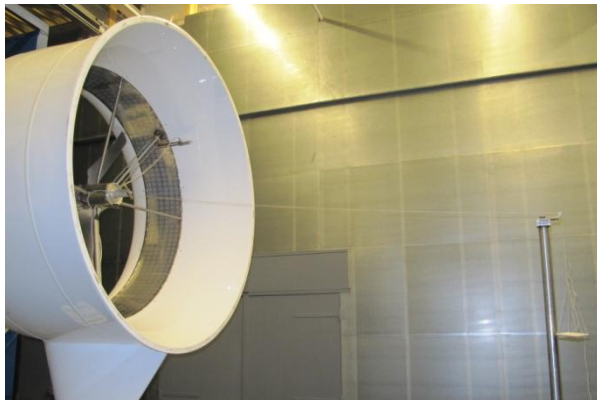


FIGURE 43: CALIBRATION

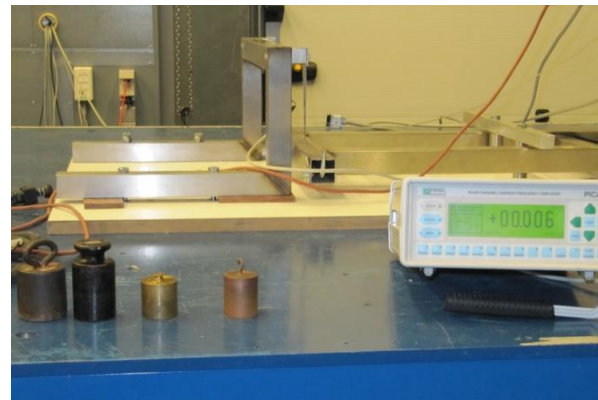


FIGURE 44: CALIBRATION EQUIPMENT

### 4.1.3 THE VELOCITY MEASUREMENTS

In order to validate the developed mathematical model which links a thrust force to a certain velocity distribution, the velocities at the rotor location are measured at multiple radial positions. For this reason a traversing mechanism was developed, which could be operated from the control room.

A five hole pitot tube was used to measure the velocities in 3D and to obtain local flow angles. In attachment B the calibration of this pitot tube is presented. Figure 45 and Figure 46 show the set-up of this pitot tube. In order to read the pressure differences the pressure hoses from the 5 hole pitot tube were attached to INITIUM pressure equipment, equipped with multiple pressure sensors, between which can be shifted within tenths of a second, when linked to a LABVIEW virtual interface.



FIGURE 45: TRAVERSING MECHANISM



FIGURE 46: 5 HOLE PITOT TUBE

## 4.2 TEST OUTLINE

In the first one and a half week the power measurements were done. In the second part of the second week, the velocity measurement were executed, since the necessary equipment was not earlier available. The second part of the power measurements were done in the third week. From now on the power measurements will be divided into session 1 and 2. In appendix D a complete overview of the tests is presented.

### 4.2.1 POWER MEASUREMENTS

The new blades have to be compared with the old blade, currently used in the DONQI URBAN WINDMILL. In order to be able to do this, for the new blades the Pn-curves<sup>15</sup> were made. They were measured for different free stream velocities and pitch angles, enabling to find the best PV-curve for each blade. A flow chart for the power measurements is given in Figure 47.

For the old blade these tests were done in the past and the optimal PV-curve was already programmed into the controller of the DONQI URBAN WINDMILL.

Each Pn-curve was produced at least twice, to check for reproducibility. Since power measurements done in the third week showed strong discrepancies with the power measurements performed in the first weeks, all power-bells were made in both test phases twice.

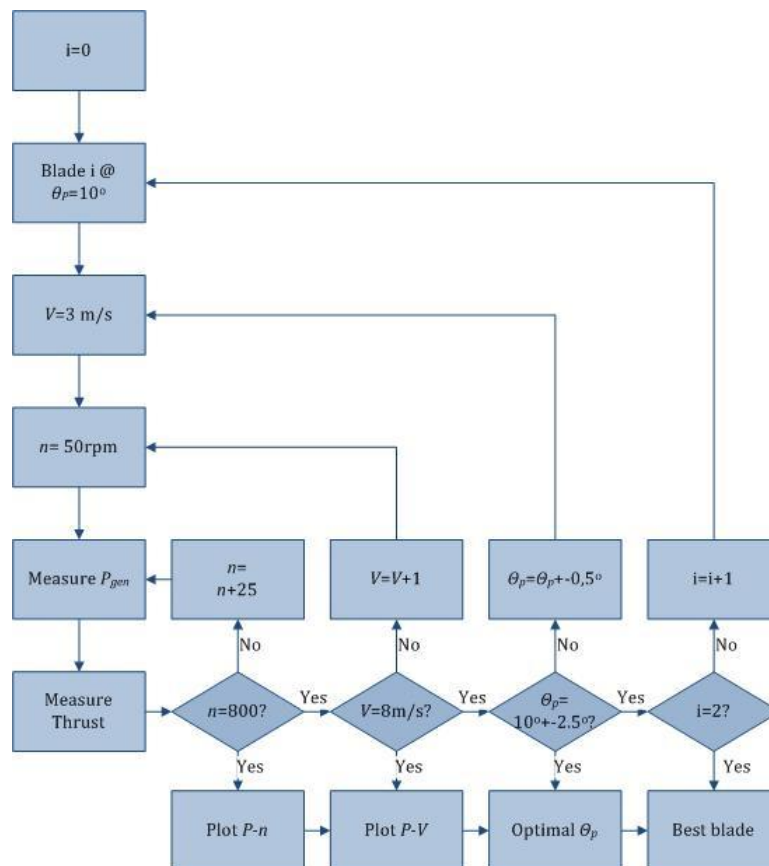


FIGURE 47: FLOWCHART POWER MEASUREMENTS

<sup>15</sup> power versus rotational speed curves at different free stream velocities

## 4.2.2 VELOCITY MEASUREMENTS

The velocity measurements have the primary purpose of validating the design process. The numerical model is based on the choice of a thrust coefficient and calculates a velocity distribution through the diffuser on various radial positions at the rotor location. This can be checked by varying the thrust on the rotor, so the loading on the blades at a certain free stream velocity and measure the velocities at the rotor position at different radial positions. The pitch angles were varied as well during these tests. The velocity measurements were done with the custom-made traversing 5-hole pitot tube in combination with the custom-made axial force measurement equipment. The velocity measurements were done with the three different blades.

A flow chart for these tests is given in Figure 48.

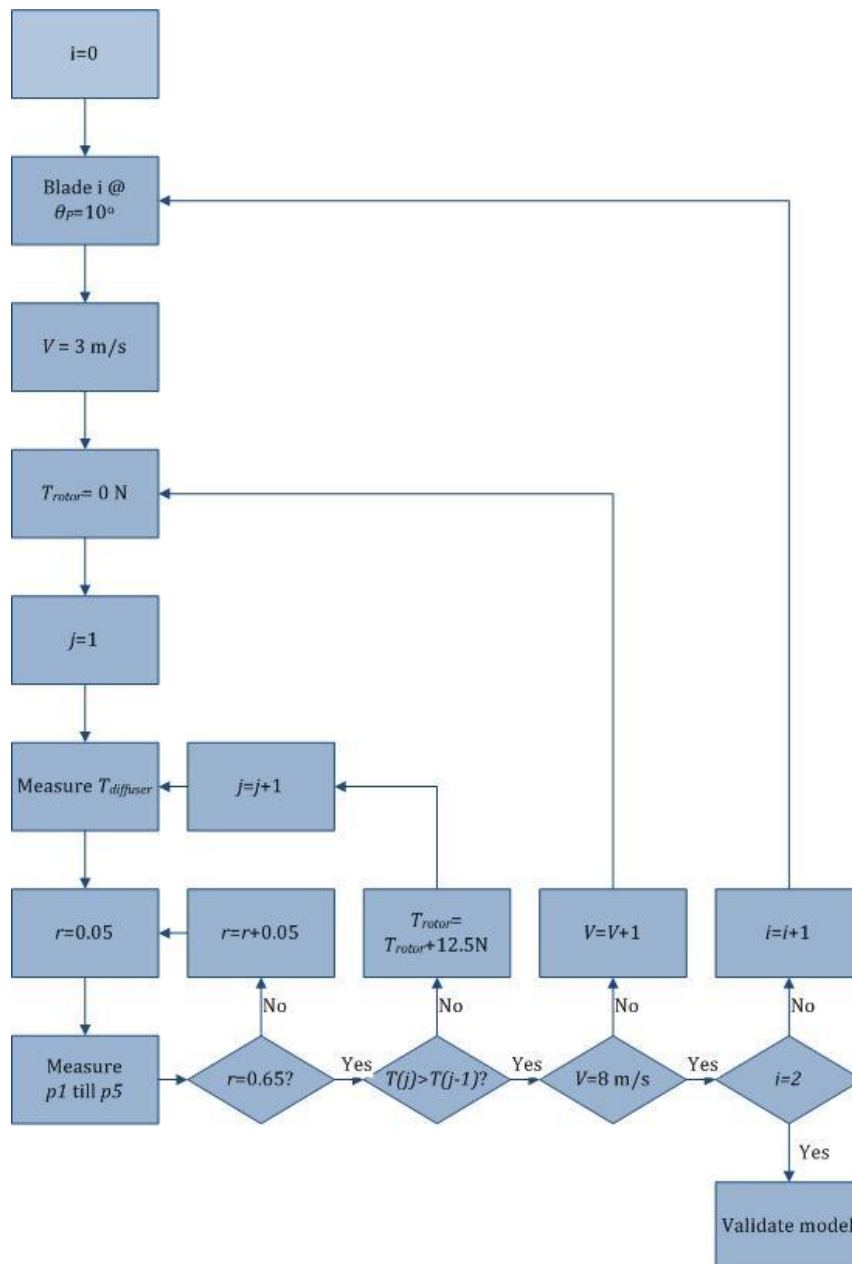


FIGURE 48: FLOWCHART VALIDATION MEASUREMENTS

### 4.3 BLOCKAGE CORRECTIONS

Since the DONQI URBAN WINDMILL is quite large in comparison to the jet's stream tube, a blockage correction has to be included in this research.

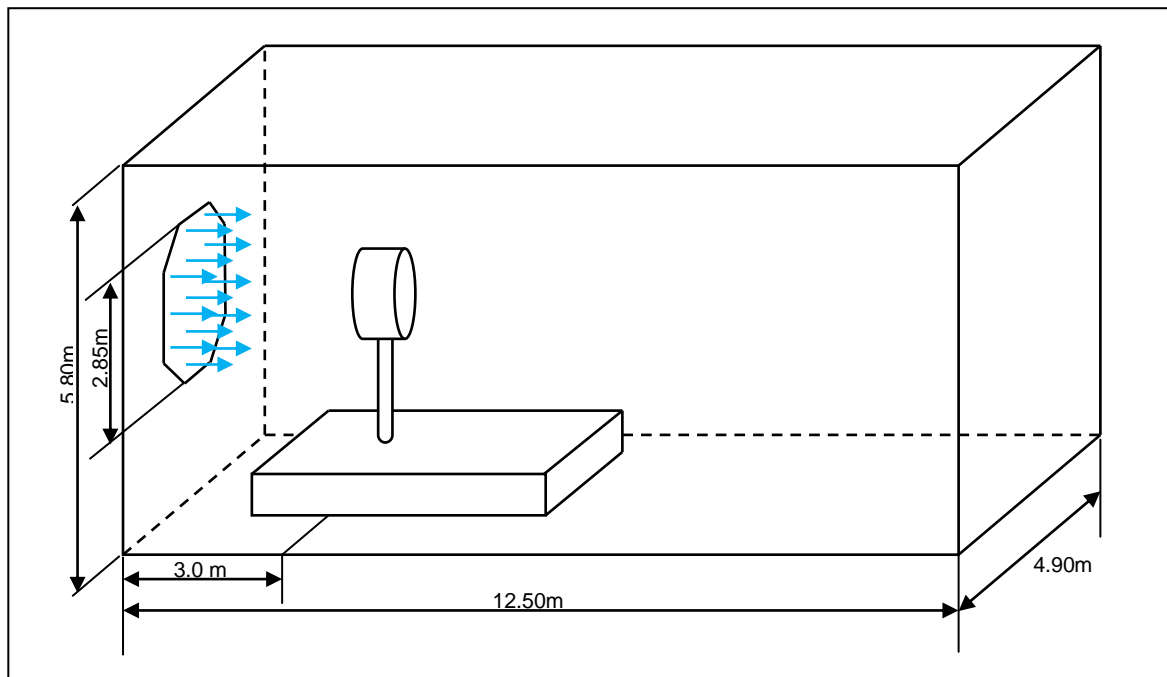


FIGURE 49: OJF TEST SET UP

In an open jet mainly the free jet shear layer has to be included for blockage correction [33] [34] [35]. The measured drag appears to be lower than the actual drag and upstream velocity effects need to be taken into account since they distort the flow and influence the measurement points. There apply different rules for open and closed jet tunnel sections. AGARD 336 [33] has a separate chapter devoted to open jet tunnels, as the OJF. The major effect is solid blockage, this results into a velocity reduction at the measurement point. Four types of blockage should be taken into account:

- Nozzle blockage
- Solid blockage and jet expansion
- Empty tunnel pressure gradients (horizontal buoyancy)
- Collector blockage

No pressure measurements were done in the test section, this means the influences of the horizontal buoyancy cannot be taken into account in this correction. Two other types of blockage that are not looked into are wake blockage and blockage due to propeller induction alternation. Wake blockage is assumed to be negligible for open test sections, as the OJF [34]. The propeller induction alternation as derived by Glauert in [34] includes more types of blockage. To get a better insight in the contribution of the several types of blockage, the nozzle, solid and collector blockage are calculated separately. The total blockage is given with the equation derived by the Mecker and Wiedemann method [33]:

$$\frac{q_c}{q_u} = (1 + \varepsilon_s + \varepsilon_n + \varepsilon_c)^2 \quad \text{EQUATION 4.1}$$

### 4.3.1 NOZZLE BLOCKAGE

The difference in the dynamic pressure is a function of the axial position of the model and the exerted drag on the nozzle, the outflow of the tunnel into the test section. The surface stresses are bigger than for a free air condition [34] since expansion is limited. The measured velocity should be increased with a factor  $\eta$ , to equal the free stream asymptote. There are two ways of calculating the correction factor, based on two different ways of how the velocity measurement was done: the plenum method or the nozzle method. For the OJF, the nozzle method applies. The upstream effects influencing the conditions in the nozzle are modeled by a point source. This point source is sized to provide an area of a body of revolution at downstream infinity that is equal to the model's frontal area. The position is determined by locating the stagnation point of the source at the leading edge of the model.

The strength of the source is determined by:

$$Q_s = U_u A_{turbine} \quad \text{EQUATION 4.2}$$

The axial location of the point source can be calculated with:

$$x_s = -x_m + \frac{L_m}{2} - \sqrt{\frac{A_{turbine}}{2\pi}} \quad \text{EQUATION 4.3}$$

In which respectively the axial position of the turbine, the length and the frontal area of the turbine are taken into account. The following formula is presented to get to the nozzle blockage correction factor with the ring vortex positioned at the nozzle exit plane:

$$\varepsilon_{qn} = \frac{\frac{A_{turbine}}{2A_{nozzle}} \left( 1 + \frac{x_s}{\sqrt{x_s^2 + R_n^2}} \right)}{1 - \frac{A_{turbine}}{2A_{nozzle}} \left( 1 + \frac{x_s}{\sqrt{x_s^2 + R_n^2}} \right)} \quad \text{EQUATION 4.4}$$

In which  $R_n$  is the hydraulic radius of the jet nozzle. Projecting the blockage to the model location gives:

$$\varepsilon_n = \varepsilon_{qn} \left( \frac{R_n^3}{(x_m^2 + R_n^2)^{3/2}} \right) \quad \text{EQUATION 4.5}$$

### 4.3.2 SOLID BLOCKAGE

A velocity reduction is induced by the expansion of the free jet flow, and the flow angle is increased by the model proximity, leading to a further increasing jet expansion. This is a function of the area ratio of the turbine and the nozzle, giving:

$$\varepsilon_s = \tau \left( \frac{V_{turbine}}{L_{turbine}} \right)^{1/2} \left( \frac{A_{turbine}}{A_{nozzle,eff}^{3/2}} \right) \quad \text{EQUATION 4.6}$$

With the effective nozzle area as:

$$A_{nozzle,eff} = \frac{A_{nozzle}}{1 + \varepsilon_{qn}} \quad \text{EQUATION 4.7}$$

In Equation 4.6,  $\tau$  stands for the solid blockage constant and is calculated with:

$$\tau = 0.41 \left( \frac{B}{H} + \frac{H}{B} \right) \quad \text{EQUATION 4.8}$$

### 4.3.3 COLLECTOR BLOCKAGE

The wake emanating from the turbine entering the collector of the OJF is going from an open jet boundary condition into a closed wall boundary condition. This change in constraints on the wake, induce a velocity increment at the turbine. The effect however should be small, since the distance between the end of the turbine and the collector is relatively large. The collector blockage can be calculated with:

$$\varepsilon_c = \varepsilon_{wc} \frac{R_c^3}{((L_{ts} - x_m)^2 + R_c^2)^{3/2}} \quad \text{EQUATION 4.9}$$

With

$$\varepsilon_{wc} = \frac{C_{Du,0}}{4} \frac{A_{turbine}}{A_{collector}} + 0.41 \frac{A_{front,turbine}}{A_{collector}} \quad \text{EQUATION 4.10}$$

For the area of the collector, the area of the cooler tubes is deducted from the total area.

### 4.3.4 TOTAL BLOCKAGE

The total blockage can now be calculated and is equal to Equation 4.1:

$$\frac{q_c}{q_u} = (1 + 0.0095 - 0.0352 + 0.0009)^2 = 0.95 \quad \text{EQUATION 4.11}$$

This means that the incoming velocities on the turbine have to be corrected with a factor equal to the square root of 0.95. With this correction, the performance of the blades can be compared to the calculated results of the blades.

A remark to the total blockage is that the corrections are calculated based on the frontal area of the turbine. This is however not a solid circular surface, but permeable. A way to correct for this fact is to scale the calculated blockage with the ratio of the actual thrust coefficient and the thrust coefficient of a circular solid surface, 1.2. For the extra correction, no scientific basis is available, so this has not been incorporated in the data analysis of the current research.

#### 4.4 EXPERIMENT ACCURACY CONSIDERATIONS

The experiments are executed with taking the accuracy considerations into account. For each of the single experiments, temperature and atmospheric pressure were stored, the thrust measuring tools were calibrated and the velocity measurement equipment was re-zero-ed. However, some notes have to be made.

First, the new blades were heavier than the old blade, and it was not possible to fully balance the rotor. This caused some vibrations in the turbine, which was noticeable at higher wind speeds. Therefore, there were hardly any measurements possible for the thrust on the total turbine with the new blades installed. Instead of a smooth axial displacement, the hammock was swinging against the load cell, not providing any usual data. Fortunately, these measurements were possible with the old blade installed. Because of these heavier blades, it was not possible to test up to high wind speeds. In consultation with the people responsible for the OJF it was decided not to exceed 8m/s in the experiments.

Second, the traversing mechanism for the five hole pitot tube was fixed on a thread with two rods, to prevail it from vibrating, however it did vibrate slightly. This was due to an off-centered hole at the end of the thread, attached to the motor driving the rotation of the thread.

As will be shown in the next chapter there is a discrepancy between the measurement in the two test sessions. In both test sessions, the tests were repeated at least twice, to show reproducibility, but nevertheless, the discrepancy between the two test session could not be explained. The total electrical connection was checked and found to be connected correctly. The generator was put on a test bench to check whether there was some internal damage.

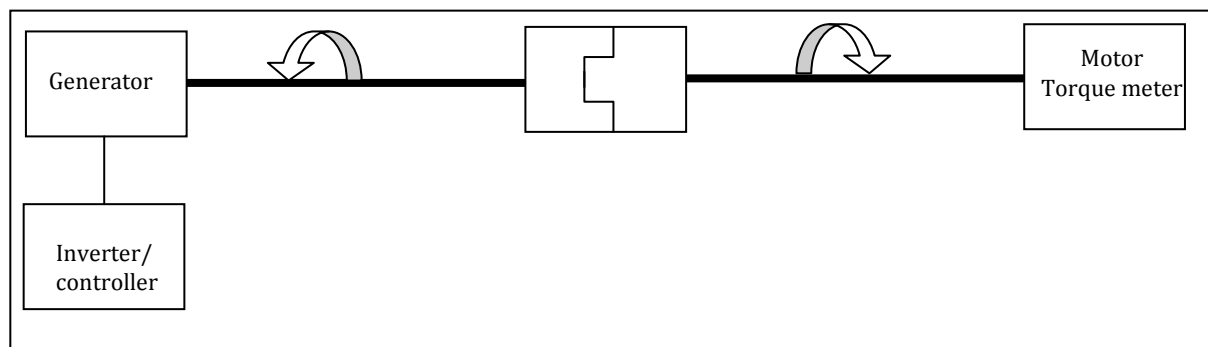


FIGURE 50: GENERATOR CHECK

In this test, a motor was driving the generator at a certain rotational speed. With the controller, the generator was excited with a certain voltage, resulting in power output. The excitation requires a torque to keep the generator rotating at the same rotational speed. The required torque was measured. Together with the rotational speed, this gave the mechanical power necessary to provide a certain electrical power.

The test showed that the generator used in the tests performed comparable to other generators used by DONQI. These test results can be found in appendix E. The test results were helpful to convert the measured electrical power in all the power tests to mechanical power and compare them to the power estimated by the numerical model.

During the tests the turbine was removed in the second test-week and installed again, it is possible that the turbine was lowered a bit further into the support, therefore having a different vertical position in both test session.

One other thing worth mentioning is the blockage correction. The horizontal buoyancy was not taken into account. For future experiments in the OJF it is therefore advisable to perform pressure measurements in the test section, and create a pressure gradient, to be able to correct for the horizontal buoyancy.

A last remark is that the airfoil used for the old blade in the DONQI URBAN WINDMILL is a NACA 2207 profile with a nose drop of 6%. The tested new blades have a cross section compared to a regular NACA 2207 profile. This was an error during the drawing of the blades. Therefore, the results of the new blades with the correct cross sectional area could turn out to be higher than the results presented in the next chapter.



## 5 EXPERIMENTAL RESULTS

This chapter presents the results of the experiments performed in the OJF. The experiments are divided into the performance of the different blades and the model validation, for which force and velocity measurements are done. Three different blades were tested, the old blade, which is used in the DONQI URBAN WINDMILL and the two new designed blades, the optimal blade and the linearized blade, Figure 51 to Figure 53.



FIGURE 51: OLD BLADE



FIGURE 52: OPTIMAL BLADE



FIGURE 53: LINEARIZED BLADE

### 5.1 PERFORMANCE OF THE BLADES

For the three blade types power rotational speed curves,  $P_n$ -curves, were measured as described in 4.2.1. For each blade, at least two full  $P_n$ -curves were made for each combination of free stream velocity and pitch angle, to ensure reproducibility of measurement results. This paragraph will first show how the  $P_n$ -curves were made and look like. From there on the PV-curves are discussed with blockage corrections and the transformation from generator power to mechanical power, to be able to compare the power measurements with the predictions of the numerical model. There is a distinction made in the results of different experiments, by three different blades, two different test sessions, different free stream velocities, different pitch angles and two different test runs for each configuration.

#### 5.1.1 POWER CURVES OLD BLADE

The optimal power curve for the original blade was already programmed in the controller of the DONQI URBAN WINDMILL, so it was rather straightforward to obtain the PV curve for the old blade. By varying the free stream velocity and recording the power output of the turbine the PV-curve was measured. The results are presented in Figure 54. The maximum performance at 8 m/s is about 20W higher in the first test session compared to the second test session, but all over the PV curves show a strong resemblance.

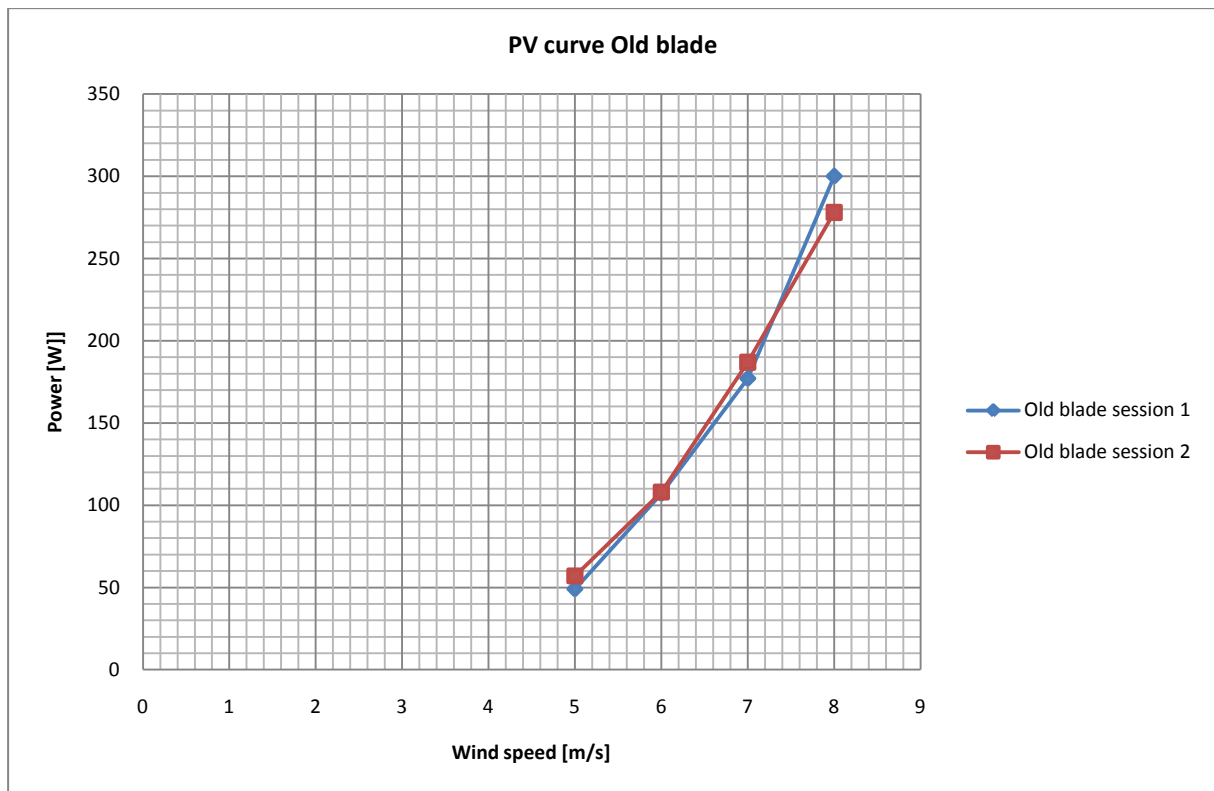


FIGURE 54: PV CURVE OLD BLADE

### 5.1.2 POWER CURVES OPTIMAL BLADE

The Pn-curves, were measured for different free stream velocities with the optimal blade in different pitch angles. The Pn-curves for two runs in the first test session in its optimal pitch angle,  $10^{\circ}$ , are presented in Figure 55 and Figure 56 respectively. Comparing these two plots show that their shapes are quite similar. This is especially noticeable in the higher power region, where both curves show a wave-like shape. The wave shape is probably caused by a difference in the optimal working points of the generator and the inverter. The maximum power in the low velocity regions is higher in the second run and is also reached at an increased rotational speed. The difference however is marginal, which shows a good repetitivity in the measurements.

The Pn-curves measured in the second test session for the optimal blade in its optimal pitch angle,  $10.5^{\circ}$ , are shown in Figure 57 and Figure 58. Less measurements were taken, due to limited time. This explains the shorter curves. Striking is that the maximum power points in second test session are much lower and occur at lower rotational speeds. Comparing the two graphs of the Pn-curves in the second test session show a strong resemblance, only the maximum power at 8m/s for the first run is higher, showing repetitivity as well. When looking at Figure 56 and Figure 57, it seems that during the experiments in the second test session, a mistake was made by consistently measuring a local maximum power output, at a lower rotational speed and not the actual global maximum power at an increased rotational speed. Paragraph 5.1.7 is devoted to explain the discrepancy between the two test sessions.

The PV-curves for the optimal blade are obtained by finding the maximum power output for each value of the free stream velocity, this is shown for the first and the second test session in Figure 59 and Figure 60 respectively. In Figure 61, the PV-curves for the optimal blade are plotted in one PV-graph.

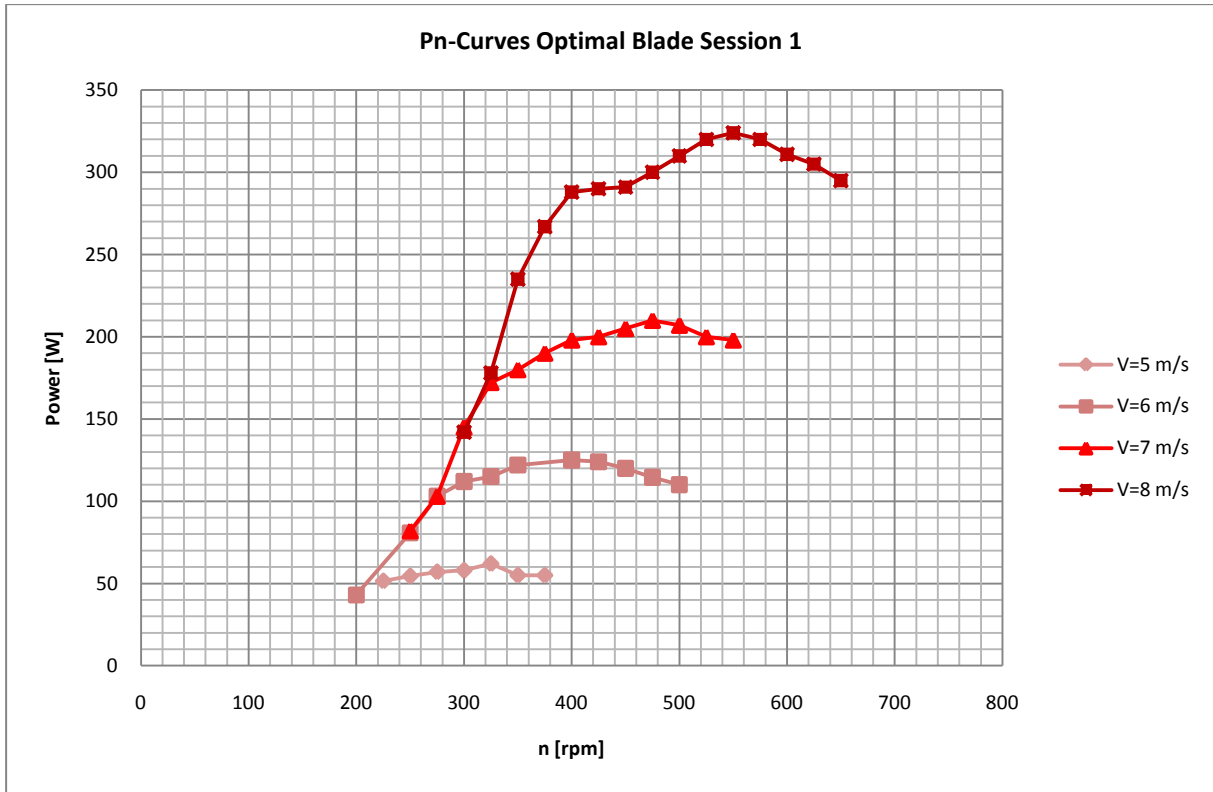


FIGURE 55: PN CURVES OPTIMAL BLADE SESSION 1 RUN1

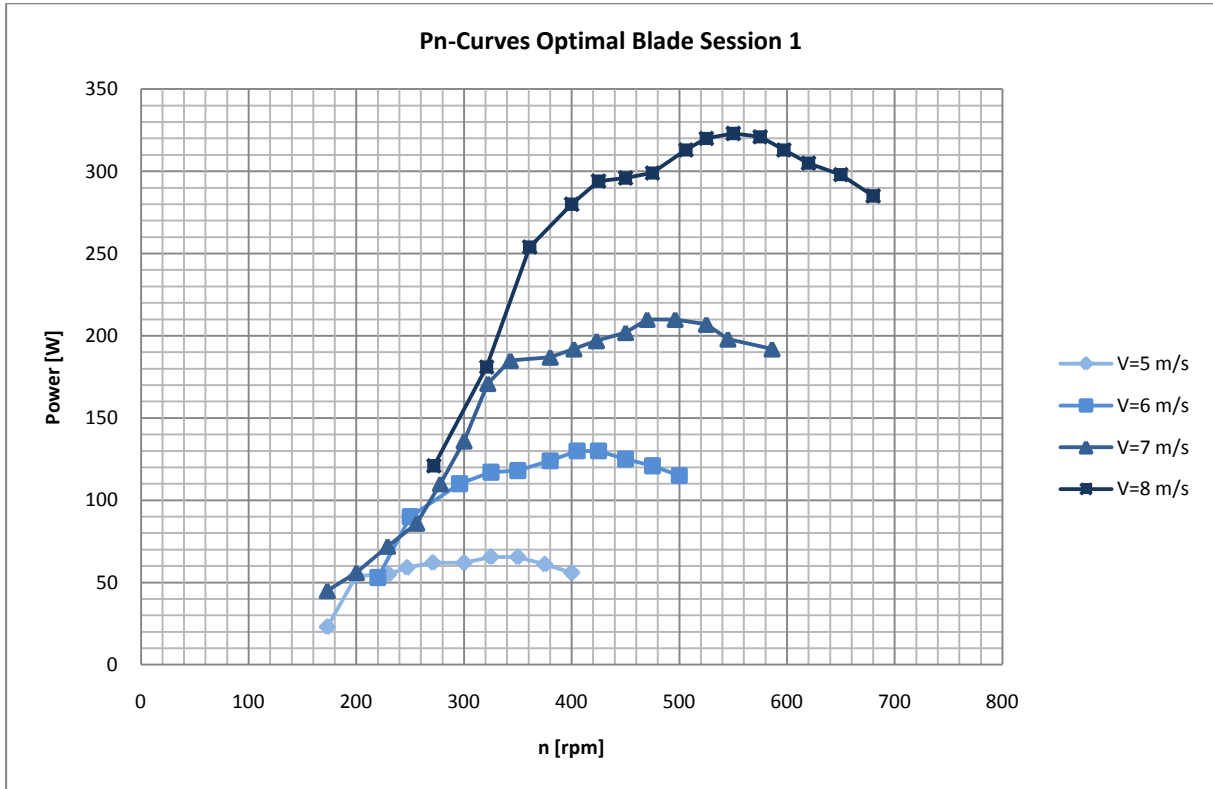


FIGURE 56: PN CURVES OPTIMAL BLADE SESSION1 RUN2

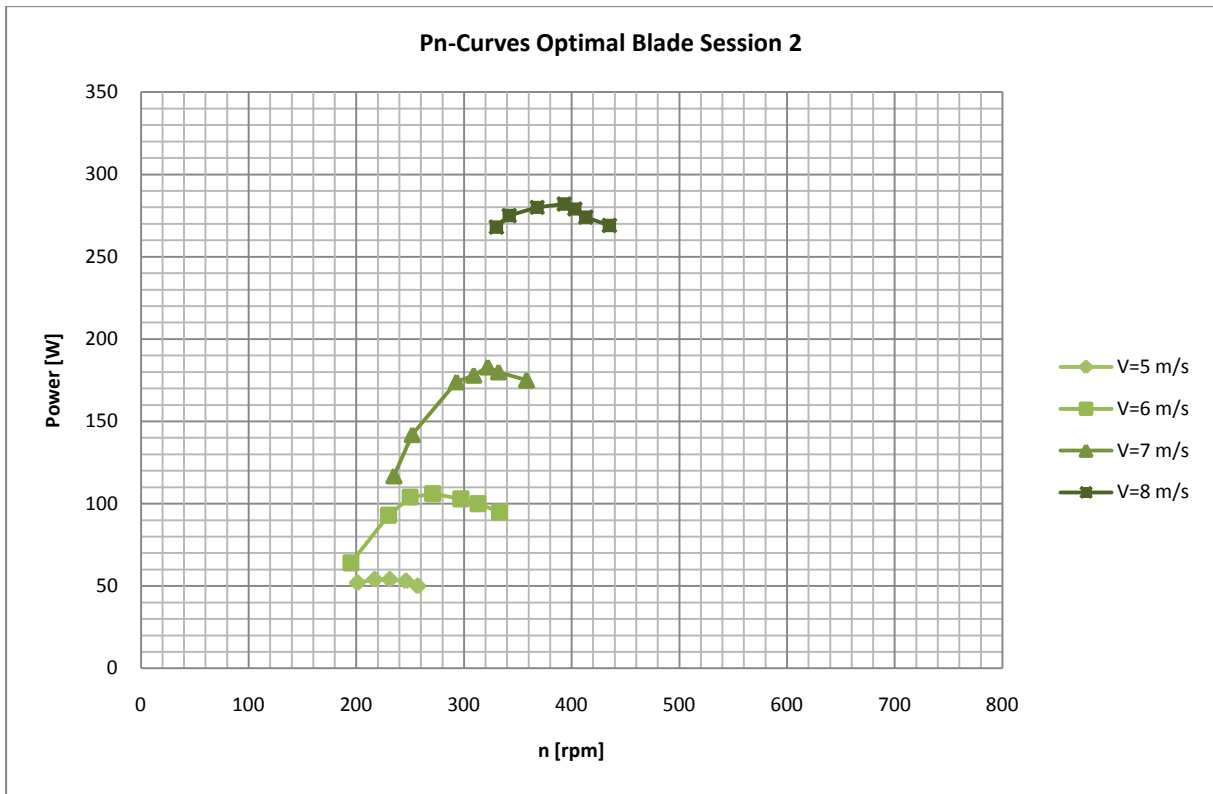


FIGURE 57: PN CURVES OPTIMAL BLADE SESSION2 RUN1

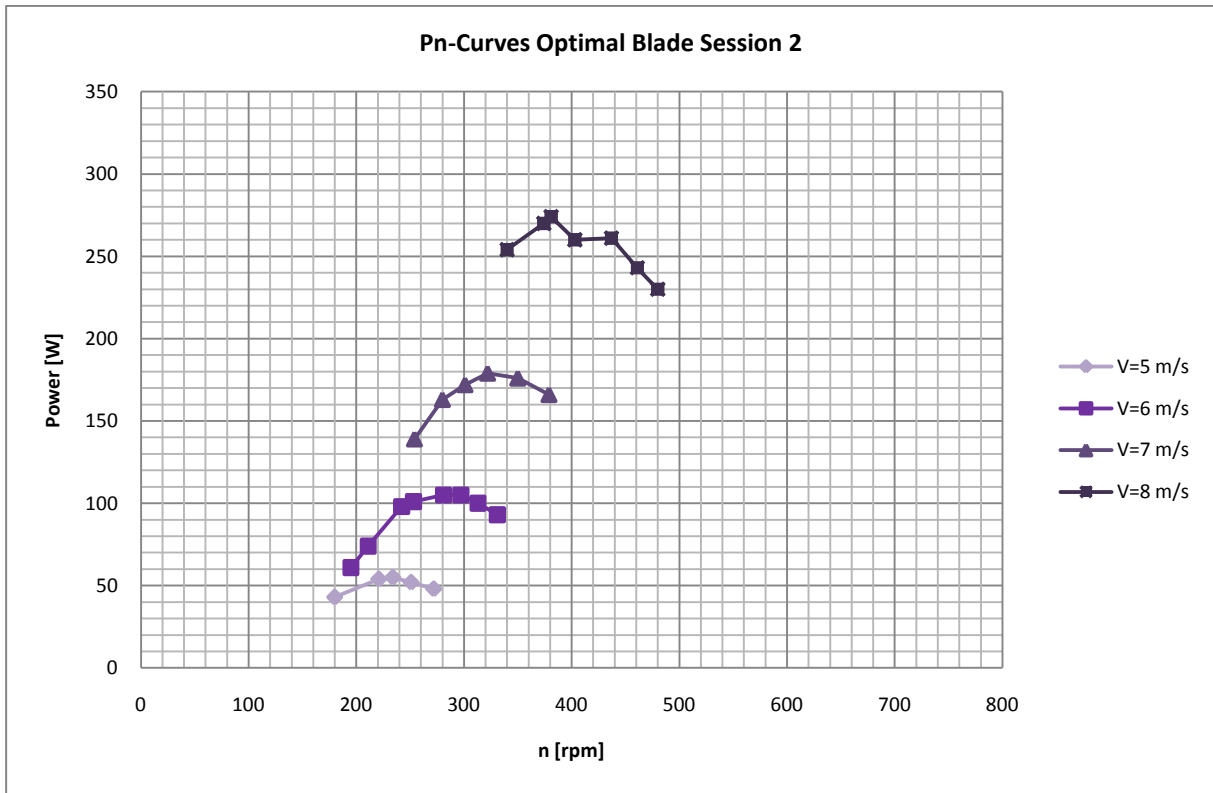


FIGURE 58: PN-CURVES OPTIMAL BLADE SESSION2 RUN2

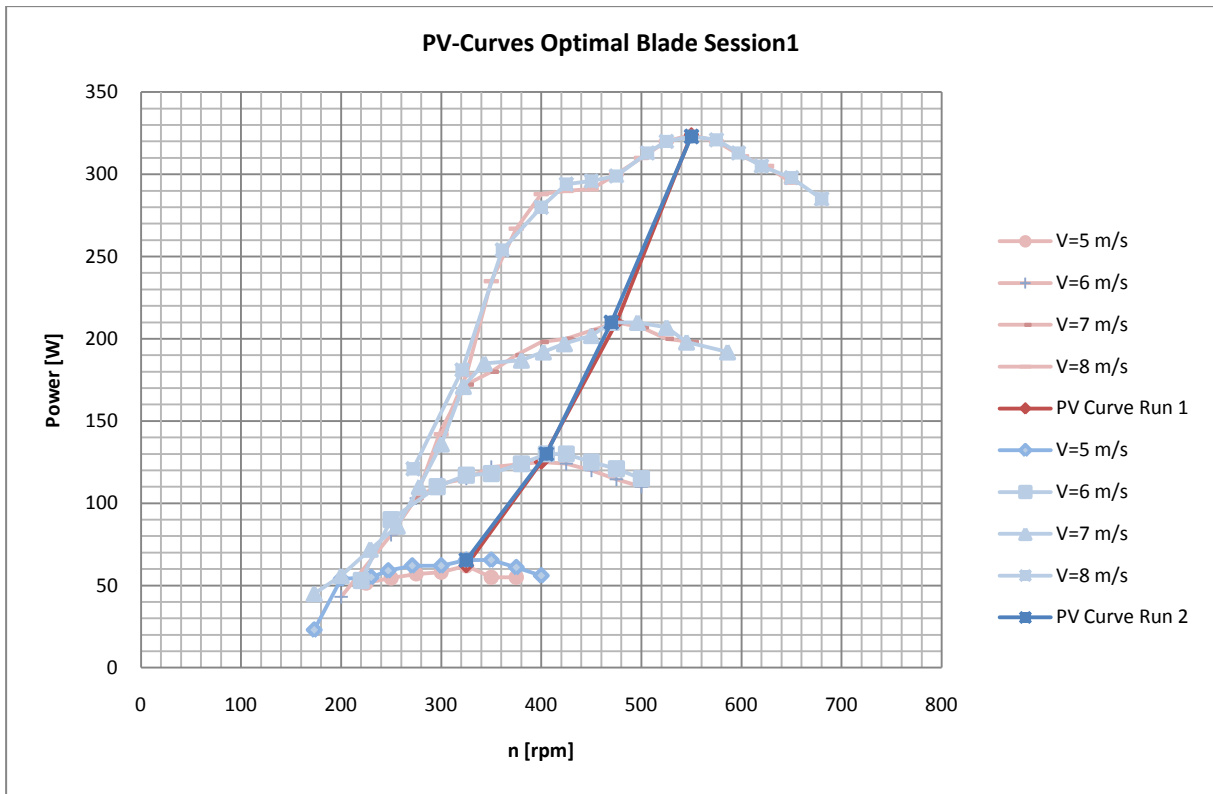


FIGURE 59: PV CURVES OPTIMAL BLADE SESSION 1

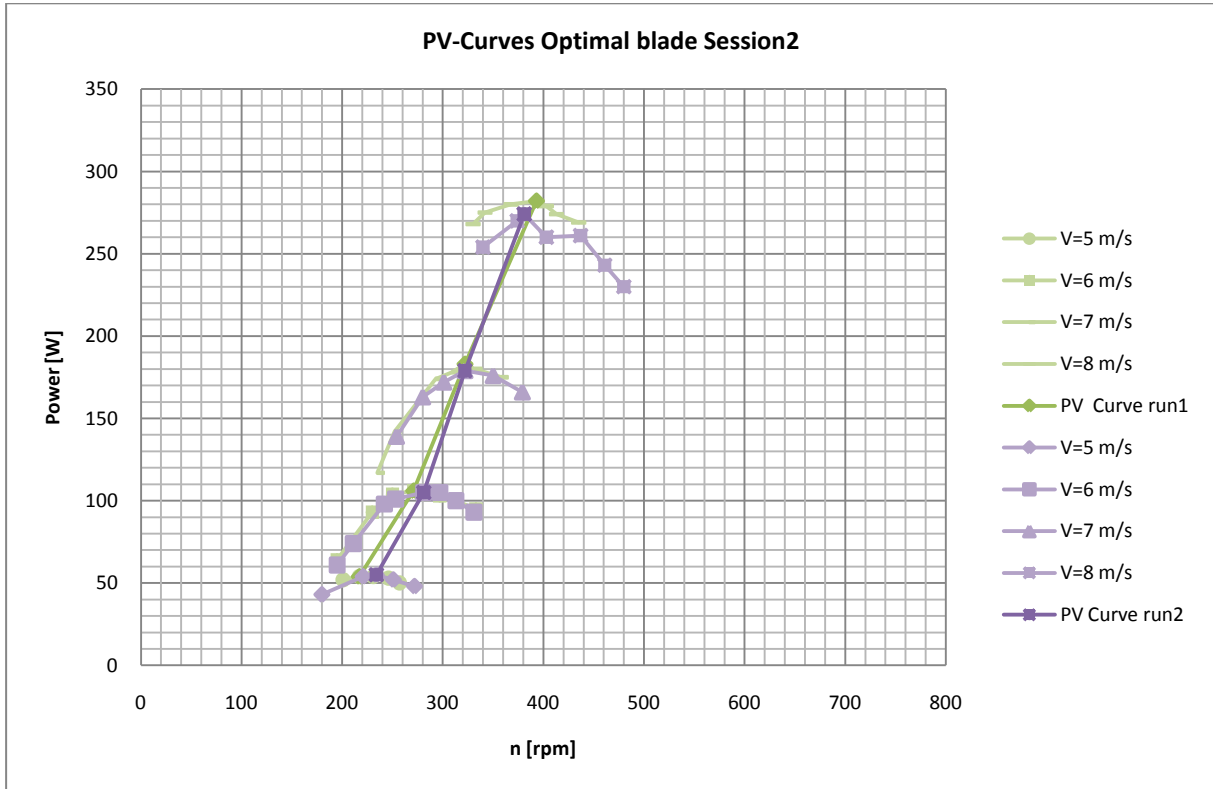


FIGURE 60: PV CURVES OPTIMAL BLADE SESSION 2

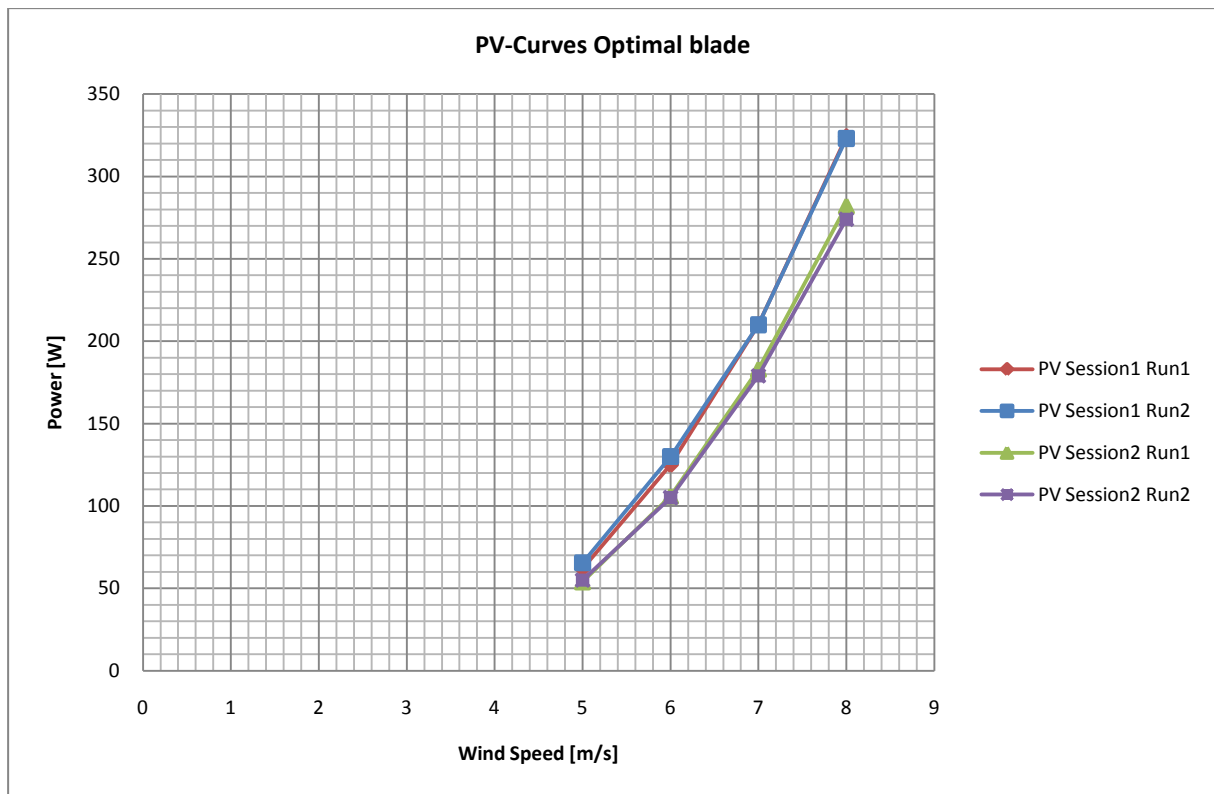


FIGURE 61: PV-CURVES OPTIMAL BLADE

The PV-curves in Figure 61 confirm the strong discrepancy, which will be discussed in paragraph 5.1.7. The best test run, run 2 in the first test session, is used to compare the optimal blade with the old and linear blade in paragraph 5.1.4. For this comparison the measurements of the second test session are not taken into account, because of the strong discrepancy.

### 5.1.3 POWER CURVES LINEAR BLADE

The Pn-curves measured with the linear blade in its optimal pitch angle,  $10^\circ$ , are presented in Appendix F, Figure 98 to Figure 101. The Pn-curves combined with the PV-curves for the first and second test session are presented in Figure 62 and Figure 63 respectively. Comparing the two Pn-curves of the first test session, also shown in Figure 62, show that in the second run the maximum power is reached at a lower rotational speed and that the maximum power is reduced. This is made clear in Figure 62 where the PV-curves are obtained by finding the maximum power output for each value of the free stream velocity. These curves substantiates the presumption that the discrepancy is caused by wrongly executed measurements as stated in the previous paragraph. In Figure 64 the PV-curves are plotted in one PV-graph, showing that the PV-curves are quite similar. The maximum measured performance in the first test session is a bit reduced in the second run. The noticed discrepancy between the measurement with the optimal blade are visible as well for the measurements with the linear blade. The best test run, first session, run1, is used to compare the linear blade with the other two blades.

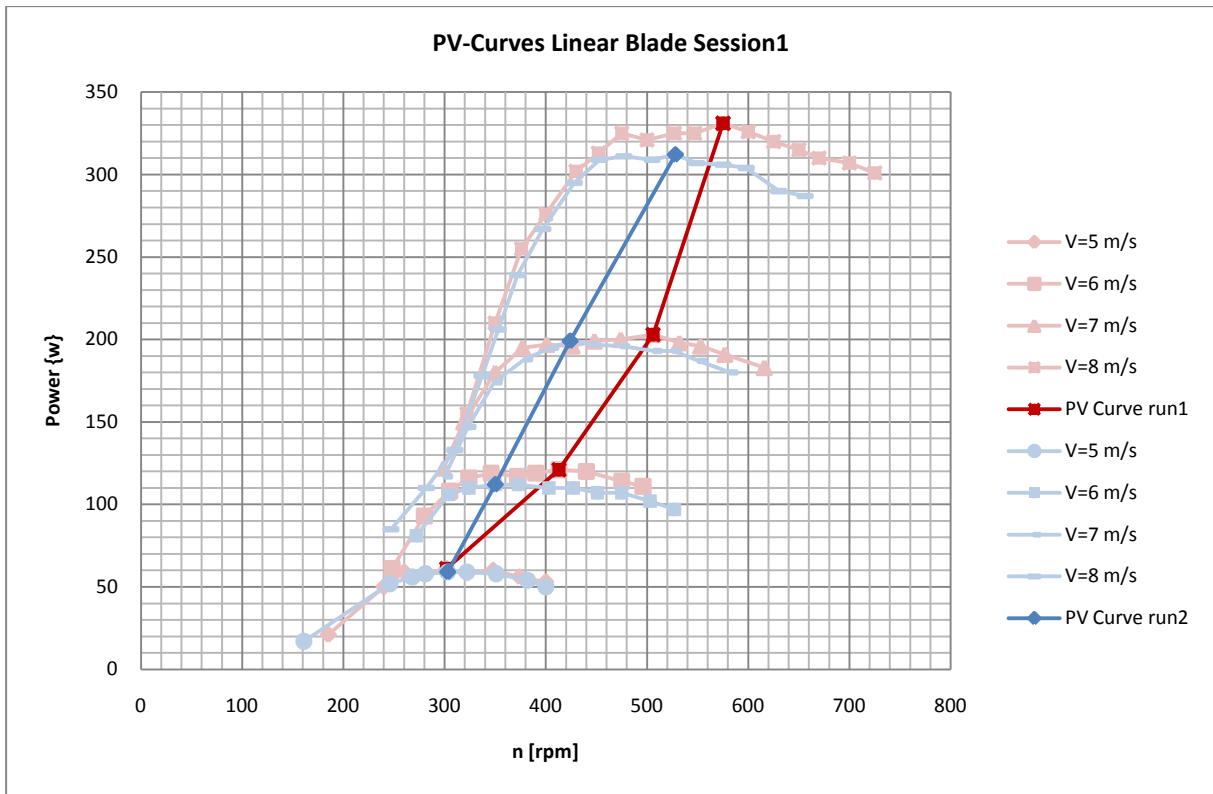


FIGURE 62: PV CURVES LINEAR BLADE SESSION1

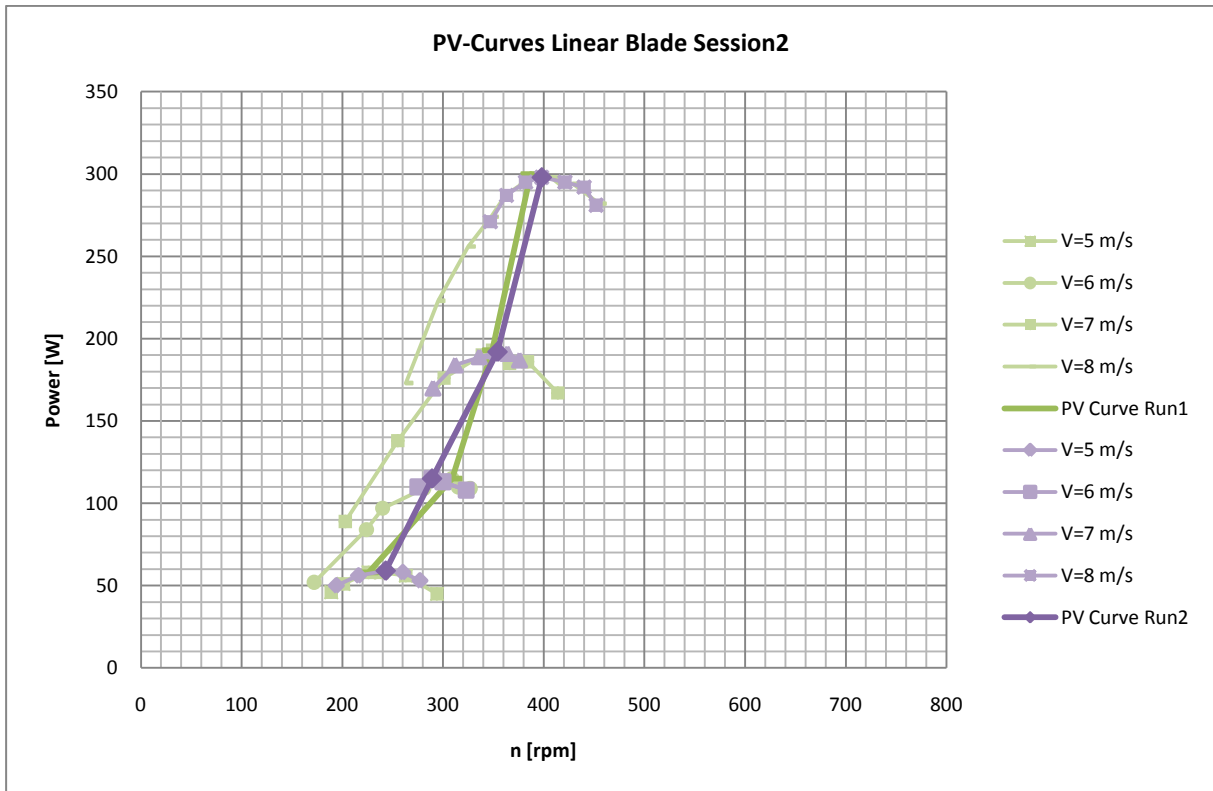


FIGURE 63: PV-CURVES LINEAR BLADE SESSION2

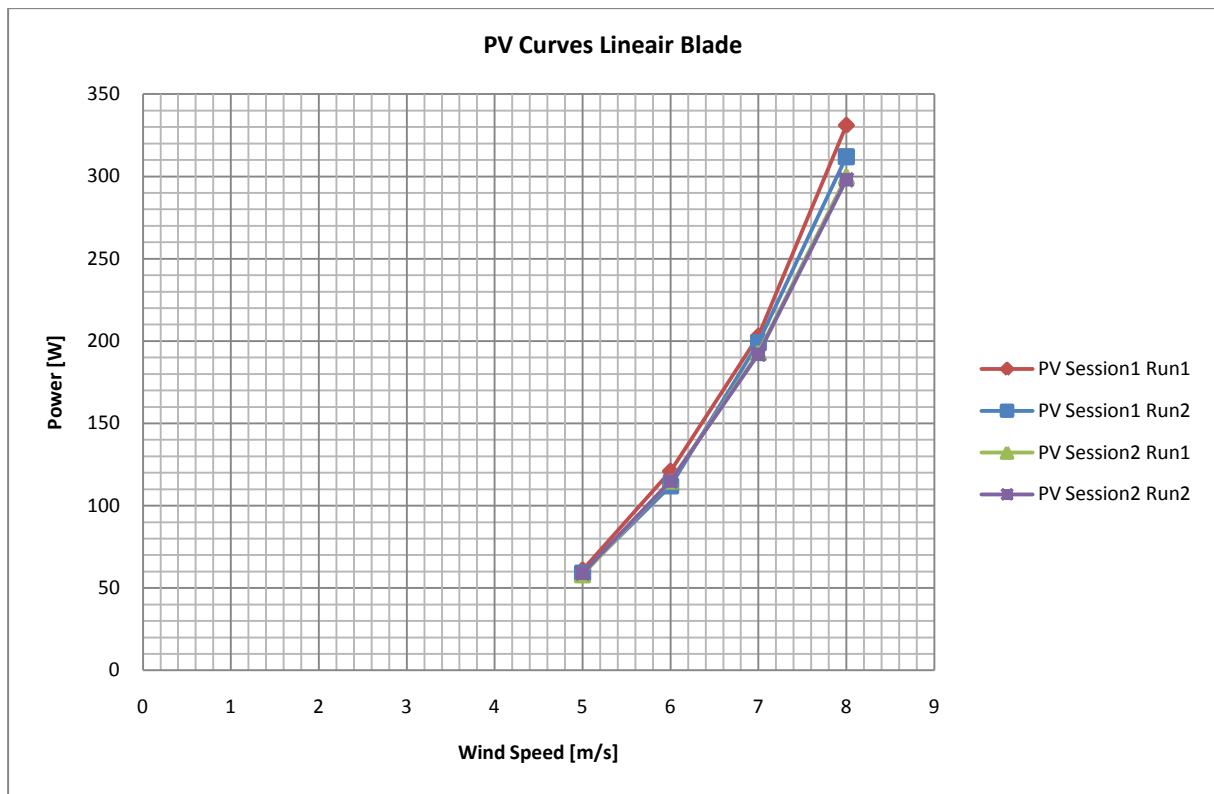


FIGURE 64: PV CURVE LINEAR BLADE

The four PV-curves for the linear blade are presented in Figure 64. They show repetitivity in the measurements, when distinguishing between the two test sessions.

#### 5.1.4 PV-CURVES OF THE THREE BLADES

Because of the strong discrepancy between the two test sessions, only the measurements of the first test session are compared with each other in this paragraph. The measured PV-curves are subject to a blockage in the OJF test section, as explained in paragraph 4.3. The calculations done in this paragraph, show that the DONQI URBAN WINDMILL in outdoor operation will produce corresponding powers at lower velocities as measured in the OJF. Before continuing with comparisons and calculations this so-called blockage correction needs to be taken into account. The correction results in a slight shift of the optimal PV-curves to the left. The PV-curves resulting from this correction are presented in Figure 65 for all three blades.

The measured power in the OJF is the so-called generator power. Since the numerical model calculates the aerodynamic power of the different blades, the measured generator power has to be converted into the aerodynamic power, which is equal to the mechanical power. The difference between the generator power and the mechanical power is the efficiency of the generator. The conversion is done by using the test results of the generator test described in paragraph 4.4 and presented in Appendix E. For a combination of rotational speed and generator power, the efficiency of the generator is known, enabling to calculate the mechanical power delivered by the rotor blades. The final PV-curves for the three blades are presented in Figure 66.

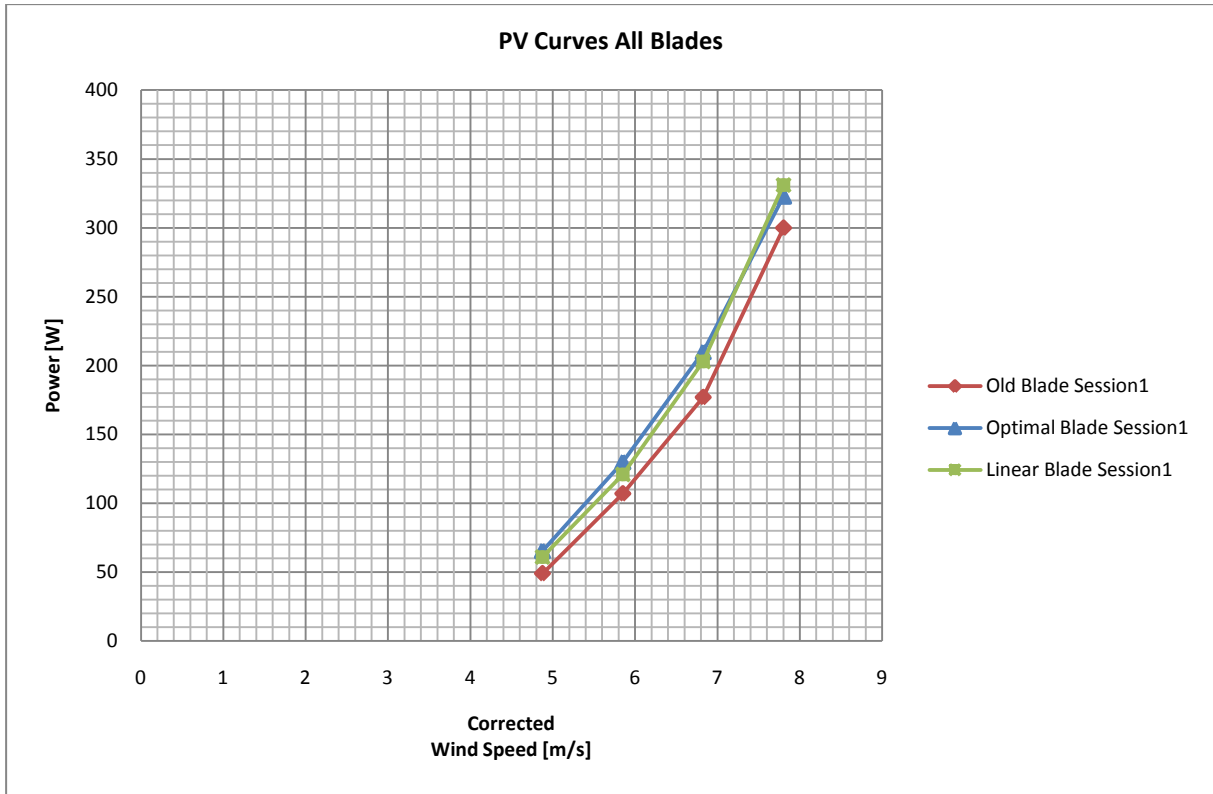


FIGURE 65: OPTIMAL PV-CURVES THREE BLADES, CORRECTED FOR TUNNEL BLOCKAGE

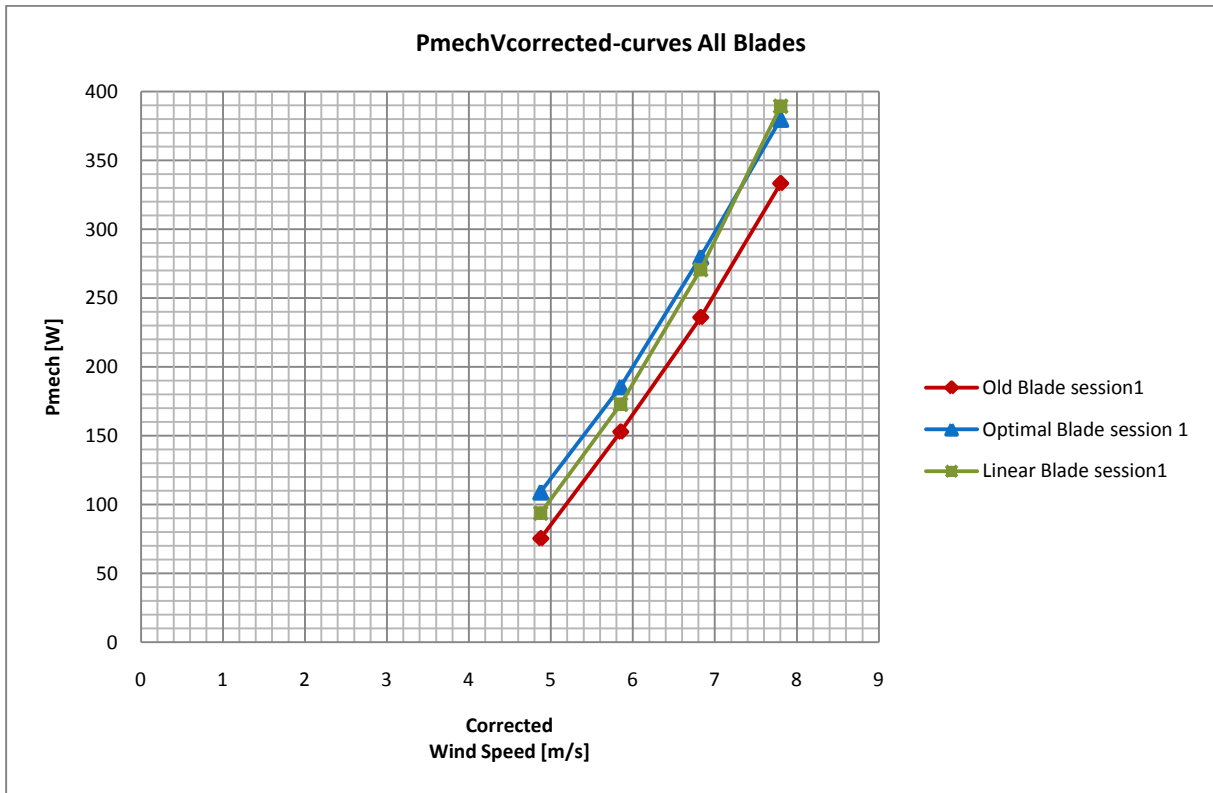


FIGURE 66: OPTIMAL PV-CURVES, CORRECTED FOR BLOCKAGE AND GENERATOR EFFICIENCY

The optimal and the linear blade outperform the old blade of the DONQI URBAN WINDMILL, as shown in Figure 66, by 15%. Noticeable is as well that at higher wind speeds the linearized blade is performing better than the optimal blade. This is mainly due to the reduced chord at the root section of the linearized blade with respect to the optimal blade. A bigger chord at the root assists the optimal blade to have a lower cut-in speed, but 'slows' it down at higher wind speeds, caused by increased drag. The cut-in speed of the optimal blade is about 3.2 m/s and the cut-in speed of the linear blade is 3.7 m/s.

The power coefficients can be used to compare the measurement results with the results of the numerical model. The power coefficients are obtained by making the power non-dimensional with the rotor swept area and are presented in Figure 67 for the three blades. The  $C_p$  of the DONQI URBAN WINDMILL is increased with 15% by use of the optimal or linear blade. The  $C_p$ -curve shows as well that the optimal blade is performing better than the linear blade at lower wind speeds. Unfortunately it was not able to perform measurements at higher wind speeds, to show that than the linear blade will outperform the optimal blade.

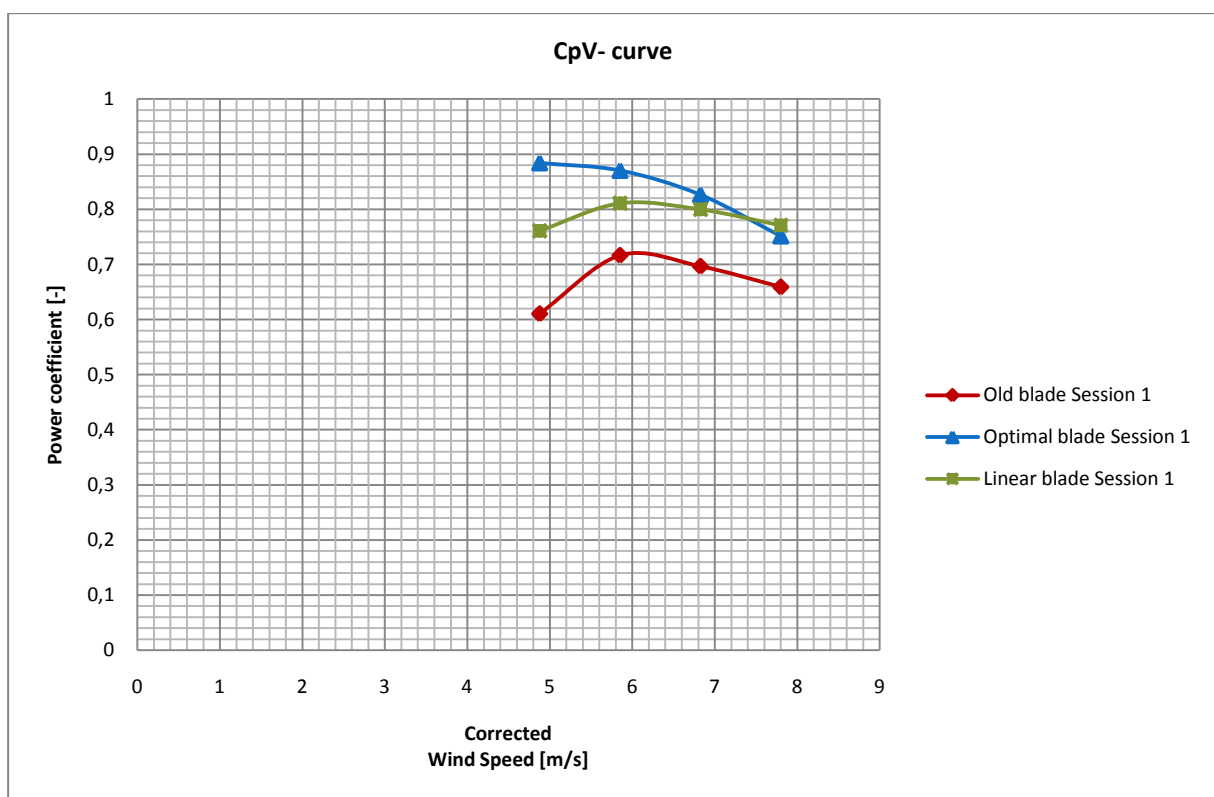


FIGURE 67: CP CURVES DIFFERENT BLADES

The power coefficients predicted in paragraph 3.6.3 are lower than the coefficients shown in Figure 67. This can be explained since the model calculates the power coefficient under standard atmospheric conditions and the measured power coefficients use the actual conditions. Another explanation is that, the measured power in the experiments is higher than the predicted power by the numerical model, as will be shown in paragraph 5.1.6.

### 5.1.5 ANNUAL ESTIMATED PRODUCTION

The Annual Estimated Production, AEP, is a way of checking what blade type will deliver more energy in one year. It is calculated by combining the measured generator power-wind speed curves and wind data from a certain installation site. The wind data was obtained for installation on the roof-top of a building in Rotterdam, The Netherlands, for which DONQI has done some extensive measurements [36]. The Weibull plot for this location is given in Figure 68.

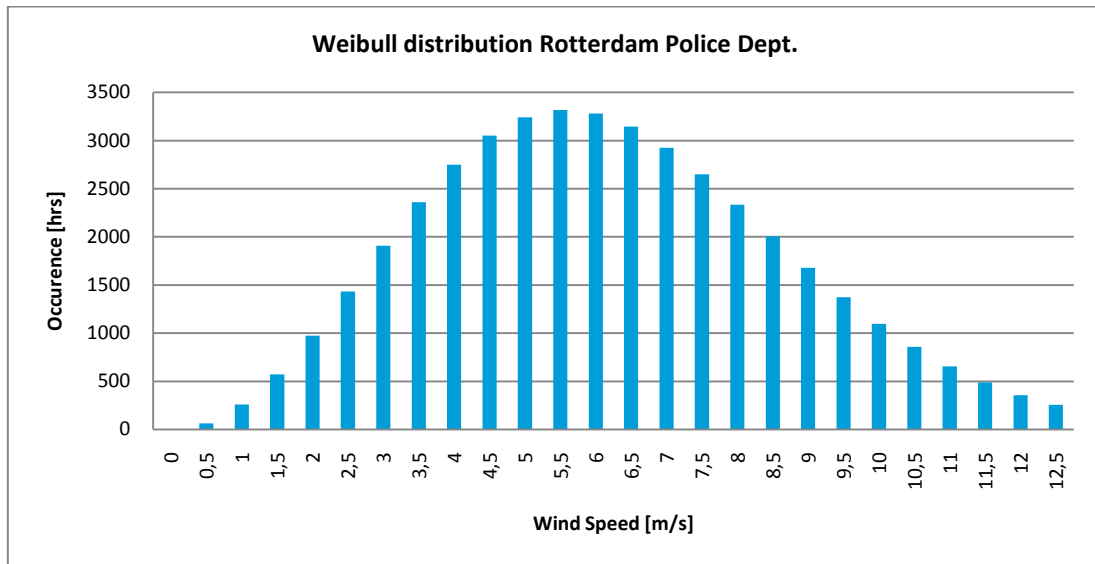


FIGURE 68: WEIBULL PLOT RPD

The velocity distribution combined with the cut-in speeds and the  $P_{gen}$ -V-curves, Figure 65, for the three blades result in the cumulative AEP graph for each blade, presented in Figure 69.

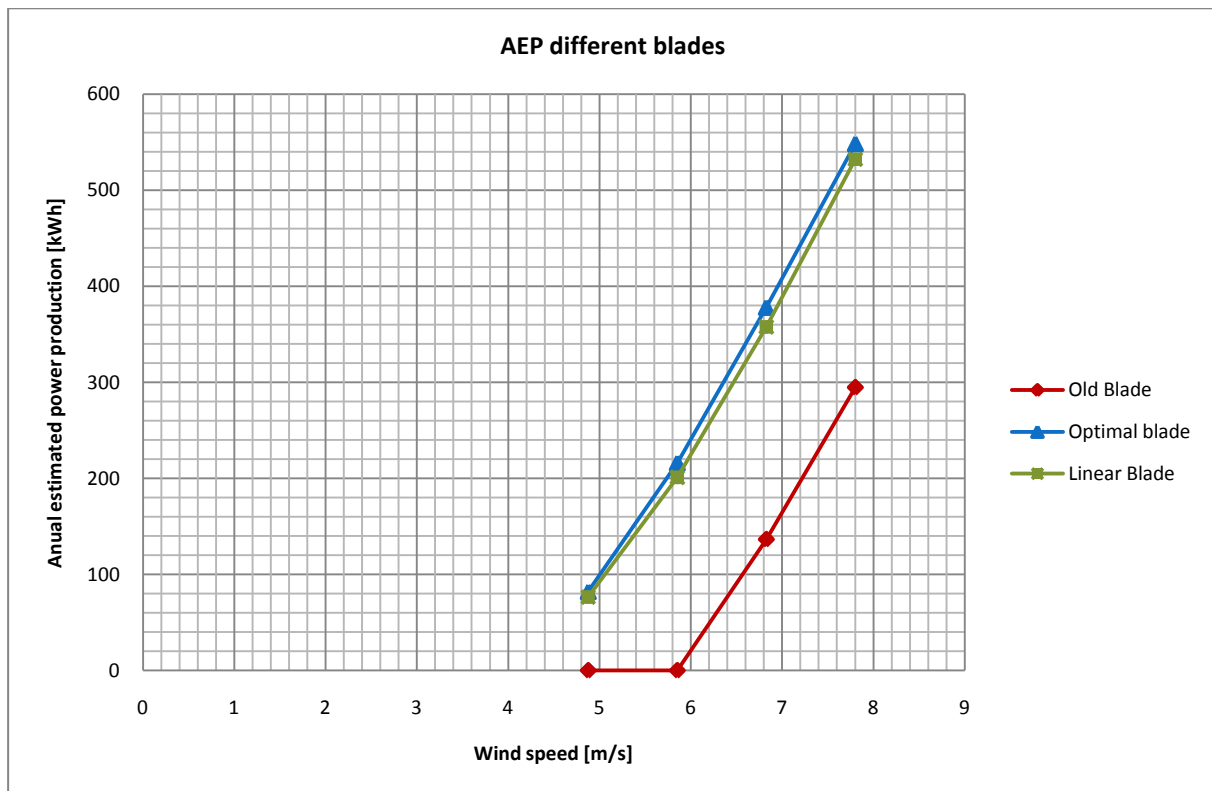


FIGURE 69: AEP FOR DIFFERENT BLADES

The optimal blade has an average cut in speed of around 3.2m/s, the linear blade a cut-in speed of 3.7m/s and the old blade shows an average cut-in speed of 6.2m/s. The Weibull distribution show that there are significant amount of hours of low wind speeds per year, leading to a higher AEP for the optimal and linear blades, as can be seen in Figure 69. The AEP with the optimal and linear blade is about 70% higher than the AEP with the old blade, this is because of the old blade's high cut-in speed and lower maximum power output.

The reduced cut-in speed explains why the optimal blade is producing more power than the linear blade, since the linear blade is outperforming the optimal blade only at higher wind speeds. When the AEP is made with the higher wind speeds, the linear blade will produce more energy in one year than the optimal blade.

### 5.1.6 COMPARISON WITH NUMERICAL MODEL

The power measurements presented in the current chapter can be compared to the obtained PV-curves from the numerical model to see whether the model represents the real world conditions. Figure 70 shows this graph. For this the measured PV-curve of the linear blade is used.

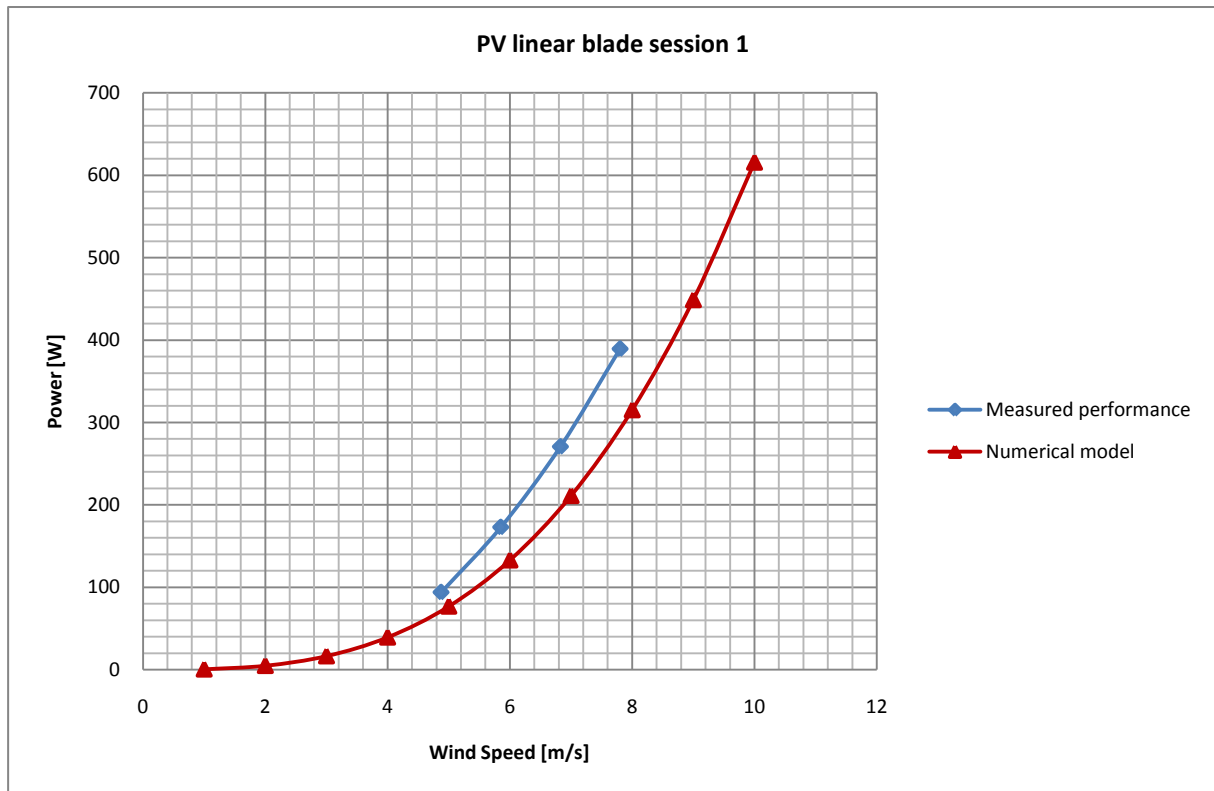


FIGURE 70: COMPARISON OF PV CURVES FROM TEST AND NUMERICAL MODEL

The model underestimates the output of the blade with 15% compared to measurements in the first test session. This can be caused by some simplifications in the model. The major simplification is the representation of the rotor blades by an actuator disk. Like this the actual flow over the blade is not modeled. As multiple tests with the DONQI URBAN WINDMILL show, the test results have always outperformed the calculated results [24].

### 5.1.7 DISCUSSION POWER MEASUREMENTS

The PV-curves for the old, optimal and the linear blades for both test sessions are presented in Figure 71. A strong discrepancy between the measurements in the first and second test session are noticeable for the optimal and linear blade. The performance of the optimal and the linear blade are reduced by 10%-15%. This discrepancy could be caused by:

- Electrical malfunctioning
- Aerodynamic changes
- Error in measurements

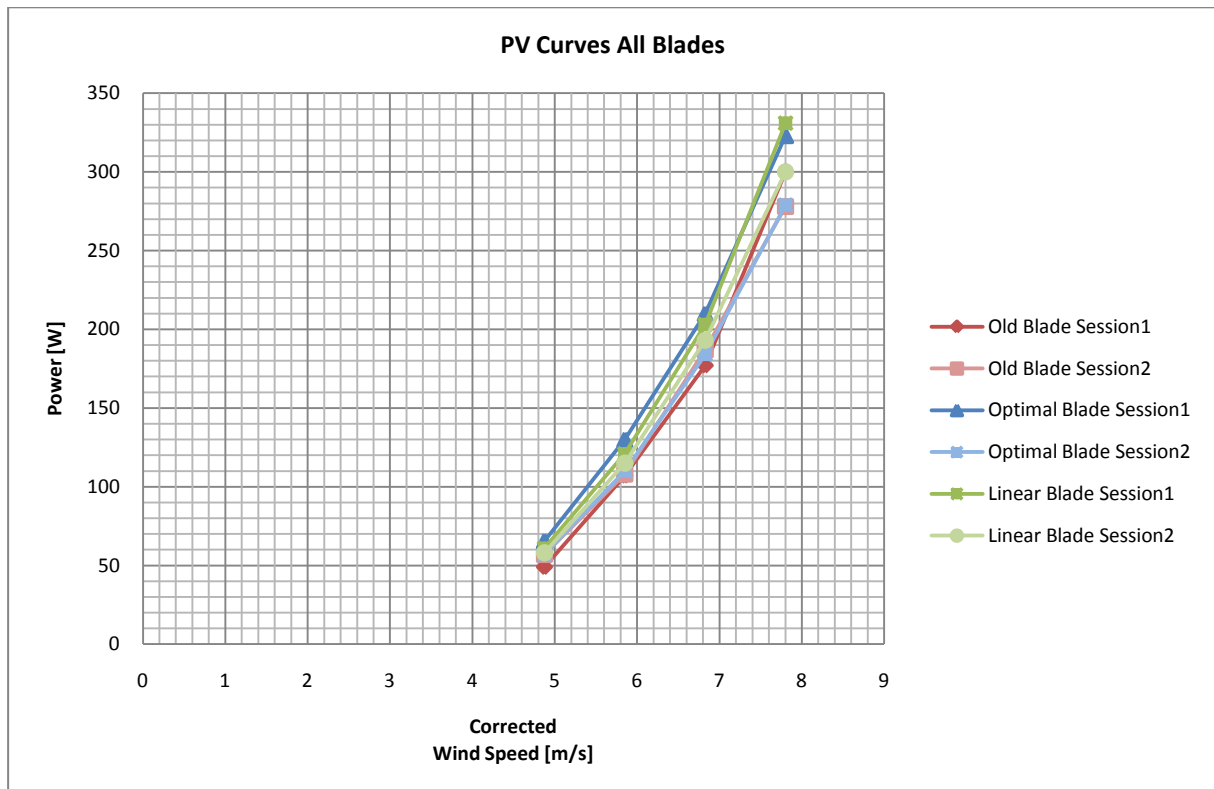


FIGURE 71: PV-CURVES THREE BLADES, SESSION 1 AND 2

To investigate the electrical malfunctioning, the connections were checked and the generator was tested, as described in paragraph 4.4. This resulted in excluding electrical malfunction from causing the reduced performance of the blades.

The discrepancy could be caused by a change in aerodynamic behavior. This is backed up by the fact that the old blade performs almost equal in both test sessions. The old blade is quite slender compared to the optimal and linear blade, and therefore less subjective to aerodynamic changes. The performed velocity measurements described in 5.2.2 confirms that the discrepancy can be caused by different aerodynamics. The blade connection in the hub might have played a role in this. The old blade is clamped in the hub with a fixed pitch angle and minimal movement, since it has a notch corresponding to a notch in the hub, disabling it to move. So all three the blades are in the exact same pitch angle. The pitch angle for the optimal and linear blades were set individually as described in 4.1.2. By fastening the bolts, the pitch angle could change a little,  $1^\circ$  or  $2^\circ$ , and the tilt angle of the blade changed as well, from  $0^\circ$  to  $5^\circ$ , causing the blade to perform different than desired. The tilt angle is the angle between the rotor plane and the blade. Although setting of the pitch angles was done with maximum precision, after tying and releasing the bolts several times, the plugs of the blades were slightly deformed, impeding the fixation of

the blades, and allowing it to tilt or rotate during the tests. This combined with rather heavy aluminum blades, 3 kg instead of 300g, lead to an unbalanced rotor, which also changed the aerodynamic behavior of the optimal and linear blades.

As was stated already in 5.1.2 a mistake in the measurements could have been made. The Pn-curves for the optimal blade in the first test session, Figure 59, show a wave-like shape. The Pn-curves for the optimal blade in the second test session, Figure 60, don not show this shape, but almost correspond to the local maximum of the measurement in the first test session. It is likely that if the measurements in the second test session were done for higher rotational speeds, the real maximum was found. An equal relation between the Pn-curves for the first and second test session are noticeable in the measurement with the linear blade, Figure 62 and Figure 63.

Also the Thrust-rotational speed curves for the optimal blade in the first and the second test session, Figure 72, confirms that it is likely that the measurements were not performed well. The thrust in the second test session is reduced with respect to the thrust in the first session. It seems as if the curves of the first test session are the extension of the curves in the second test session. It is therefore expected that if the measurements in the second test session were extended to higher rpm's the correct results would have been found.

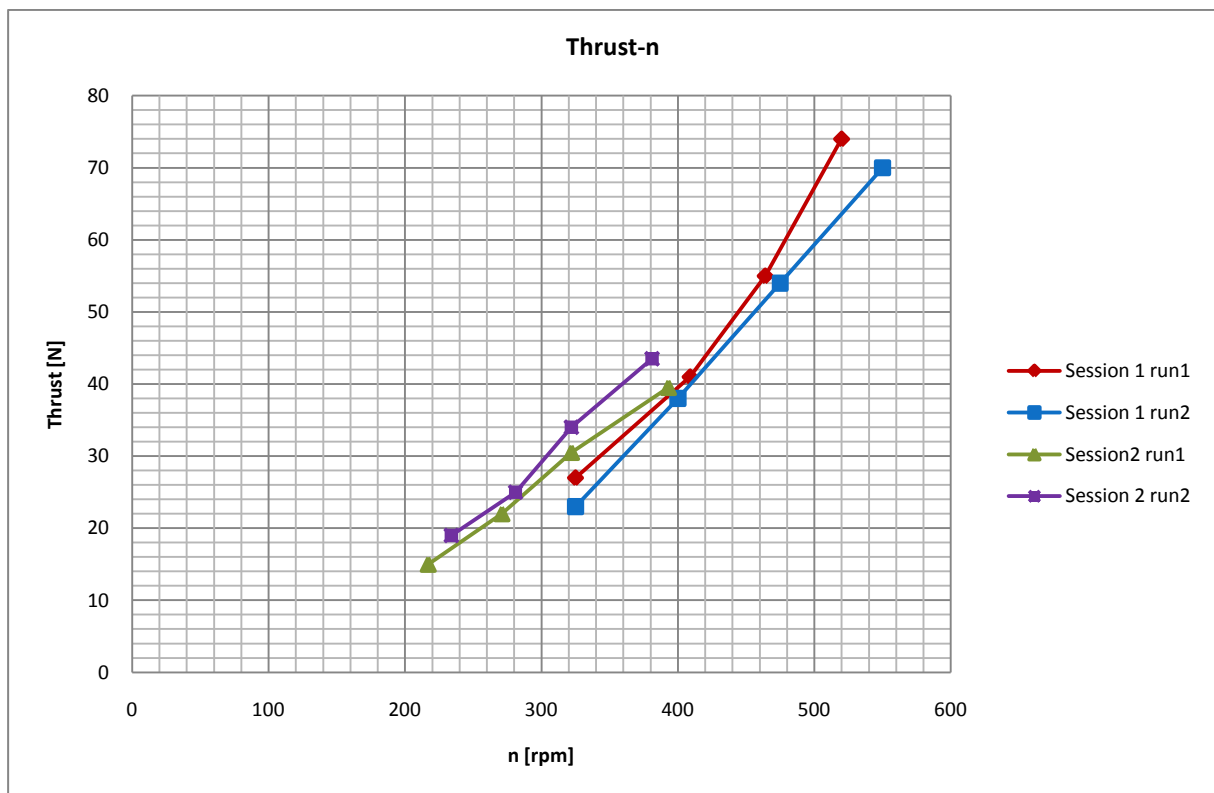


FIGURE 72: THRUST RPM CURVES OPTIMAL BLADE

The power coefficient-tip speed ratio plots shown in Figure 73 show that the DONQI URBAN WINDMILL performs best around a tip speed ratio between 5.5 and 6, cancelling the input of the tests in the second session. This tip speed ratio is slightly lower than the 6.2 used as a design input. The plot shows as well that for the old blade the optimal tip speed ratio is higher than for the new designed blades, but that the maximum power coefficient is lower. The velocity distributions in the next paragraph shows that the axial velocities for the old blade are lower

than for the optimal blade, resulting in a higher tip speed ratio. This can be caused by a lower thrust, resulting in a lower power coefficient. For the optimal blade the power coefficient is the highest. Figure 73 confirms that the measurement with the optimal and the linear blade in the second session are way off, providing sufficient ground to use the measurements of the first test session for the validation in the next paragraph.

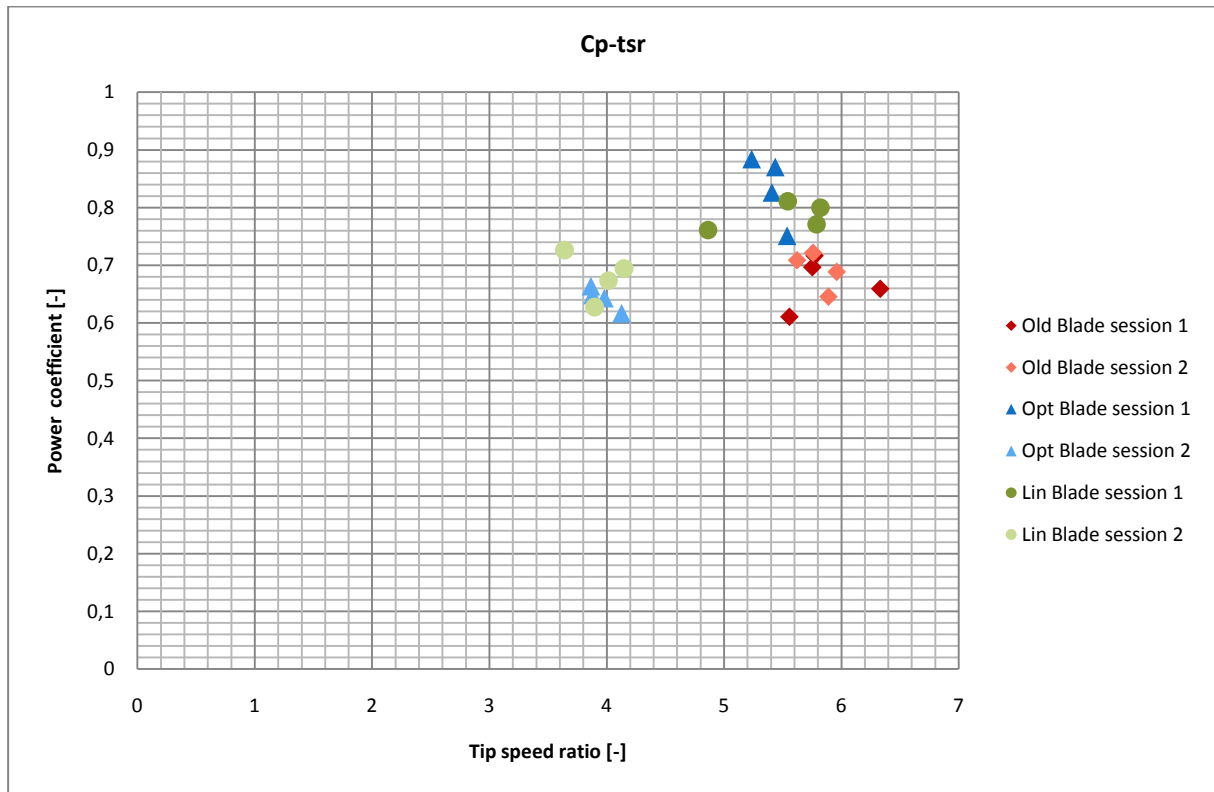


FIGURE 73: CP-TIP SPEED RATIO

## 5.2 MODEL VALIDATION

The numerical model can be validated with the performed force measurements and the velocity measurements at a certain thrust. This chapter presents these measurements and validate the numerical model with these results.

### 5.2.1 FORCE MEASUREMENTS

The axial force measurements were done simultaneously with the power measurements. This to measure at which thrust coefficient the DONQI URBAN WINDMILL performs best. The force measurements were also done to show whether the theory in paragraph 3.5.2, stating that the thrust on the diffuser and on the rotor should be in the same order of magnitude, holds. Starting with the latter Figure 74 shows the thrust coefficients for the old blade<sup>16</sup>:

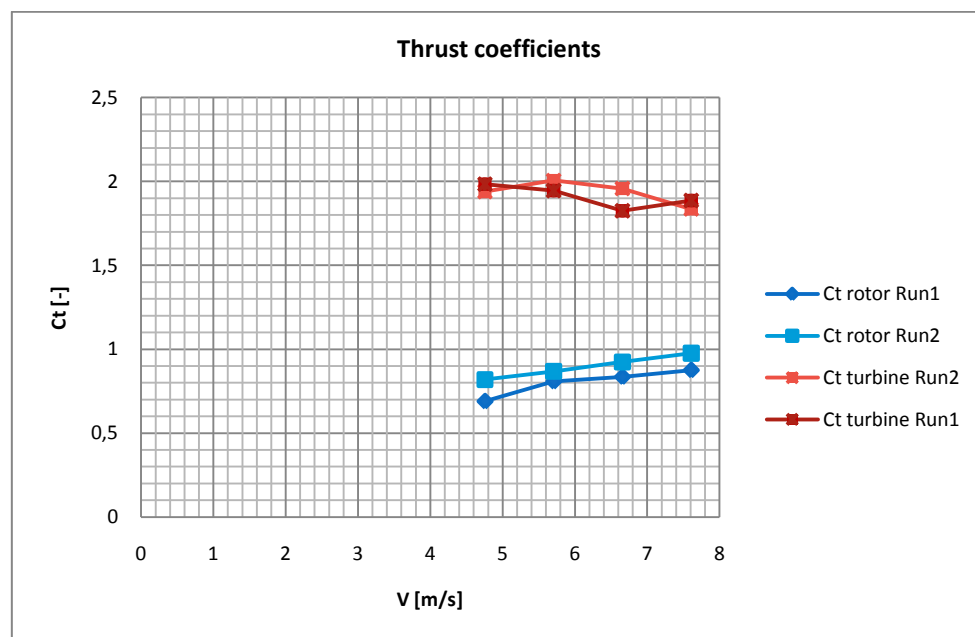


FIGURE 74: THRUST COEFFICIENTS ON DIFFUSER AND ROTOR

As can be seen the total force on the turbine is almost twice the force on the rotor, which is in agreement with the stated theory [15] and the results presented by Ten Hoopen [1].

The thrust coefficients at which the blades show the maximum power production are shown in Figure 75. The thrust coefficients are calculated with respect to the rotor area and the free wind speed. It is clear that the thrust on the optimal and linear blade are higher than the thrust at the old blade. The shape of the blade easily explains this, the increased chord of the optimal and linear blade cause higher thrusts on the blades, and these blades are designed for a more accurate axial velocity distribution.

For a certain wind speed the influence of the thrust coefficient on the power coefficient can be verified by creating  $C_T$ - $C_P$  curves. Doing this for the optimal and the linear blade in the first test session yields Figure 76 and Figure 77. These two graphs show that the blades have an optimal performance point around a thrust coefficient of 1.0-1.1. This is a bit higher than the  $\frac{8}{9}$  for which the model was run, but is a way of showing that the theory as developed by Konijn [27] is not

<sup>16</sup> Since with the old blade the total thrust measurements were most reliable

applicable for this specific DAWT, Since he states the optimal thrust coefficient is far below  $\frac{8}{9}$ . The other theories, Van Bussel [16], Lawn [20] and Werle and Presz [18] satisfy the results of the thrust measurements with the DONQI URBAN WINDMILL.

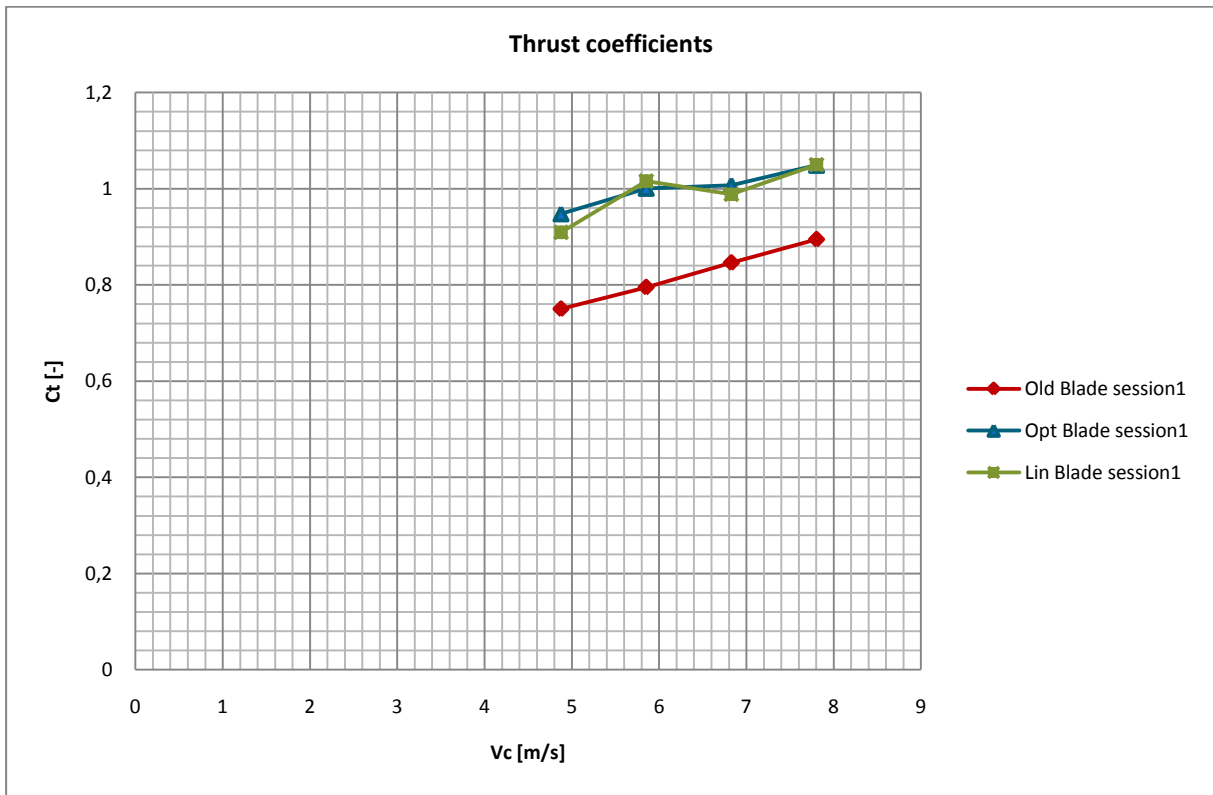


FIGURE 75: THRUST COEFFICIENTS FOR THE DIFFERENT BLADES

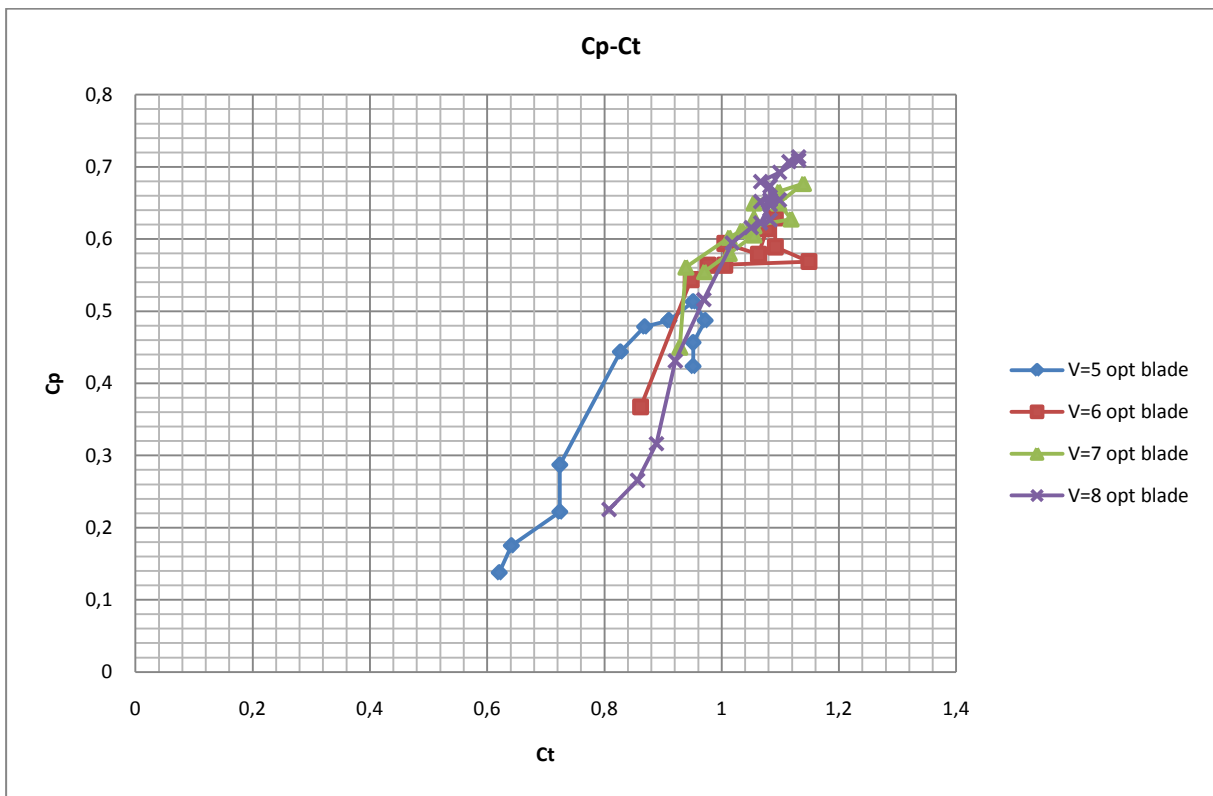


FIGURE 76: CP-CT FOR OPTIMAL BLADE

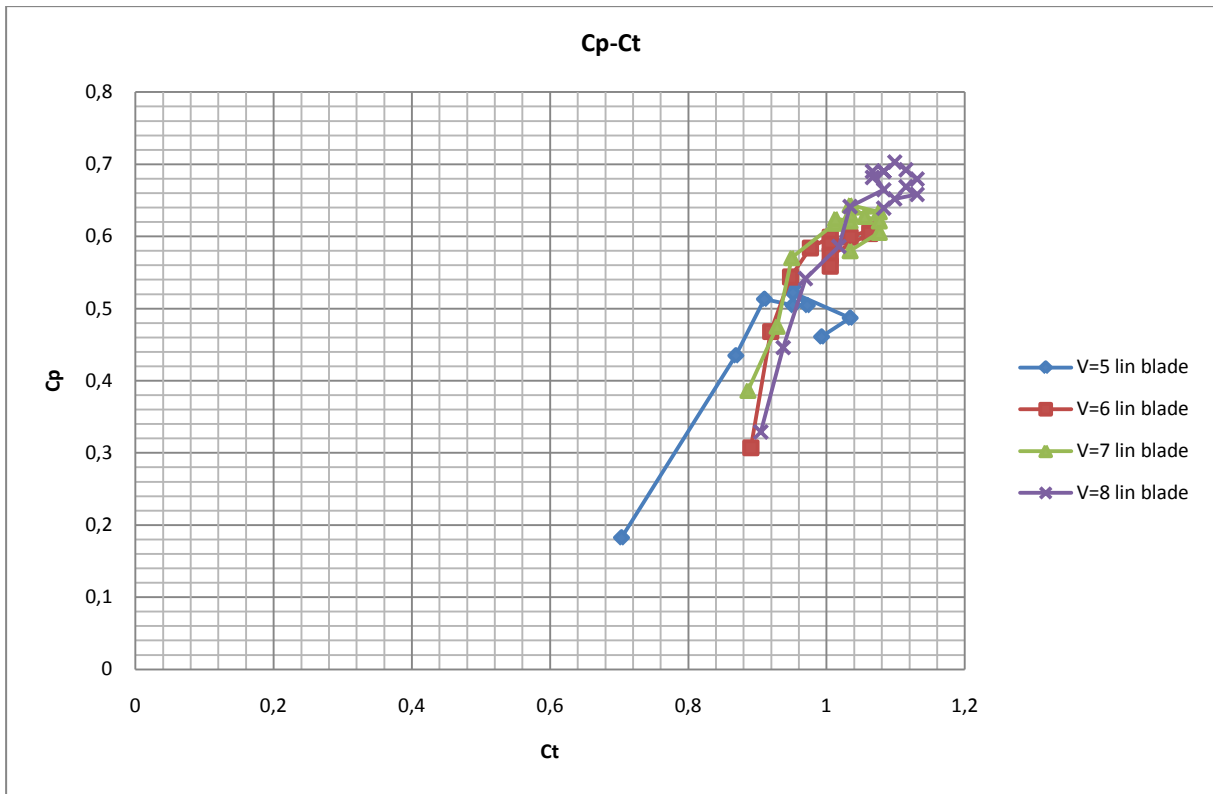


FIGURE 77: CP-CT FOR LINEAR BLADE

## 5.2.2 VELOCITY MEASUREMENTS

Most of the velocity measurements were done with the old blade and the linearized blade. For the optimal blade some measurements were done, due to limited availability of the measuring equipment. Fortunately, also three runs were done for an empty diffuser, to be able to compare this to an 'empty' run in the numerical model.

### 5.2.2.1 EMPTY DIFFUSER

In the case of an empty diffuser, the support structure of the generator is still in place. To include this in the comparison, the drag caused by these support trusses has to be calculated and transferred to a thrust coefficient, at which the model can be run, to obtain a calculated velocity distribution. Using a drag coefficient of 1.17<sup>17</sup> [37] for the cylindrical support trusses and the traversing mechanism, yields a thrust coefficient of 0.05[-], from now on referred to as  $C_{t,0}$ . If a comparison is made between the model and the measurements, the measured thrust coefficients have to be increased with  $C_{t,0}$  to get the  $C_t$  at which the model needs to be run, in this case that means the model is run at  $C_{t,0}$ , yielding the velocity distribution shown in Figure 78.

The velocity distribution obtained from measurements without the rotor present, by the five hole pitot tube is presented in this same graph as well. Three runs were made with an empty diffuser, at different free stream velocities. The curve that is shown in the modeled velocity distribution is not seen in the measured distribution. At the root the augmentation of the diffuser is underestimated and at the tip of the blade it is overestimated. This is mainly because the support truss is modeled as a screen with a certain thrust coefficient and that in the actual measurement the truss has a cross shape, and the measurements are done in a clearance in this cross as is seen in Figure 45, and are not hindered so much by these trusses.

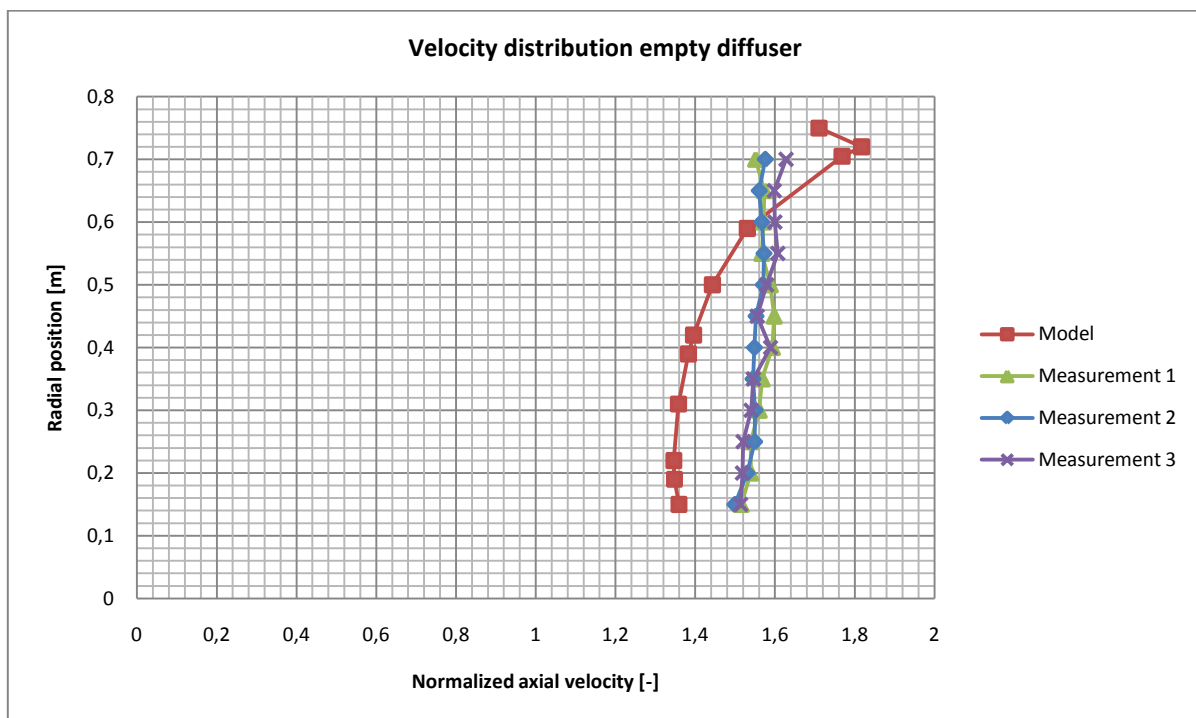


FIGURE 78: VELOCITY DISTRIBUTION EMPTY DIFFUSER

<sup>17</sup> For  $Re \geq e^4$

The shape of the hub was also different from the modeled shape. This was caused by two things. The tests were done with a generator that was different than the generator donQi was using at the moment the research was started. The shape of this generator was different and required a different support. A support was custom made to also be able to measure the thrust on the blades. The load cells that were measuring the forces had to be calibrated frequently, what prevailed to put a smooth tail on the rear side of the hub, as shown in chapter 4. The measurements with the empty hub had instead of the smooth shape as shown in Figure 14 a cylindrical shape.

### 5.2.2.2 VELOCITY MEASUREMENTS WITH OLD BLADE

Most of the velocity measurements were done with the old blade. One of the reasons was that this blade is smoother than the new blades, because of the fabrication method. Besides that, with the old blades, the test could be done with a bigger range of velocities as well, hopefully giving more insight in the results. To get different thrusts, the rotational speed was altered as well as the free stream velocity. As was already noted before, the pitch angle of the old blade cannot be changed. To be able to get some insight in the results of the old blade, different graphs were made for bins of the thrust coefficient.

The first two graphs, Figure 79 and Figure 80, show the velocity distribution for similar thrust coefficients with an equal free stream velocity, but with tests performed in the second and third week respectively. The difference that is noticed can explain the discrepancy between the power measurements that were done before and after these velocity measurements tests. The velocity at the root of the blades are significantly reduced in the third week. This is quite remarkable, since the turbine has not been moved over the weekend. Since it is the test with the old blade, the pitch angle is not altered either. Studying the flow angles measured by the five hole pitot tube could explain the discrepancy. The flow angles in the third week are much larger than those in the second week, more than double. The cause of this change in flow angles is not clear, especially since all the circumstances in the test were exactly equal in both cases, even the atmospheric conditions.

Part of the velocity distributions of the tests performed in the second week follow the shape of the modeled velocity. However the majority of the measurements are not comparable to the model.

In Figure 81 the measurements for the old blade with comparable thrust coefficients but different free stream velocities are shown. This graph is used to show the consistency between the measurements. The allover trend between the measurements and the model are comparable. However as seen before, the magnitude of the normalized velocity is again overestimated by the model. The difference between the different free stream velocities, all measured on the same day, can partly be explained when having a look at the flow angles, which are varying quite strong, despite the rotational velocity is varying proportionally for the different measurements. This behavior is confirmed by a similar graph for lower thrust coefficients in appendix F.

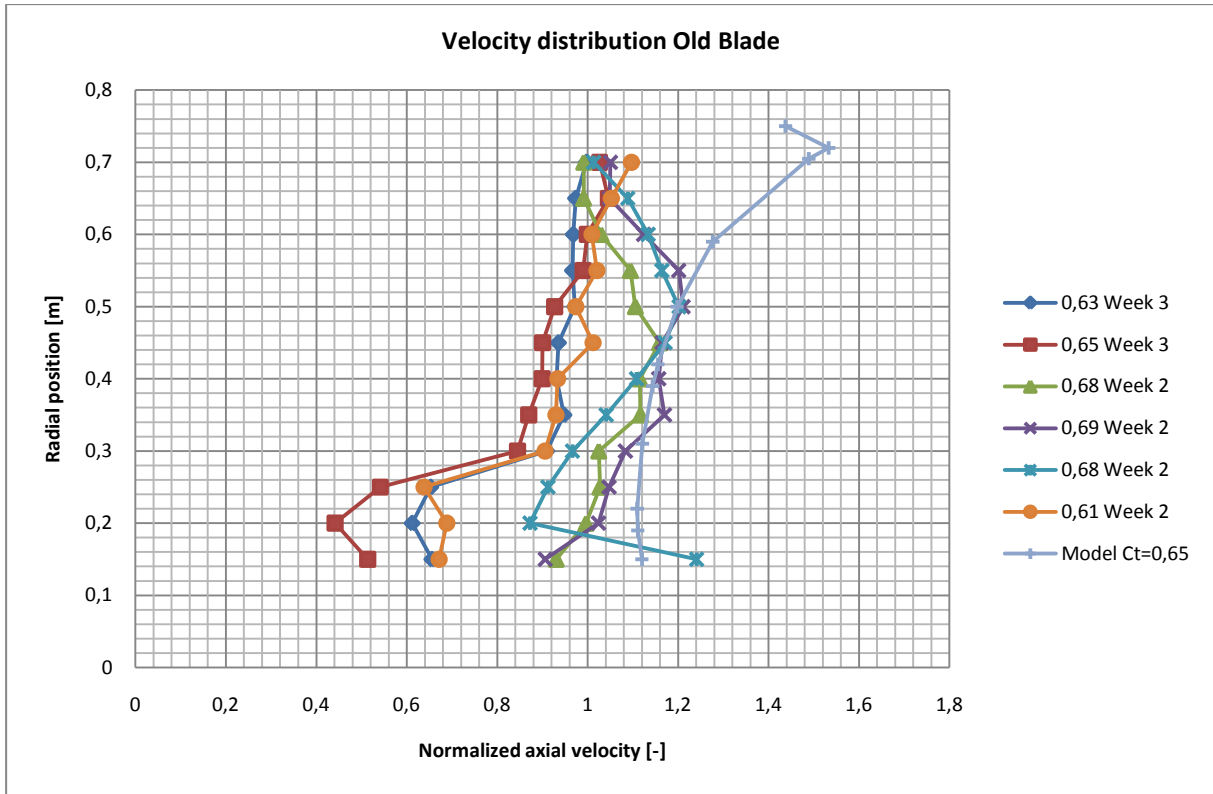


FIGURE 79: VELOCITY DISTRIBUTION OLD BLADE  $0.6 < C_t < 0.7$  AT  $V=10\text{M/S}$  WEEK 2-3

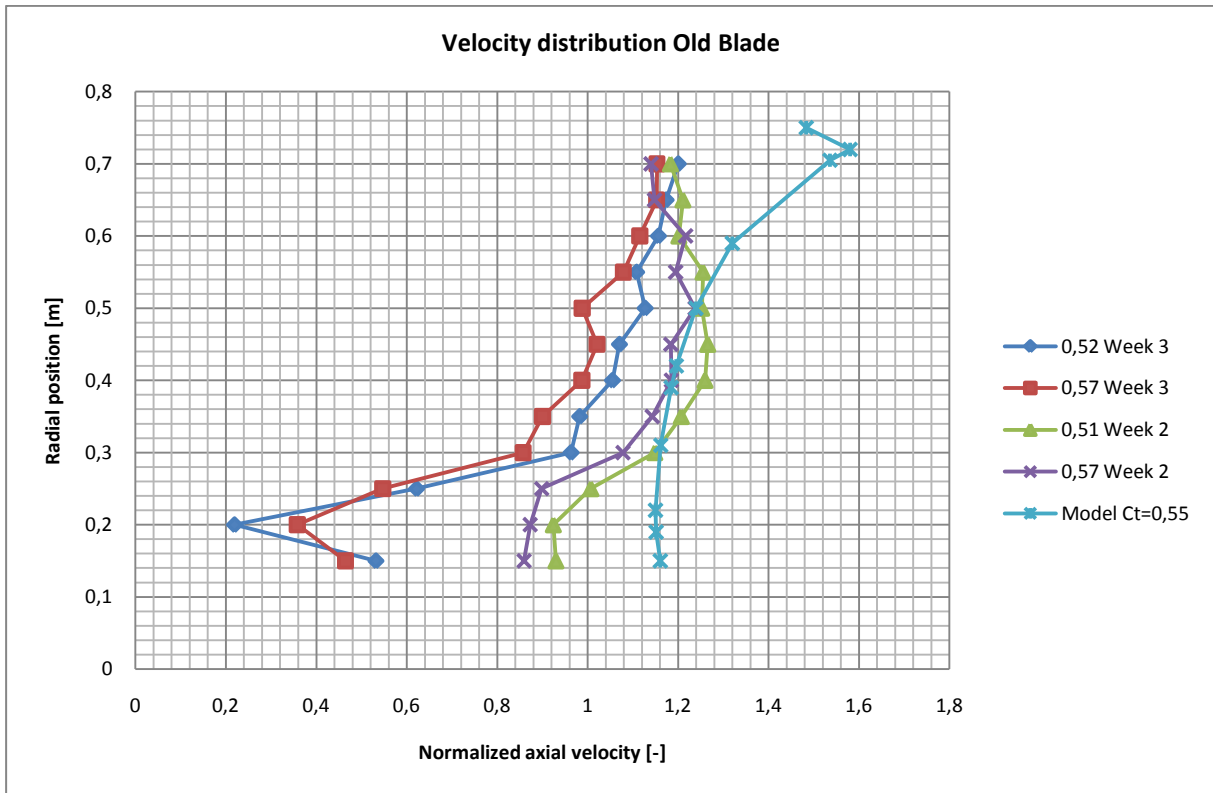


FIGURE 80: VELOCITY DISTRIBUTION OLD BLADE  $0.5 < C_t < 0.6$  AT  $V=10\text{M/S}$  WEEK 2-3

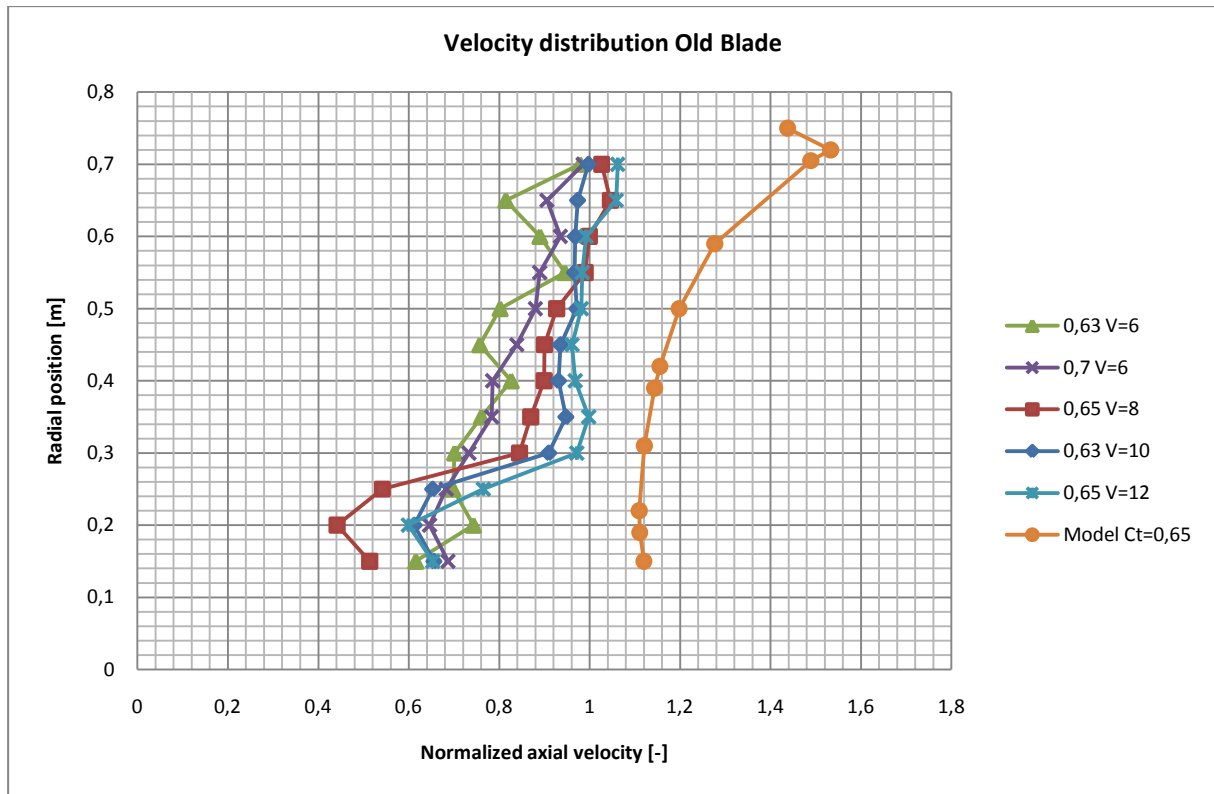


FIGURE 81: VELOCITY DISTRIBUTION OLD BLADE CT=0.65 V=6-12

### 5.2.2.3 VELOCITY MEASUREMENTS WITH OPTIMAL BLADE

The different thrust coefficients for the optimal blade were obtained by altering the rotational speed of the rotor blades with the controller at the same wind speed and the pitch angle was changed once from 10.5 degrees to 12.5 degrees. This change can be noticed clearly when looking at the blue, diamond marked line in Figure 82. This curve shows much lower axial velocities then the green, triangle marked line with the same thrust coefficient, of 0.54. An equal thrust coefficient was obtained by breaking the blades, and running the turbine at a lower rotational speed for the higher pitch angle. Looking at the data for the flow angles, as defined in Appendix B, can explain this, Table 4.

Flow angles	$\alpha$		$\beta$	
	Min	Max	Min	Max
Pitch=10.5°	6	8	0	7
Pitch=12.5°	9	19	3	15

TABLE 4: FLOW ANGLES, CT=0.54 AND PITCH=10.5/12.5

The flow angles for the session with a 12.5 degrees pitch are almost twice as big as for the session with a pitch angle of 10.5 degrees, it is therefore likely to assume separation in the session with the pitch angle of 12.5 degrees. Comparing the measurements with the velocity distribution obtained from the model gives something different as was found before, the trend is also that the velocity is increasing when approaching the diffuser, but the augmentations is underestimated by the numerical model.

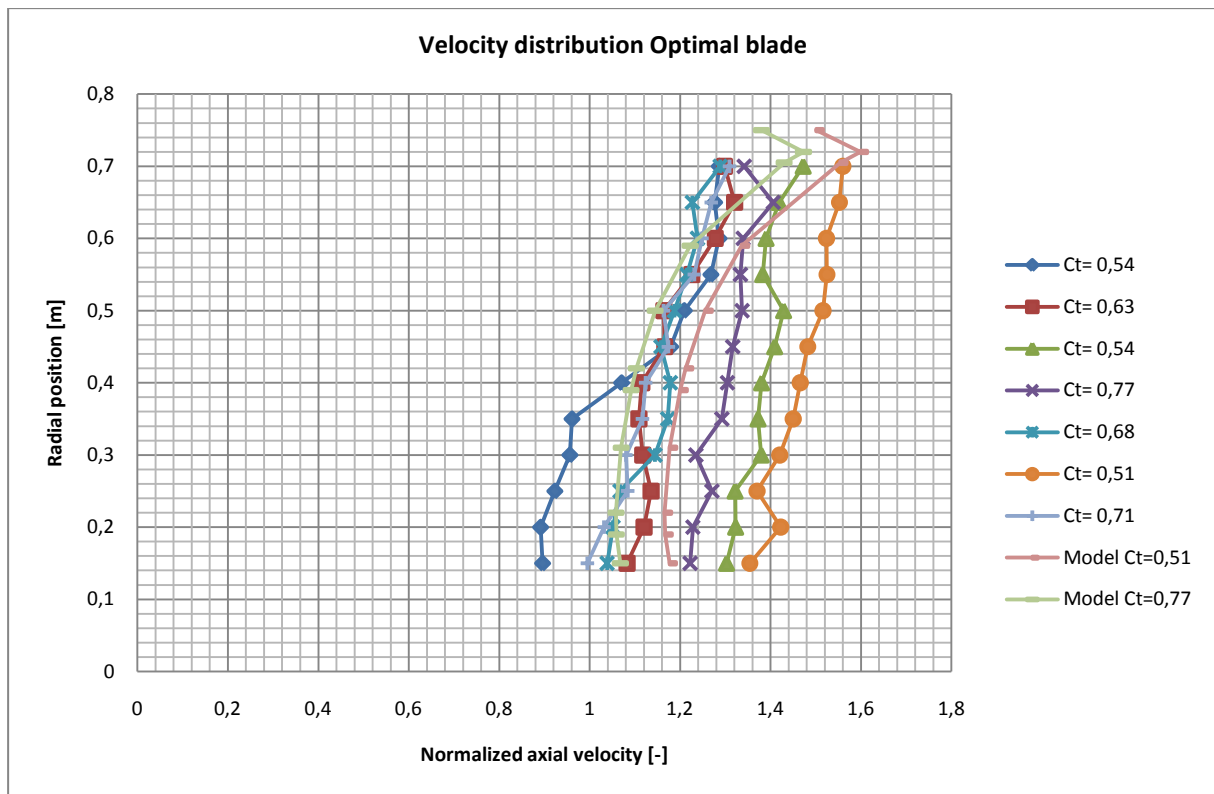


FIGURE 82: VELOCITY DISTRIBUTION OPTIMAL BLADE

Investigation of the change of the rotational speed for the different thrust coefficients show that it changes proportional with the thrust coefficient, some exceptions aside. This confirms that the tests are well executed and that the measurement tools were working properly.

#### 5.2.2.4 VELOCITY MEASUREMENTS WITH LINEAR BLADE

For the linear blade the velocity measurements are compared similar as for the old blade. However, for this blade all measurements are done with an equal wind speed, but with altered pitch angles<sup>18</sup>. As for the old blade, measurements were done in the second and in the third week. The first graph, Figure 83, shows a different trend as Figure 79 and Figure 80. Whereas in the two latter the measurements in the second week showed higher velocities than in the third week, the current graph shows the opposite. It has to be mentioned, that in this case, the pitch angles were not equal, 12.5 and 11.5 degrees for the second and third week respectively. The local angles of attack were different as well, caused by the difference in pitch and due to a higher rotational speed in the measurements in the third week, this indicate partial separation of the flow in the third week. The atmospheric conditions were equal. This difference together with a higher thrust coefficient could explain the discrepancy, which is not that big as well.

<sup>18</sup> Ranging between 7.5° and 12.5°

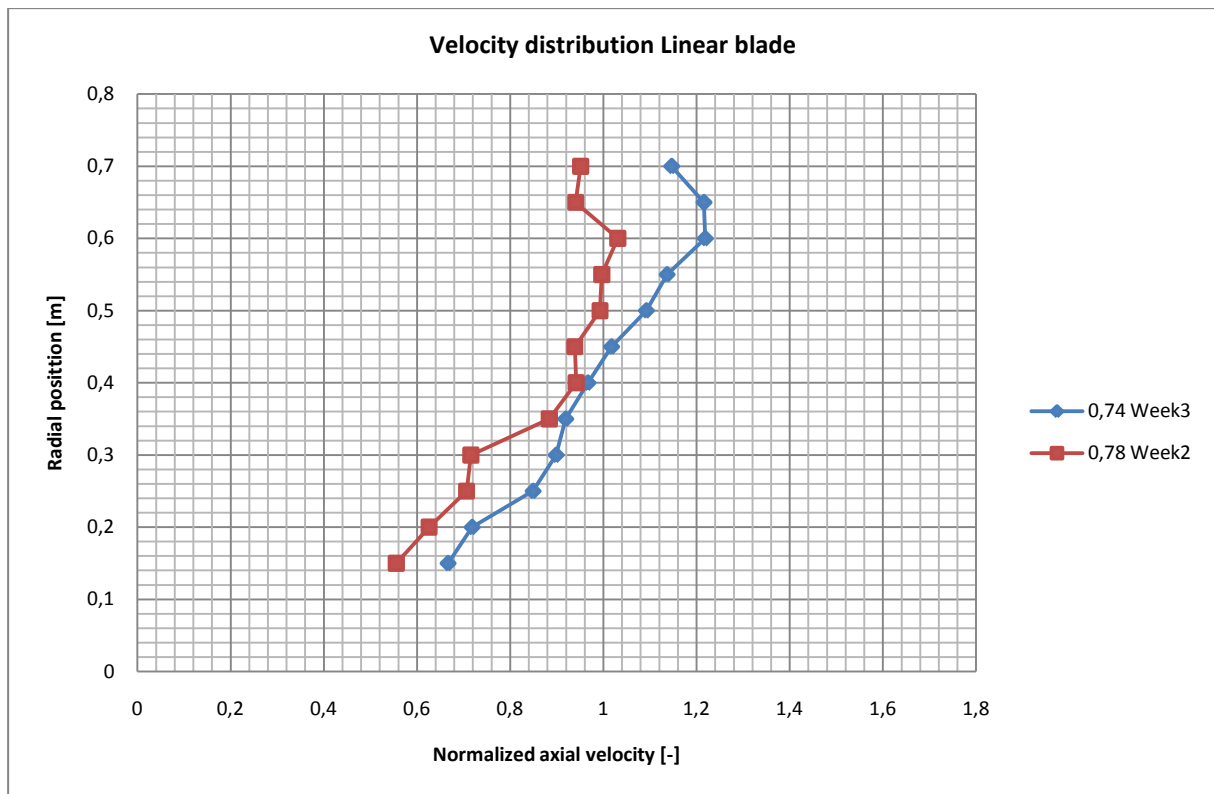


FIGURE 83: VELOCITY DISTRIBUTION LINEAR BLADE  $C_T=0.75$  DIFFERENT WEEKS AND PITCH

Whereas the flow angles in the third week measurements with the old blade were twice as big compared to the angles in the second week, this does not hold in the measurements with the linear blade. The angles in the second week are even slightly bigger. This could be caused by the axial position of the blade, more specific, its tilt angle. So there is a completely different flow acting on the blades in both measurements. Besides that, there is a reason to believe that the measurements in week three were not right, the rotational speed is significantly higher than for the other measurement, also the measurement done just before the third week measurement,  $C_T=0.74$ , gives a lower  $C_T$  for an even higher rotational speed, again indicating flow separation. Thus there is a reason to doubt the accuracy of the force/rpm measurement in the this series of measurements.

Figure 84 gives the velocity distribution for the measurements done with the linear blade with the same pitch angle, but different thrust coefficients set by the rotational speed. All measurements in Figure 84 show a reduced velocity at the root and the all over trend is equal. Comparing them with the results of the numerical model shows a similar trend, but an overestimation by the model. The three tests with an almost equal thrust coefficient show strong similarity.

It was checked whether the rotational velocity changes proportional with the thrust coefficients. For the majority of the tests in this section this conditions holds, meaning that the measurements were done correctly.

The problem with the measurements of the linear blade are that the steps in the pitch angle were quite big. Measurements were done with three different pitch angles, 7.5, 11.5 and 12.5, varying the angle of attack significantly, allowing the blades to act in stall, or with a much lower lift coefficient. This is noticeable in the comparison made between the extremes of the pitch angles, Figure 85. The difference between the thrust coefficient is not that big, however the

difference in axial velocity is much bigger than expected. This is probably caused by the large difference in pitch angles. Both measurements were done on the same day.

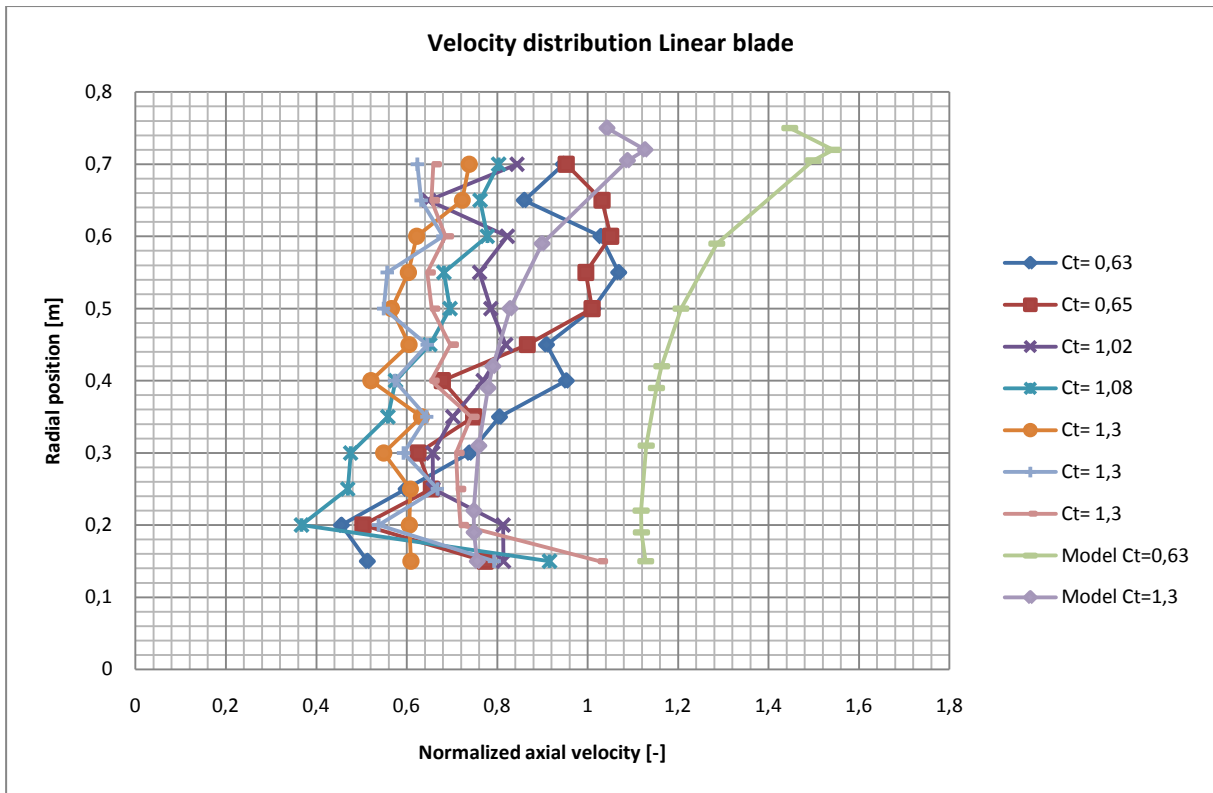


FIGURE 84: VELOCITY DISTRIBUTION LINEAR BLADE SAME PITCH, DIFFERENT CT

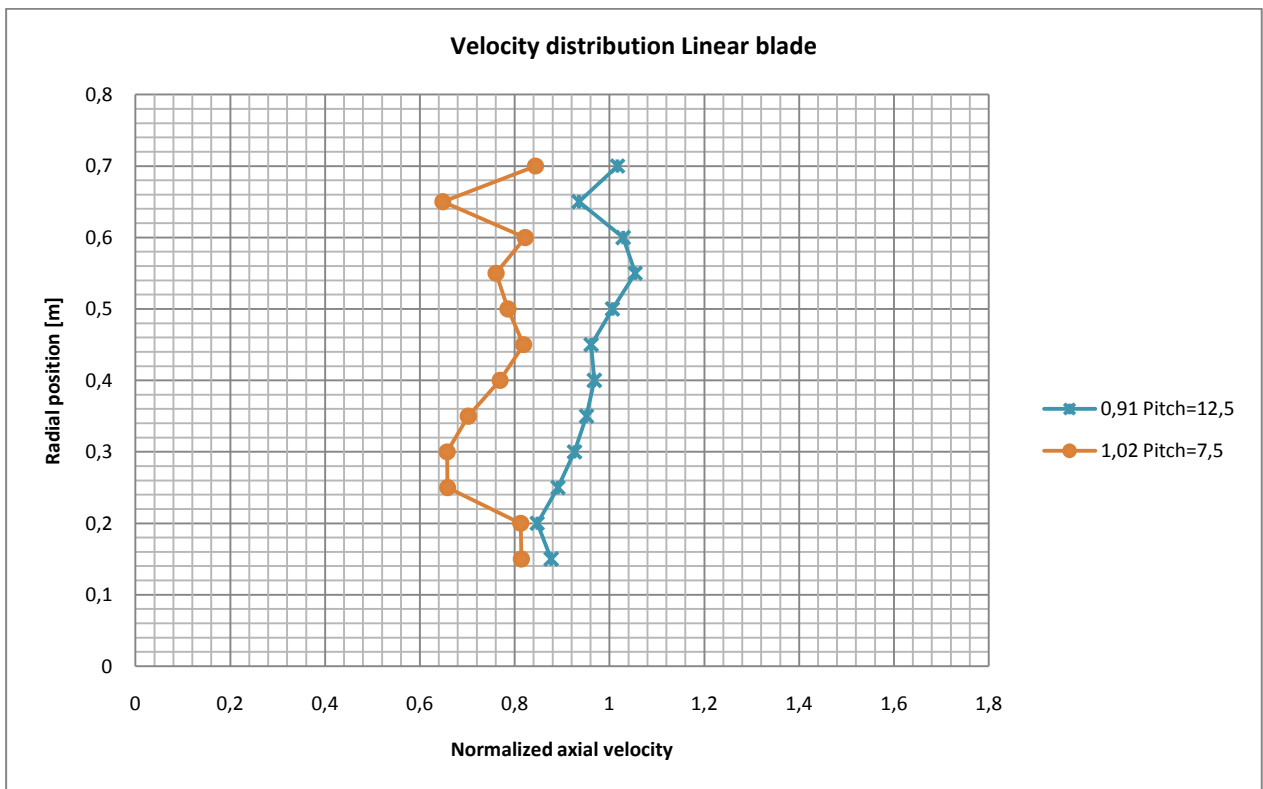


FIGURE 85: VELOCITY DISTRIBUTION LINEAR BLADE CT=0.95 PITCH=7.5-12.5

### 5.2.2.5 COMPARISON OF VELOCITY DISTRIBUTIONS DIFFERENT BLADES

The solidity of the three blades differ significantly, from 0.3-0.03 for the old blade to 1.7-0.06 for the optimal blade and 1.2-0.06 for the linear blade. Figure 86 is a summary of the other velocity distributions in this paragraph and shows that the solidity is an important parameter in the decision whether the rotor blades are allowed to be represented by an actuator disk. As was seen already, the optimal blade is quite well represented by the numerical model. For the other blades the model is quite off. This is because the model does not distinguish between the different blades, since they are replaced by a disk with a certain thrust. Since the velocity distribution calculated by the numerical model is the basis for the optimal blade, Figure 86 provides sufficient validation for the use of the developed model to design an aerodynamic optimal blade. The linearized blade is derived from this blade, so it should be very close to its optimal shape.

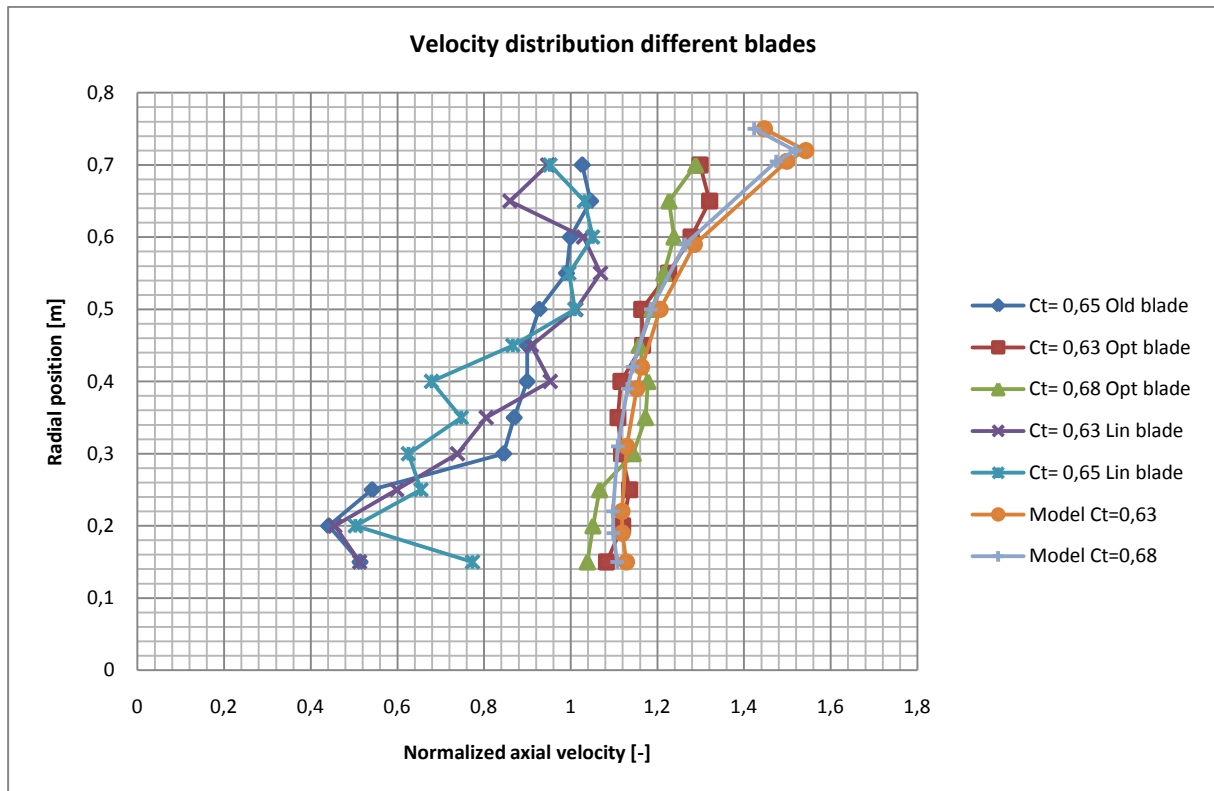


FIGURE 86: VELOCITY DISTRIBUTION DIFFERENT BLADES, CT=0.63-0.68

### 5.3 DISCUSSION EXPERIMENTS

---

The difference in the power measurements between the first and the second session cannot be explained completely. The extra tests performed with the generator learned that the electronics of the generator and the test set up are working properly. These tests do offer a nice bonus: the relation between the generator power and the mechanical power is found and can be used to transfer the results of the OJF tests from generator power to mechanical power, providing the opportunity to get a better validation of the developed numerical model. The power measurements show quite a resemblance with the numerical model, whereas this is not the case for all the velocity measurements, except for the optimal blade. This is explained by the solidity of the optimal rotor. The numerical model is based on an actuator disk, representing the rotor blades, so the higher the solidity yielding the same thrust, the better the model will resemble the OJF tests, as shown by the tests with the different blades, since flow separation is avoided like this<sup>19</sup>. The lower the solidity, the worse the model resembles the tests. So for designing a high solidity rotor the model serves the goal quite well. For a low solidity rotor the model is still an improvement of what was available so far. A significant reduction in computational time was achieved by the use of the vortex cylinder and root vortex. It requires a couple of seconds to calculate a new blade geometry, whereas the model of Ten Hoopen [1] requires at least multiple minutes to obtain a velocity distribution.

The linearized blade is chosen to replace the old blade of the DONQI URBAN WINDMILL, based on the power output and on the production costs. The power output at higher velocities is the best for the linearized blade. The production costs are determined by the shape and the volume of the blade. The shape of the optimal blade is quite complicated, besides that, it also requires more material. Therefore, the production costs for the linearized blade will be lower than those for the optimal blade. Comparing the production cost for the linearized blade to those of the old blade learns that the old blade costs about €8.50 per set and the linearized blade €13.50, so a cost increase of about 50%. However, the power provided by the linearized blade can be 15% higher than that of the old blade and moreover the annual performance of the DONQI URBAN WINDMILL can be increased with 70%, this basically due to the reduced cut in speed with the new blades. Next to these incentives, the new blade will also serve a commercial role: a revolving rotor in the DONQI URBAN WINDMILL will be sold better than a non-revolving one. The blade will be produced through hand lay-up, in a mold that is created by a CNC-machine.

The velocity measurements provide a reason to think that a slightly better blade can be produced. This because the velocities measured with the linear blade installed are lower than the velocities that are the basis of the optimal blade geometry. Iterating the blade design in the numerical model, extended with a lifting line method, can provide a new velocity distribution and therefore a new and possibly improved blade design.

---

<sup>19</sup> Due to lower rotational speed



## 6 CONCLUSIONS AND RECOMMENDATIONS

This chapter contains the main conclusions of the executed research, which are used to answer the main research question asked in the second chapter of this report:

*"How to design an improved rotor for the DONQI URBAN WINDMILL?"*

First the partial conclusions are presented in this chapter, required to answer the main research question. This chapter will be closed with some recommendations on future research and improvements on the numerical model.

### Conclusions

Currently the DONQI URBAN WINDMILL is equipped with three quite slender blades. The maximum measured power coefficient during the tests involved in this research was 0.71 based on the rotor swept area. This is significant higher than the theoretical maximum power coefficient for a bare turbine, which is  $\frac{16}{27}$ . The goal of the performed research was to increase the power coefficient of the DONQI URBAN WINDMILL. This goal is achieved, the power coefficient of the DAWT is increased with 15%, the annual power production with 70% and the cut in wind speed is reduced with 100%, for an increase in cost of 50%.

The old blade design was based on CFD calculation by NLR, which was off. The two new blade designs were achieved by first calculating the velocity distribution at the rotor location of the DONQI URBAN WINDMILL. The velocity distribution is calculated with an axisymmetric surface vorticity model in which the rotor was modeled by a vortex cylinder and a root vortex. The strengths of the vortex cylinder and root vortex are determined by the optimal theoretical rotor loading of  $\frac{8}{9}$ . The obtained velocity distribution is used as a basis to calculate the optimal blade geometry with a Blade Element Momentum numerical model with wake rotation.

The velocity distribution is verified with bare turbine theory, by running the numerical model with an increased and decreased diffuser. This provides similar results for an optimal rotor loading as the model was expected to give for a bare wind turbine case. The pressure distribution obtained from previous research and the numerical model were compared and showed a strong resemblance as well.

Two types of new blades were designed. The basis for an optimal blade geometry is a velocity distribution at the rotor location of the DAWT when the thrust coefficient is set to  $\frac{8}{9}$ . This optimal geometry on its turn is linearized on some sections to obtain a simplified blade geometry. This linearized blade has the advantage that the production costs are reduced with respect to the optimal blade, since the total volume of the blade has been reduced and the geometry is simplified. These two new blades and the old blade of the DONQI URBAN WINDMILL are tested in the Open Jet Facility of Delft University of Technology in a production turbine of DONQI. This production turbine is equipped with custom-made force measurement tools and a traversing 5-hole pitot tube to obtain the thrust and a corresponding 3D velocity distribution in the diffuser.

The OJF power measurements showed that the optimal and linearized designed blades clearly outperform the old blade design, by 15% as a maximum measured power coefficient. The power coefficients of the optimal and linearized blade are 0.88 and 0.81 respectively. The optimal and the linearized blades have a slightly different airfoil than the old blade. The two new blades have a NACA 2207 airfoil and the old blade has this same airfoil but combined with a 6% nose drop, providing slightly better aerodynamic features.

Comparing the annual estimated production for a specific location in The Netherlands shows that the new blades will produce up to 70% more energy per year, 540 kWh/year compared to 300kWh/year. The increased performance is mainly caused by halving the cut-in speed, to approximately 3m/s. Besides that, the higher maximum power output contributes as well. The optimal blade provides a lower cut-in speed than the linearized blade, but the latter performs better at increased wind speeds. The increased root section of the optimal blade causes too much drag at higher wind speeds, allowing the linear blade to produce better under these circumstances. Next to this, the linear blade is easier and cheaper to be produced, making the linear blade the desired blade for the future generation of DONQI URBAN WINDMILLS. The cost of the linearized blade is about 50% higher than the costs of the old blade. This is however outweighed by the extra produced energy and finally, a rotating blade is favorable over a non-rotating one from a marketing point of view.

A strong discrepancy is seen between the power measurements in two different test sessions. This is probably due to a mistake in the measurements in the second test session. Therefore, it is decided to focus on the results of the first test session.

The axial force measurements allow to relate the maximum power point to the exerting rotor loading. This gave insight in the optimal rotor loading of a DAWT. From the performed experiments, it could be concluded that the optimal rotor loading for the DONQI URBAN WINDMILL is 1.1 with respect to the rotor area. This is quite close to the optimal rotor loading for bare turbines, as previous research have indicated. This also shows that the theory developed by Lawn [20] can be used for this specific turbine. Force measurements have shown as well that the axial force on the rotor and on the diffuser are balancing each other. Van Bussel [15] already predicted this was the case and this is demonstrated with the tests performed in the current research.

The numerical model is validated by velocity measurements behind the rotor at different radial positions. These measurements are done with a 5-hole pitot tube, yielding a 3D velocity distribution. The 3D distribution is required to be able to have a better comparison between the different measurements. For the validation mainly the axial velocities are used. They are normalized with the free stream velocities corrected for wind tunnel blockage. The velocity measurements with the optimal blade matches the modeled velocity distribution quite well. However, the measurements with the old blade and the linearized blade do not match the modeled distribution. The model overestimates the measured velocity distribution for these two types of blades. This can be explained by looking at the solidity of the rotor. The numerical model does not distinguish between different blade geometries, but uses an actuator disk with a certain loading. The optimal rotor has a much higher solidity and is similar to a screen with a certain loading, so the measurements are more likely to approximate the calculated results.

A fast operating design code is developed to obtain an optimal rotor blade for a DAWT. The successive steps followed are listed below:

- Create a mesh for the diffuser
- Calculate the self induction of the diffuser
- Calculate the strength of the vortex cylinder and root vortex
- Calculate the influence of diffuser, rotor and vortex collocation points on one another
- Obtain the velocity distribution through the diffuser
- Iterate the velocity calculations until convergence is obtained
- Match the blade element forces with momentum change over the rotor
- Obtain blade geometry

## Recommendations

The developed numerical model can be expanded with a lifting-line approach, to represent the rotor blades, to update the velocity distribution after the linearized blade is designed. If this is programmed in a separate module, it can be iterated until convergence is obtained, possibly yielding an improved design. The costs for this will be significant extra computational time.

For improved blockage correction more research is required on horizontal buoyancy and blockage correction for rotating test specimens. The current way of calculating the blockage corrections assumes a solid frontal surface, assuming a thrust coefficient comparable to that of a solid circle, equal to 1.2. Often wind turbine rotors are not loaded up to such a high thrust coefficient. It is suggested in this research to scale the blockage correction with the ratio of the measured thrust coefficient with that of the solid circle. To validate this, more research is required and a CFD study could be part of this.

Future research could lead to integrated diffuser and rotor design. A way to do this could be equating the thrust of the diffuser to that of the rotor blades. So if first the velocity distribution for an existing design is calculated and based on that an improved rotor design is made, the thrust on the rotor blades is known. With this thrust the design of the diffuser can be adapted, yielding a new velocity distribution through the diffuser. These calculations should be iterated until convergence is obtained.



## LIST OF FIGURES

FIGURE 1: TRIAS ENERGETICA .....	7
FIGURE 2: COSTS OF ENERGY IN THE NETHERLANDS [3] .....	17
FIGURE 3: WIND DISTRIBUTION URBAN ENVIRONMENT VS GRASS LAND (DOTTED LINE); FIGURE ADAPTED FROM [7] .....	18
FIGURE 4: UK AND US SMALL WIND TURBINE SALES [8] [9] .....	18
FIGURE 5: DONQI URBAN WINDMILL .....	18
FIGURE 6: IMPRESSIONS OF DAWT'S; GRUMMAN AEROSPACE, VORTEC 7 AND DONQI URBAN WINDMILL .....	19
FIGURE 7: BARE WIND TURBINE [23] .....	20
FIGURE 8: DIFFUSER [23].....	20
FIGURE 9: EJECTOR [23] .....	20
FIGURE 10: AXIAL VELOCITY AT THE ROTOR POSITION [26] AND ADAPTED FROM [1].....	22
FIGURE 11: CONTROLE VOLUME AS USED BY VAN BUSSEL AND WERLE&PRESZ .....	25
FIGURE 12: MAXIMUM POWER AS FUNCTION OF TURBINE RESISTANCE [20].....	30
FIGURE 13 BIOT-SAVART LAW.....	31
FIGURE 14: DIMENSIONS OF DIFFUSER.....	33
FIGURE 15: PANEL DISTRIBUTION DIFFUSER AND HUB .....	33
FIGURE 16: REAL MODELING ACTUATOR DISK .....	34
FIGURE 17: ACTUAL MODELING ACTUATOR DISK [29] .....	34
FIGURE 18: 2D VISUALISATION OF VORTEX CYLINDER .....	35
FIGURE 19: 3D VISUALISATION OF VORTEX CYLINDER AND ROOT VORTEX .....	35
FIGURE 20: CALCULATION OF AXIAL AND TANGENTIAL VELOCITY .....	36
FIGURE 21: ROOT VORTEX .....	38
FIGURE 22: BLADE ELEMENT FORCES .....	41
FIGURE 23: VELOCITY DISTRIBUTION WITH INCREASED DIAMETER .....	43
FIGURE 24: VELOCITY DISTRIBUTION WITH REDUCED CHORD .....	43
FIGURE 25: CP VERIFICATION .....	44
FIGURE 26: INDUCED VELOCITIES, TANGENTIAL(RED) AND AXIAL (GREEN) .....	45
FIGURE 27: AXIAL VELOCITIES ON ROTOR ELEMENTS FOR VARIOUS CT'S.....	46
FIGURE 28: CHORD DISTRIBUTIONS .....	47
FIGURE 29: TWIST DISTRIBUTIONS .....	47
FIGURE 30: 3D CAD DRAWINGS .....	48
FIGURE 31: FDM MODEL .....	48
FIGURE 32: VARIOUS STAGES IN GRINDING AND SANDING .....	48
FIGURE 33: RAW SAND-CASTED BLADE .....	48
FIGURE 34: PV CURVES OF NEW BLADES .....	49
FIGURE 35: GENERATOR AND HUB .....	51
FIGURE 36: GENERATOR .....	51
FIGURE 37: PITCH MEASURING .....	52
FIGURE 38: SETTING THE PITCH ANGLE .....	52
FIGURE 39: BUILT UP THRUST MEASUREMENT .....	52
FIGURE 40: THRUST MEASUREMENT .....	52
FIGURE 41: THE HAMMOCK .....	53
FIGURE 42: LOAD CELL .....	53
FIGURE 43: CALIBRATION .....	53
FIGURE 44: CALIBRATION EQUIPMENT.....	53
FIGURE 45: TRAVERSING MECHANISM .....	54
FIGURE 46: 5 HOLE PITOT TUBE .....	54
FIGURE 47: FLOWCHART POWER MEASUREMENTS .....	55
FIGURE 48: FLOWCHART VALIDATION MEASUREMENTS .....	56
FIGURE 49: OJF TEST SET UP .....	57
FIGURE 50: GENERATOR CHECK.....	60
FIGURE 51: OLD BLADE .....	63

FIGURE 52: OPTIMAL BLADE .....	63
FIGURE 53: LINEARIZED BLADE .....	63
FIGURE 54: PV CURVE OLD BLADE .....	64
FIGURE 55: PN CURVES OPTIMAL BLADE SESSION 1 RUN1 .....	65
FIGURE 56: PN CURVES OPTIMAL BLADE SESSION1 RUN2 .....	65
FIGURE 57: PN CURVES OPTIMAL BLADE SESSION2 RUN1 .....	66
FIGURE 58: PN-CURVES OPTIMAL BLADE SESSION2 RUN2 .....	66
FIGURE 59: PV CURVES OPTIMAL BLADE SESSION 1.....	67
FIGURE 60: PV CURVES OPTIMAL BLADE SESSION 2.....	67
FIGURE 61: PV-CURVES OPTIMAL BLADE .....	68
FIGURE 62: PV CURVES LINEAR BLADE SESSION1 .....	69
FIGURE 63: PV-CURVES LINEAR BLADE SESSION2.....	69
FIGURE 64: PV CURVE LINEAR BLADE .....	70
FIGURE 65: OPTIMAL PV-CURVES THREE BLADES, CORRECTED FOR TUNNEL BLOCKAGE.....	71
FIGURE 66: OPTIMAL PV-CURVES, CORRECTED FOR BLOCKAGE AND GENERATOR EFFICIENCY .....	71
FIGURE 67: CP CURVES DIFFERENT BLADES .....	72
FIGURE 68: WEIBULL PLOT RPD .....	73
FIGURE 69: AEP FOR DIFFERENT BLADES .....	73
FIGURE 70: COMPARISON OF PV CURVES FROM TEST AND NUMERICAL MODEL .....	74
FIGURE 71: PV-CURVES THREE BLADES, SESSION 1 AND 2 .....	75
FIGURE 72: THRUST RPM CURVES OPTIMAL BLADE .....	76
FIGURE 73: CP-TIP SPEED RATIO .....	77
FIGURE 74: THRUST COEFFICIENTS ON DIFFUSER AND ROTOR.....	78
FIGURE 75: THRUST COEFFICIENTS FOR THE DIFFERENT BLADES.....	79
FIGURE 76: CP-CT FOR OPTIMAL BLADE .....	79
FIGURE 77: CP-CT FOR LINEAR BLADE.....	80
FIGURE 78: VELOCITY DISTRIBUTION EMPTY DIFFUSER .....	81
FIGURE 79: VELOCITY DISTRIBUTION OLD BLADE $0.6 < CT < 0.7$ AT $V=10M/S$ WEEK 2-3 .....	83
FIGURE 80: VELOCITY DISTRIBUTION OLD BLADE $0.5 < CT < 0.6$ AT $V=10M/S$ WEEK 2-3 .....	83
FIGURE 81: VELOCITY DISTRIBUTION OLD BLADE $CT=0.65$ $V=6-12$ .....	84
FIGURE 82: VELOCITY DISTRIBUTION OPTIMAL BLADE.....	85
FIGURE 83: VELOCITY DISTRIBUTION LINEAR BLADE $CT=0.75$ DIFFERENT WEEKS AND PITCH.....	86
FIGURE 84: VELOCITY DISTRIBUTION LINEAR BLADE SAME PITCH, DIFFERENT CT.....	87
FIGURE 85: VELOCITY DISTRIBUTION LINEAR BLADE $CT=0.95$ PITCH=7.5-12.5 .....	87
FIGURE 86: VELOCITY DISTRIBUTION DIFFERENT BLADES, $CT=0.63-0.68$ .....	88
FIGURE 87: $C_p$ POLAR FOR A BARE DIFFUSER.....	104
FIGURE 88: FRONT VIEW.....	105
FIGURE 89: VELOCITY ANGLE RELATIVE TO PRESSURE PROBE .....	105
FIGURE 90: CALIBRATION GRAPH A .....	106
FIGURE 91: CALIBRATION GRAPH B .....	106
FIGURE 92: CALIBRATION.....	106
FIGURE 93: ACTUATOR DISK MODEL (THE BLUE LINE IS THE DISK) .....	107
FIGURE 94: POWER-RPM PLOTS FOR THE TESTED GENERATOR AND ANOTHER GENERATOR.....	111
FIGURE 95: TORQUE RPM FOR TESTED GENERATOR AND ANOTHER GENERATOR.....	111
FIGURE 96: DIFFERENCE MEASURED $P_{MECH}$ AND $P_{GEN}$ FOR VARIOUS RPM .....	112
FIGURE 97: PN CURVES FOR DIFFERENT SOFTWARE AND GENERATOR .....	112
FIGURE 98: PN CURVES LINEAR BLADE SESSION 1 RUN 1 .....	113
FIGURE 99: PN CURVES LINEAR BLADE SESSION 1 RUN 2 .....	113
FIGURE 100: PN-CURVES LINEAR BLADE SESSION2 RUN1 .....	114
FIGURE 101: PN-CURVES LINEAR BLADE SESSION2 RUN2 .....	114
FIGURE 102: VELOCITY DISTRIBUTION OLD BLADE $CT=0.55$ $V=6-12$ .....	115
FIGURE 103: FLOW ANGLES OLD BLADE $CT=0.55$ $V=6-12M/S$ .....	115
FIGURE 104: VELOCITY DISTRIBUTION LINEAR BLADE, PITCH=12.5.....	116
FIGURE 105: VELOCITY DISTRIBUTION DIFFERENT BLADES, $CT=0.51-0.57$ .....	116
FIGURE 106: VELOCITY DISTRIBUTION DIFFERENT BLADES, $CT=0.7-0.9$ .....	117

---

## LIST OF TABLES

---

TABLE 1: US AND GLOBAL SMALL WIND TURBINE SALES IN 2009 [9]	18
TABLE 2: SPECIFICATION DONQI URBAN WINDMILL	21
TABLE 3: THRUST COEFFICIENTS OF ROTOR AND DIFFUSER	44
TABLE 4: FLOW ANGLES, $CT=0.54$ AND $PITCH=10.5/12.5$	84



---

## REFERENCES

---

1. **Hoopen, P.D.C. Ten.** *An Experimental and computational Investigation of a Diffuser Augmented Wind Turbine; With an application of vortex generators on the diffuser trailing edge.* 2009.
2. **Stankovic, Campbell and Harries.** *Urban Wind Energy.* London, United Kingdom : Earthscan, 2009. 978-1-84407-282-8.
3. **Commission, European.** Eurostat. [Online] [Cited: September 14, 2010.] [http://epp.eurostat.ec.europa.eu/portal/page/portal/energy/data/main\\_tables](http://epp.eurostat.ec.europa.eu/portal/page/portal/energy/data/main_tables).
4. —. [Online] [Cited: September 14, 2010.] [http://ec.europa.eu/environment/climat/climate\\_action.htm](http://ec.europa.eu/environment/climat/climate_action.htm).
5. **Government, Dutch.** [Online] [Cited: September 14, 2010.] <http://www.rijksoverheid.nl/onderwerpen/duurzame-energie/doel-20-duurzame-energie>.
6. **Initiative, Rotterdam Climate.** [Online] [Cited: September 14, 2010.] [http://www.rotterdamclimateinitiative.nl/nl/50\\_minder\\_co\\_sub\\_2\\_sub/over\\_het\\_programma/over\\_het\\_programma\\_50\\_minder\\_co\\_sub\\_2\\_sub](http://www.rotterdamclimateinitiative.nl/nl/50_minder_co_sub_2_sub/over_het_programma/over_het_programma_50_minder_co_sub_2_sub).
7. **Mertens, S.** *Wind Energy in the Built Environment; Concentrator Effects of Buildings.* Delft : Multi Science, 2006. 0906522-35-8.
8. **Renewable UK.** *Small Wind Systems; UK Market Report April 2010.* London : s.n., 2010. [www.renewable-uk.com](http://www.renewable-uk.com).
9. **AWEA: American Wind Energy Association.** *Small Wind Turbine Global Market Study; Year ending 2009.* Washington DC, US : s.n., 2010. [www.awea.com/smallwind](http://www.awea.com/smallwind).
10. **Phillips, D.G.** *An investigation on Diffuser Augmented Wind Turbine Design.* Auckland, Australia : University of Auckland, 2003.
11. *Fluid Dynamic Aspects of Wind Energy conversion.* **Vries, O. de.** 1979, AGARDograph 243.
12. *Research and Development for Shrouded Wind Turbines.* **Igra, O.** 1981, Energy conversion & Management, 21:13-48.
13. *Preliminary Design and Economic Investigations of Diffuser Augmented Wind Turbines DAWT.* **Foreman, K.M.** [ed.] Research Department Grumman Aerospace. New York : s.n., 1981.
14. *Experiments With a Diffuser Augmented Wind Turbine.* **Foreman, K.M. and Gilbert, B.L.** [ed.] Grumman Aerospace. 105, 1983, Journal of Energy Resources Technology, pp. 46-54.
15. *An Assessment of the Performance of Diffuser Augmented Wind Turbines.* **Bussel, G.J.W. van.** [ed.] Delft University of Technology. Delft : s.n., 1999, Proceedings of the 3th ASME Joint Fluids Engineering Conference July 18-23, 1999, San Francisco, California.
16. *The science of making more torque from wind: Diffuser experiments and theory revisited.* **Bussel, G.J.W. van.** [ed.] Delft university of technology. Delft : s.n., 2007, Journal of physics: Conference series 75.
17. *Effect of placing a diffuser around a wind turbine.* **Hansen, M.O.L.** [ed.] Technical University of Denmark. Lyngby : s.n., 2000, Wind energy; 2000;3; 207-213.

18. *Ducted Wind/Water Turbines and Propellers Revisited*. **Werle, M.J. and Jr., W.M. Presz.** Massachusetts : s.n., September-October 2008, Journal of Propulsion and Power, pp. 1146-1151. Vol 24, No 5.
19. *Generalized Limits for Energy Extraction in a Linear Constant Velocity Flow Field*. **Jamieson, P.** [ed.] Garrad Hassan. Glasgow : s.n., Wind Energy; 2008; 11; 445-457.
20. *Optimization of the power output from ducted turbines*. **Lawn, C.J.** London : University of London, 10 31, 2002, Proceedings of the Institution of Mechanical Engineers, Part A: Journal of Power and Energy.
21. *Potential Flow Calculations of Axisymmetric Ducted Wind Turbines*. **Widnall, S.** s.l. : Massachusetts Institute of Technology, July 2009.
22. **Hoopen, P.D.C. Ten.** *A Literature Study and Experimental Investigation of a Diffuser Augmented Wind Turbine; In the Preparation of the Final Msc. Thesis Work.* 2009.
23. *Concentrator systems for Wind Energy, with Emphasis on Tipvanes*. **Holten, T. van.** 1, Delft, Netherlands : Wind Engineering, 1981, Vol. 5, pp. 29-45.
24. **Heijden, K. van der.** *Interview with Kasper van der Heijden.* 02 2010.
25. **(NLR), National Aerospace Laboratory.** *Evaluatie en verbetering van de prestaties van een kleinschalige diffusor augmented wind turbine (dawt); 1e fase.* 2008.
26. **(NLR), National Aerospace Research Laboratory.** *Ontwerp van een kleinschalige diffusor augmented wind turbine (dawt); 2e fase.* 2008.
27. *One Dimensional Flow Theory for Diffuser Augmented Wind Turbines*. **B.J. Konijn, H.W.M. Hoeijmakers, F. Jaarsma, B.I. Soemarwoto, K.M.J. de Cock.** Twente/Amsterdam : University of Twente and NLR, July 2010.
28. **Lewis, R.I.** *Vortex Element Methods for Fluid Dynamic Analysis of Engineering Systems.* Cambridge : Cambridge University Press, 1991. ISBN: 13 978 0 521 36010 4.
29. **Burton, Sharpe, Jenkins, Bosanyi.** *Wind Energy Handbook.* Sussex England : John Wiley&Sons Ltd., 2008. 978-0-471-4997-9.
30. *Lecture Notes AE4-W12: Lecture 9, Vortex Line Wake Model / Vortex Wake Model / Acceleration Potential Method*. **Bussel, G.J.W. van.** Delft : TUDelft, 2009.
31. *Lecture Notes 4P720 Aerodynamics of Wind Turbines, Part 1, Principles of Energy Extraction and Blade Element Momentum Theory*. **Snel, G. Schepers and H.** Eindhoven : TU/e and ECN, October 16, 2009.
32. **J. Katz, A. Plotkin.** *Low Speed Aerodynamics, From Wing Theory to Panel Methods.* San Diego State University : McGraw-Hill Inc, 1991. 0-07-050446-6.
33. **Cooper, K.** *Bluff Body Blockage Corrections in Closed and Open-Test-Section Wind Tunnels.* Neuilly sur Seine-France : AGARD-AG 336 Wind Tunnel Wall Correction, 1998. pp. 6-1 - 6-33.
34. **Barlow, J.B., Rae, W.H. and Pope, A.** *Low Speed Wind Tunnel Testing.* New York : John Wiley and Sons, 1999. ISBN- 0-471-55774-9.
35. **Timmer, W.M.** *Interview with Nando Timmer on Wind tunnel correction.* Delft, September 8, 2010.

36. **B.M. van Wijk, F.M. Yemer.** *Urban wind Resource Assessment, a case-study at the available wind resources at the building of the Rotterdam Police Dept.* s.l. : Delft University of Technology, 2010.
37. **Hoerner, S.F.** *Fluid Dynamic Drag, theoretical, experimental and statistical information.* Bakersfield : Hoerner Fluid Dynamics, 1965.
38. **Samuelsson, I.** *Low speed windtunnel investigation of propeller slipstream aerodynamic effects on different nacelle wing combinations.* s.l. : Technical Report, 1990.
39. *Das Maximum der theoretisch möglichen Ausnützung des Windes durch Windmotoren.* **Betz, A.** 1920, Zeitschrift für das gesamte Trubinenwesen 1920: 20: 307-309.



---

## APPENDICES

---

Appendix A: Problem of decoupling the duct from the rotor design

Appendix B: Calibration of 5-hole pitot tube

Appendix C: Theories

Appendix D: Test overview

Appendix E: Generator tests

Appendix F: More test results

## APPENDIX A: PROBLEM OF DECOUPLING THE DIFFUSER FROM THE ROTOR DESIGN

As Jamieson [19] describes a velocity distribution at the location of the rotor has to be obtained, without a rotor present. This can be done in some ways:

- Running the bare diffuser in a computational model
- Using measurements of a bare diffuser

The problem of using the bare diffuser configurations can be explained with the help of Figure 87. This figure shows the pressure distribution over the diffuser annular airfoil, of the DONQI URBAN WINDMILL. It can be seen that at 85% chord the flow starts to separate. This means that without the rotor present, the flow will not be fully attached to the diffuser, as was also witnessed during experiments without a rotor [1].

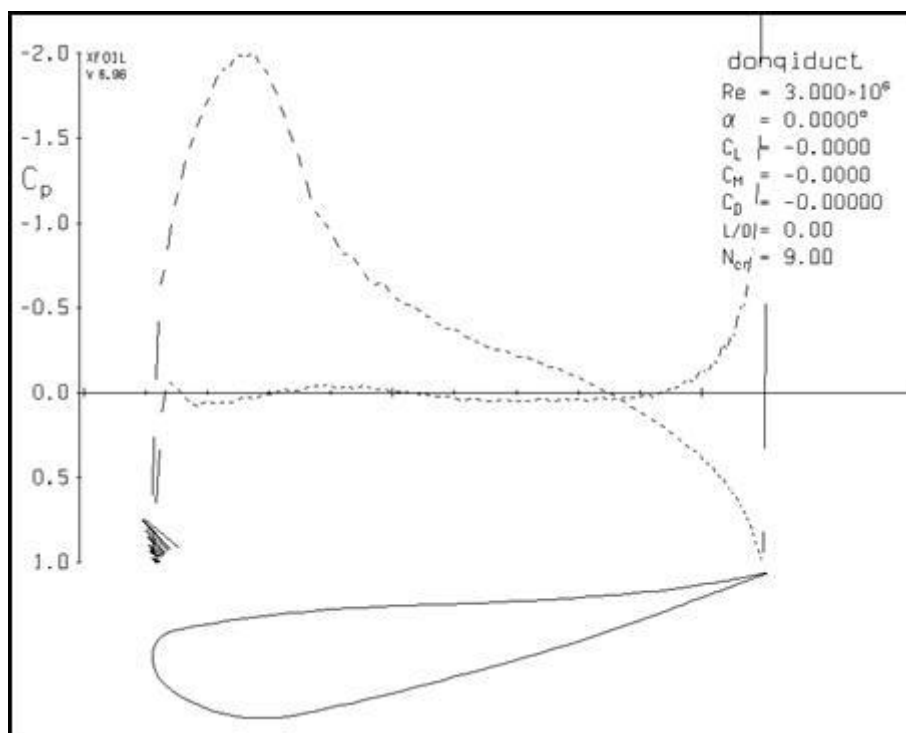


FIGURE 87:  $C_p$  POLAR FOR A BARE DIFFUSER

With a rotor present the flow is attached on the duct. This because of two things:

- The local angle of attack is reduced because of the force exerted on the flow by the rotor.
- The rotor causes a pressure jump in the flow through the duct.
- The velocity of the flow at the diffuser wall is highest, this energizes the boundary layer of the diffuser [17].

This shows that decoupling is not applicable for a DAWT rotor design study and that this theory by Jamieson [19] can not be used in the current research to design a rotor for the DONQI URBAN WINDMILL.

## APPENDIX B: 5 HOLE PITOT TUBE

Obtained from Ten Hoopen [1]:

This appendix contains a description of the mathematical scheme used to derive the various angles and velocities from the measured 5 hole pressure probe readings. The 5 hole pressure probe is calibrated according to Samuelsson's calibration scheme [38] used in the investigation of propeller slipstream nacelle/wing interactions. The 5 hole pressure probe used is depicted in Figure 89 and is calibrated in the low speed wind tunnel at Delft University of Technology.

Through the use of a LABVIEW measurement application it was possible to obtain the pressure measurements from the 5 hole pressure probe. The pressure readings were referenced to the atmospheric pressure  $p_{ref}$  in the Open Jet Facility. From the 5 pressure readings it was possible, with the use of the calibration data, to derive the flow angles and velocities.

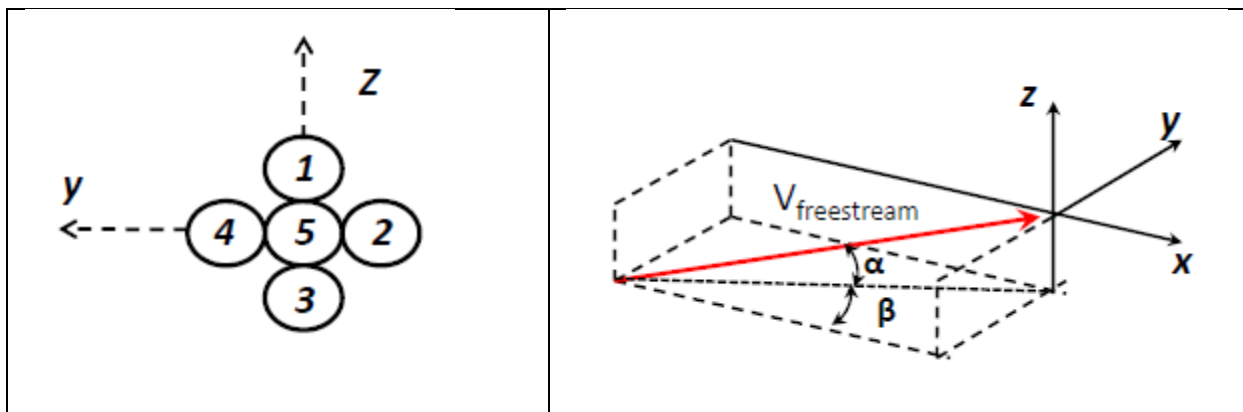


FIGURE 88: FRONT VIEW

FIGURE 89: VELOCITY ANGLE RELATIVE TO PRESSURE PROBE

1. Calculate the minimum and average pressures:

$$p_{min} = \min(\Delta p_1, \Delta p_2, \Delta p_3, \Delta p_4) \quad \text{EQUATION 0.1}$$

$$p_{average} = \frac{(\Delta p_1 + \Delta p_2 + \Delta p_3 + \Delta p_4)}{4} \quad \text{EQUATION 0.2}$$

2. Calculate various coefficients:

$$F_A = \frac{\Delta p_3 - \Delta p_1}{\Delta p_5 - \Delta p_{min}} \quad \text{EQUATION 0.3}$$

$$F_P = \frac{\Delta p_2 - \Delta p_4}{\Delta p_5 - \Delta p_{min}} \quad \text{EQUATION 0.4}$$

3. Perform a bi-linear interpolation with  $F_A$  and  $F_P$  in calibration graph, Figure 90, to obtain  $\alpha$  and  $\beta$ .
4. Perform a bi-linear interpolation with  $\alpha$  and  $\beta$  in calibration graph, Figure 91 and Figure 92, to obtain the values of  $F_Q$  and  $F_H$ .

5. Calculate the dynamic and total pressure present at the tip of the probe with Equation 0.5 and Equation 0.6 respectively.

$$q_{tip} = \frac{\Delta p_5 - p_{average}}{F_Q} \quad \text{EQUATION 0.5}$$

$$P_{Tot,tip} = F_H(\Delta p_5 - p_{min}) + \Delta p_5 - p_{ref} \quad \text{EQUATION 0.6}$$

6. From the values calculated in Equation 0.5 the total velocity present at the tip of the probe can be calculated with Equation 0.7.

$$V = \sqrt{\frac{2}{\rho} q_{tip}} \quad \text{EQUATION 0.7}$$

7. The last step consists of converting the velocities in the proper reference plane.

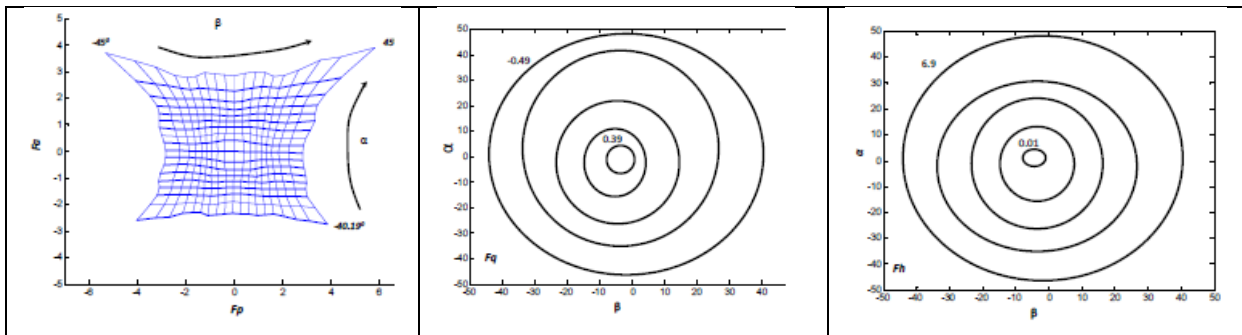


FIGURE 90: CALIBRATION GRAPH A

FIGURE 91: CALIBRATION GRAPH B

FIGURE 92: CALIBRATION GRAPH C

## APPENDIX C: AXIAL MOMENTUM MODEL FOR BARE TURBINES

Wind consists of moving particles, one of the basic laws in physics shows that moving particles are energy carriers, more specifically, carriers of kinetic energy:

$$E_{kin} = \frac{1}{2} m U_{\infty}^2 \quad \text{EQUATION 0.8}$$

When looking at the mass flow, the power available in the wind will be:

$$\dot{m} = \rho A_{rotor} U_{\infty} \quad \text{EQUATION 0.9}$$

$$P_{available} = \frac{1}{2} \rho A_{rotor} U_{\infty}^3 \quad \text{EQUATION 0.10}$$

Not all of this power can be captured, because the wind still has a velocity behind the rotor. If all the power available will be captured, there should be no wind behind the rotor. Physically this is impossible. This limitation is known as the Betz limit and can be explained with an actuator disc model [39]. Figure 93 shows a stream tube model for the flow approaching and passing a wind turbine, modeled by a permeable actuator disc, exerting a force on the flow. The control volume is limited by the dashed lines.

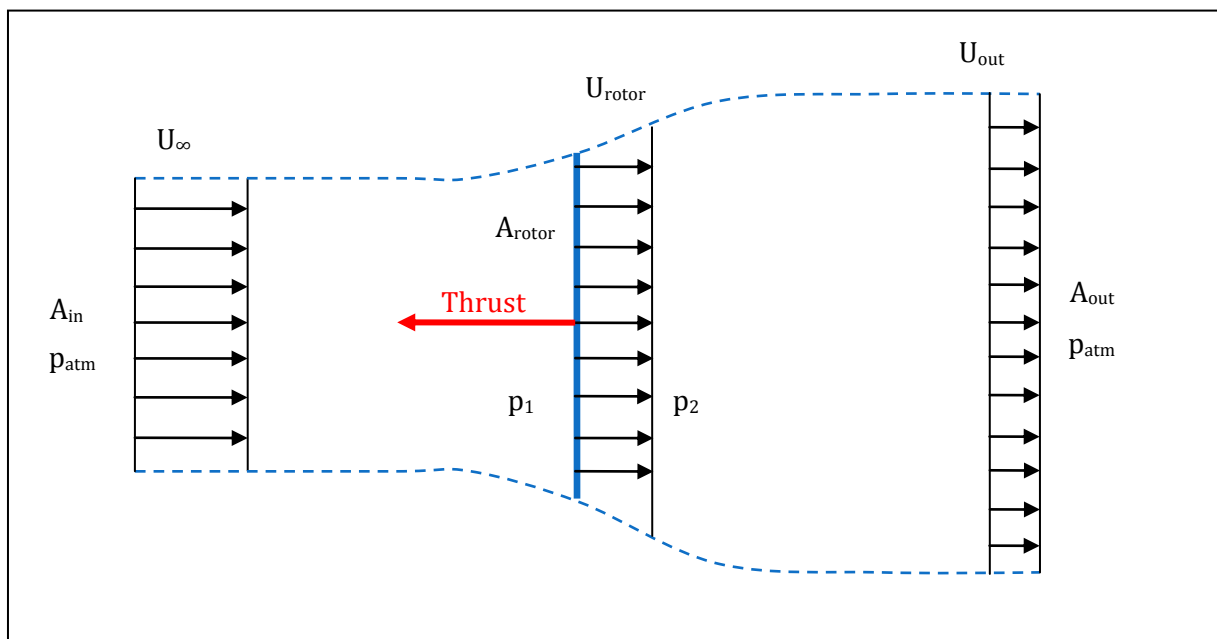


FIGURE 93: ACTUATOR DISK MODEL (THE BLUE LINE IS THE DISK)

The power that the turbine harvests from the incoming wind depends on the force exerted by the actuator disc on the incoming flow:

$$P_{captured} = T U_{rotor} \quad \text{EQUATION 0.11}$$

Momentum theory shows that the thrust exerted on the flow by the rotor is due to velocity and thus pressure difference. Assuming incompressible flow, the following continuity equation holds.

$$U_{\infty}A_{in} = U_{rotor}A_{rotor} = U_{out}A_{out} \quad \text{EQUATION 0.12}$$

Momentum is conserved within the stream tube, thus:

$$\Delta M = T \quad \text{EQUATION 0.13}$$

$$\Delta M = \rho A_{in} U_{\infty}^2 - \rho A_{out} U_{out}^2 \quad \text{EQUATION 0.14}$$

With Equation 0.12 this yields:

$$T = \rho A_{rotor} U_{rotor} (U_{\infty} - U_{out}) \quad \text{EQUATION 0.15}$$

When applying Bernoulli's law to find an equation for the pressure difference over the actuator disc first the pressure difference just in front of the actuator disc can be found and secondly the pressure difference just behind the actuator disc:

$$p_{atm} + \frac{1}{2} \rho U_{\infty}^2 = p_1 + \frac{1}{2} \rho U_{rotor,1}^2 \quad \text{EQUATION 0.16}$$

$$p_{atm} + \frac{1}{2} \rho U_{out}^2 = p_2 + \frac{1}{2} \rho U_{rotor,2}^2 \quad \text{EQUATION 0.17}$$

Combining Equation 0.16 and Equation 0.17 and assuming that  $U_{rotor,1} = U_{rotor,2}$  gives:

$$(p_1 - p_2) = \frac{1}{2} \rho (U_{\infty}^2 - U_{out}^2) \quad \text{EQUATION 0.18}$$

A pressure difference exerted on a surface results into a force:

$$T = (p_1 - p_2) A_{rotor} = \frac{1}{2} \rho A_{rotor} (U_{\infty}^2 - U_{out}^2) \quad \text{EQUATION 0.19}$$

Combining the two equations obtained for the thrust force; Equation 0.15 and Equation 0.19 gives:

$$U_{rotor} (U_{\infty} - U_{out}) = \frac{1}{2} (U_{\infty}^2 - U_{out}^2) \quad \text{EQUATION 0.20}$$

$$U_{rotor} = \frac{1}{2} (U_{\infty} + U_{out}) \quad \text{EQUATION 0.21}$$

Introducing the axial induction factor  $a$  gives:

$$a = 1 - \frac{U_{rotor}}{U_{\infty}} \quad \text{EQUATION 0.22}$$

$$U_{rotor} = U_{\infty}(1 - a) \quad \text{EQUATION 0.23}$$

With this the thrust force becomes:

$$T = \frac{1}{2} \rho A_{rotor} U_{\infty}^2 4a(1 - a) \quad \text{EQUATION 0.24}$$

Using this result in Equation 0.11 and combining with Equation 0.23 gives:

$$P_{captured} = \frac{1}{2} \rho A_{rotor} U_{\infty}^3 4a(1 - a)^2 \quad \text{EQUATION 0.25}$$

Dividing Equation 0.25 by Equation 0.10 gives an equation for the power coefficient:

$$C_p = \frac{P_{captured}}{P_{available}} = 4a(1 - a)^2 \quad \text{EQUATION 0.26}$$

The maximum efficiency will occur when the induction factor,  $a$ , is equal to  $\frac{1}{3}$ . The efficiency is then  $\frac{16}{27} = 59\%$ . This is known as the Betz limit of a wind turbine. It is the theoretical maximum efficiency of a horizontal axis wind turbine [39].

The thrust coefficient at which a bare turbine operates most efficient is calculated accordingly:

$$C_T = \frac{T}{\frac{1}{2} \rho A_{rotor} U_{\infty}^2} = 4a(1 - a) \quad \text{EQUATION 0.27}$$

So a bare turbine operates most efficient at a thrust coefficient of  $\frac{8}{9}$ .

## APPENDIX D: TEST OVERVIEW

Date	Measurement	Blade	Remarks
19-jul-10	Power	Optimal	
20-jul-10	Power	Optimal	
21-jul-10	Power	Optimal	
22-jul-10	Power	Old	
23-jul-10	Power	Old/Linear	
26-jul-10	Power	Linear	
27-jul-10	Power/Velocity	Linear	
28-jul-10	Velocity	Linear	DONQI tests with new gen
29-jul-10	Velocity	Linear	Build up original set-up
30-jul-10	Velocity	Old	
2-aug-10	Velocity	Old/Empty/Optimal	Remarkable change in power/velocities.
3-aug-10	Velocity/Power	Linear (velocity) / Swept and Optimal (power)	
4-aug-10	Power	Swept/Linear	
5-aug-10	Power	Optimal	
6-aug-10	Power	Old	

APPENDIX E: GENERATOR TEST

Tests on lathe-machine.

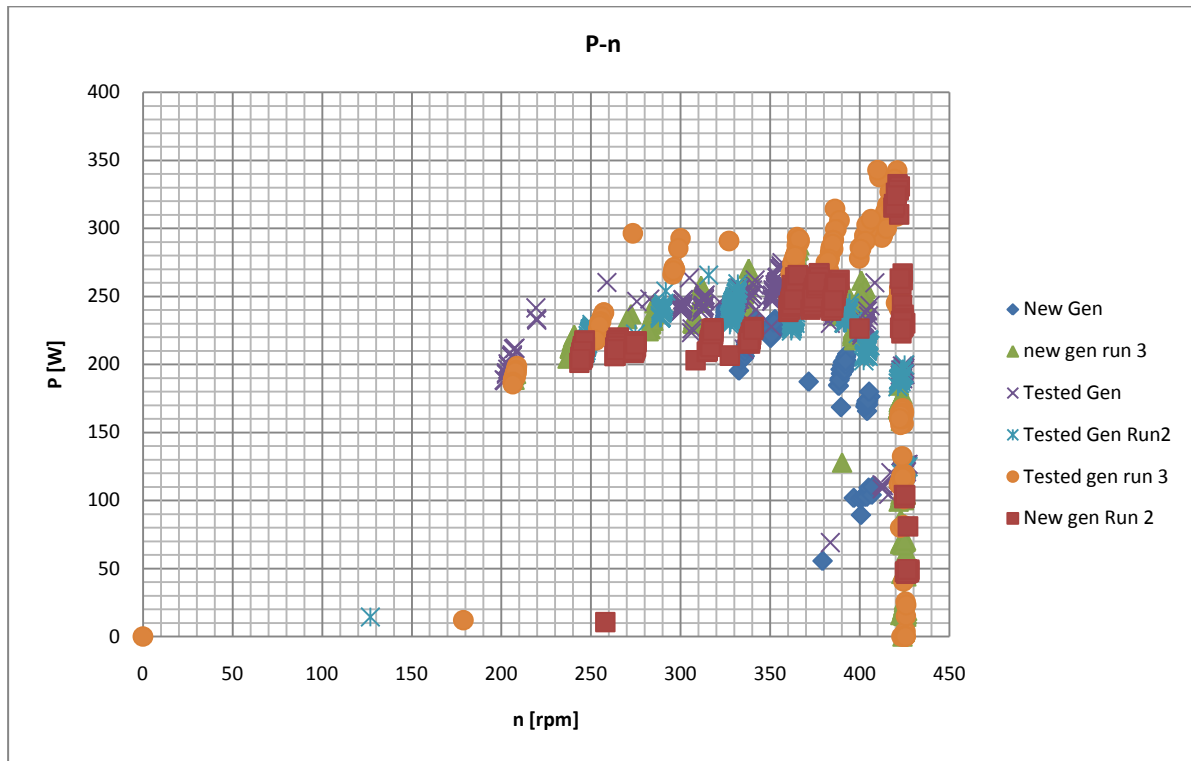


FIGURE 94: POWER-RPM PLOTS FOR THE TESTED GENERATOR AND ANOTHER GENERATOR

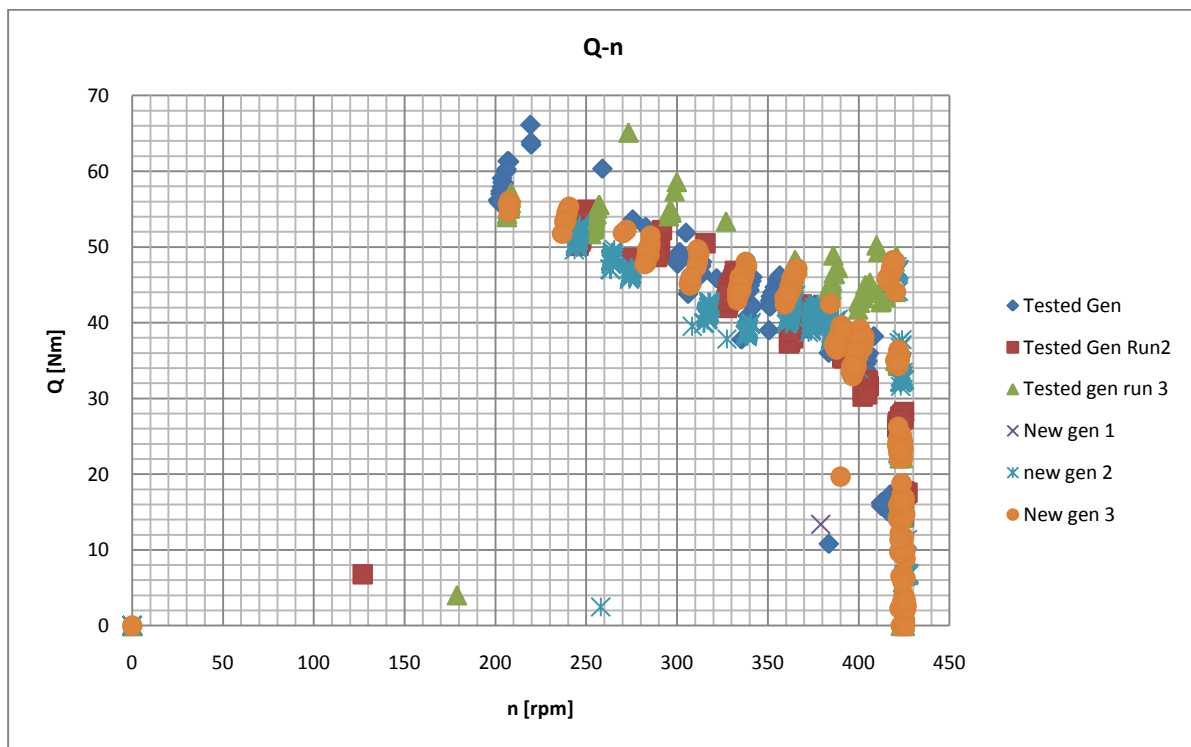


FIGURE 95: TORQUE RPM FOR TESTED GENERATOR AND ANOTHER GENERATOR

Tests with actual torque measurements to check difference between generator and software versions (3D skewed was generator in the test):

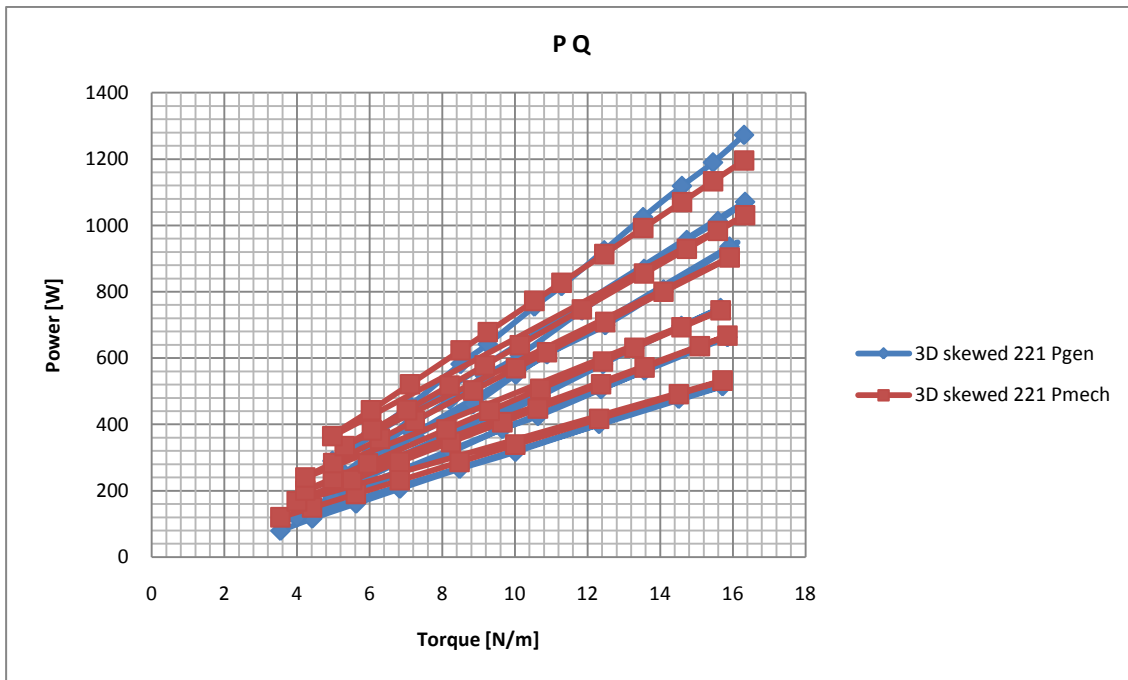


FIGURE 96: DIFFERENCE MEASURED PMECH AND PGEN FOR VARIOUS RPM

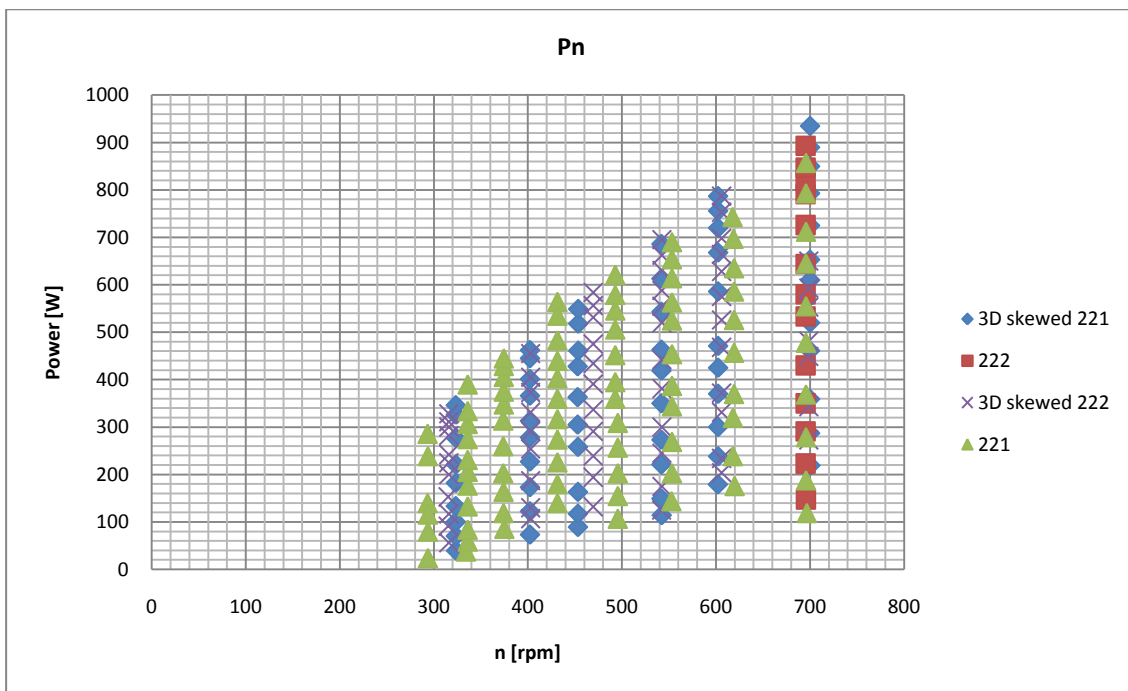


FIGURE 97: PN CURVES FOR DIFFERENT SOFTWARE AND GENERATOR

Both tests excluded that the generator was broken. The last test however had a advantage, since it provided the relationship between the generator power and the mechanical power. This relationship was used to compare the measured generator power to the modeled mechanical power of the rotor blades. To clarify: the generator used was the 3D skewed generator with software version 221.

APPENDIX F: MORE TEST RESULTS

Power measurements Linear Blade

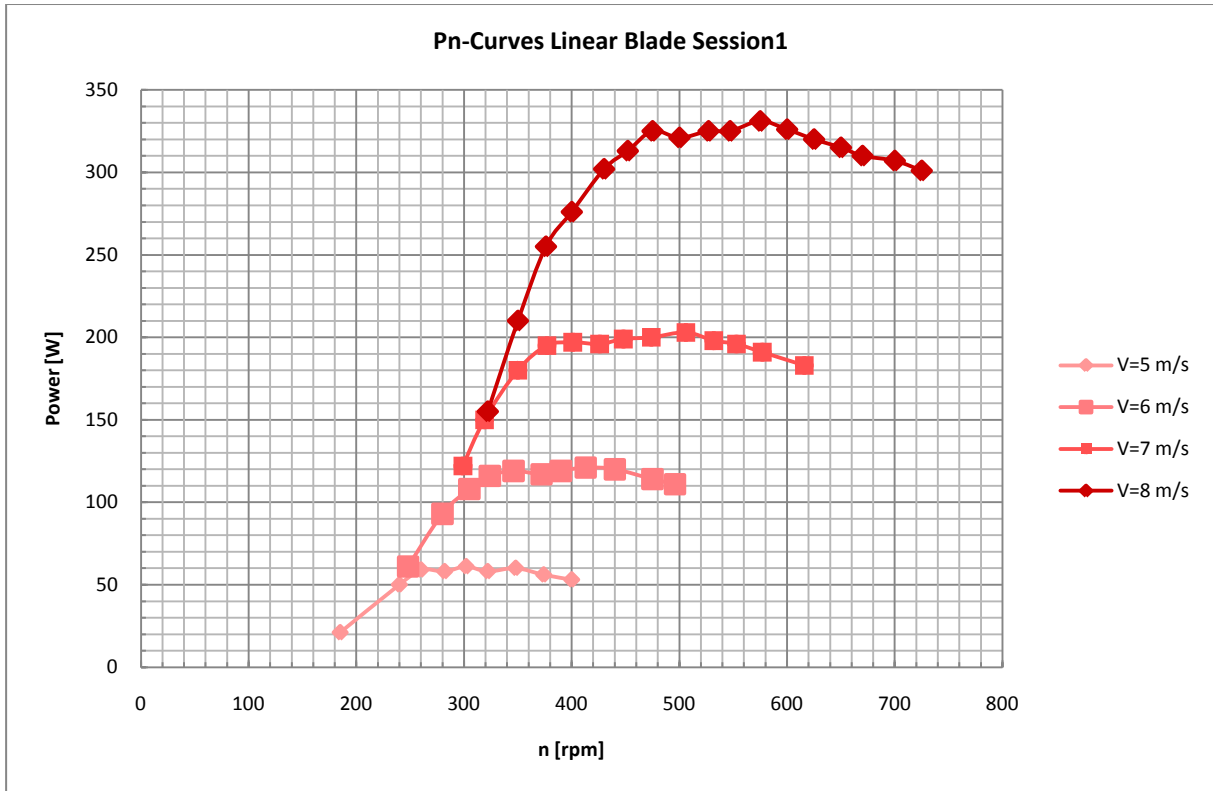


FIGURE 98: PN CURVES LINEAR BLADE SESSION 1 RUN 1

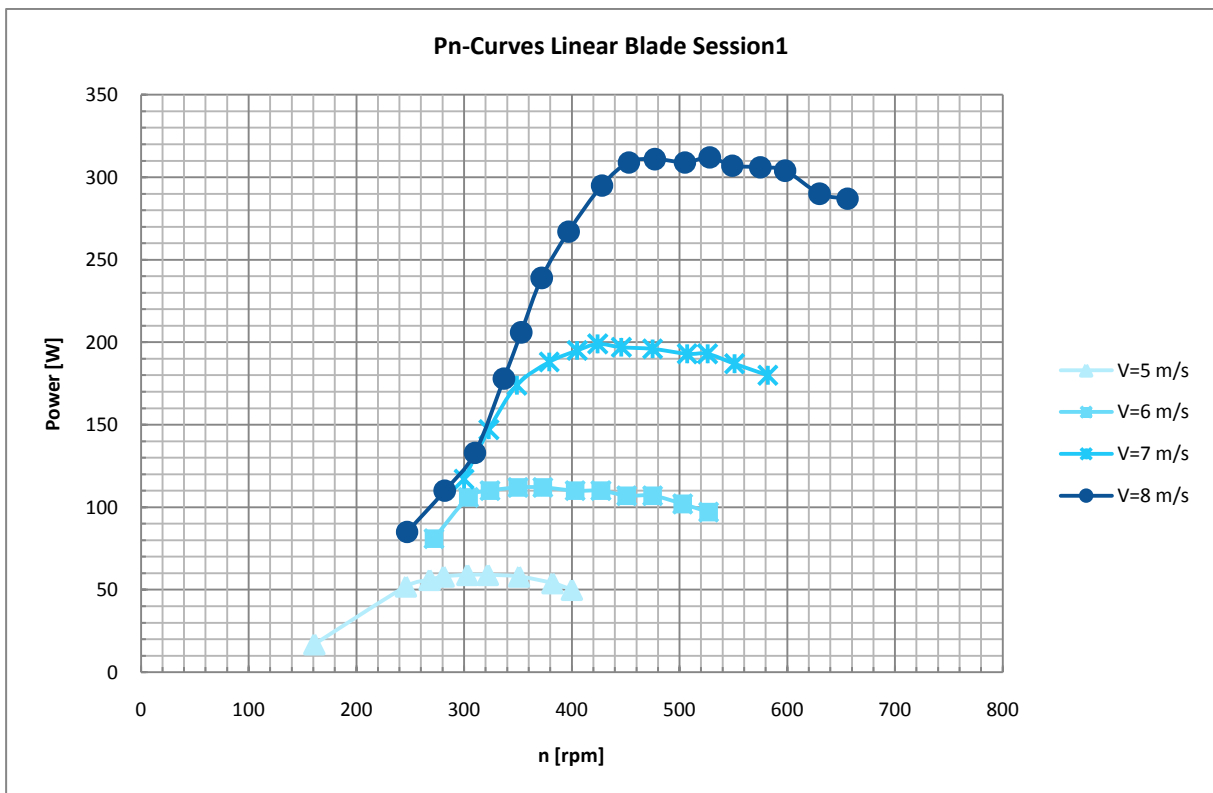


FIGURE 99: PN CURVES LINEAR BLADE SESSION 1 RUN 2

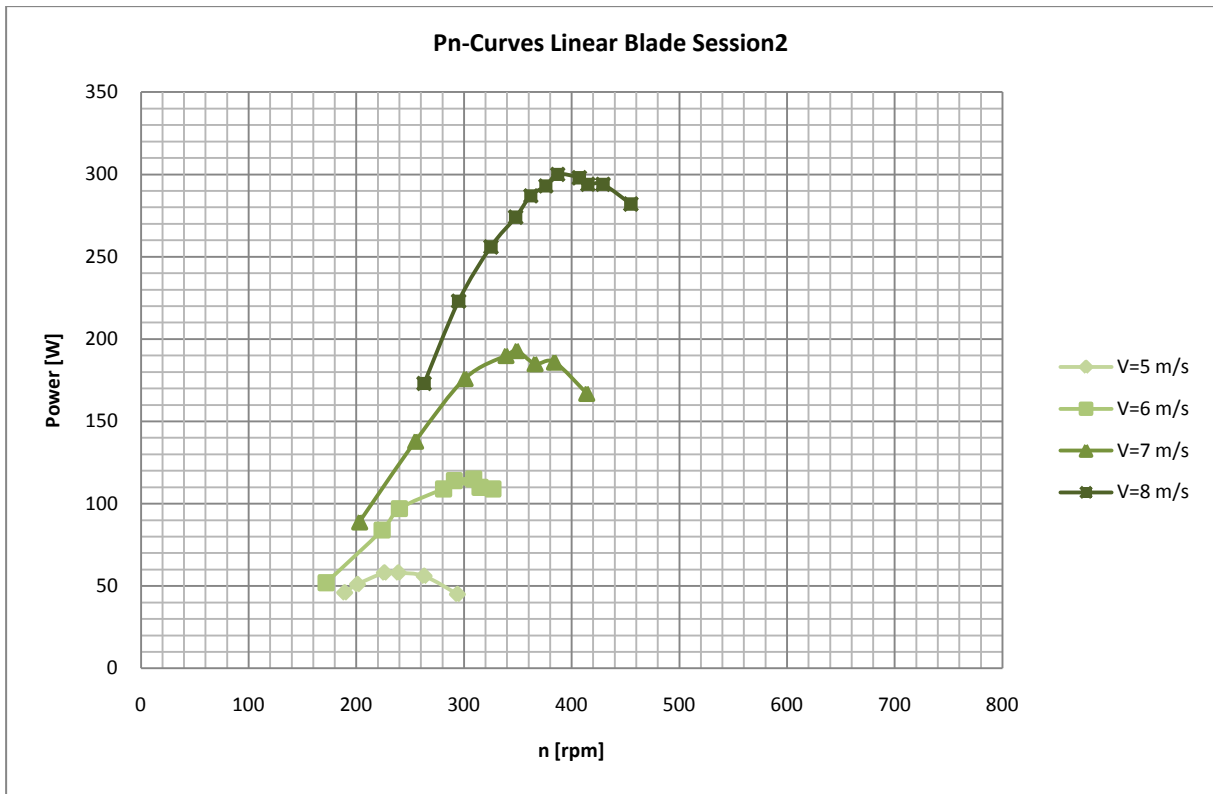


FIGURE 100: PN-CURVES LINEAR BLADE SESSION2 RUN1

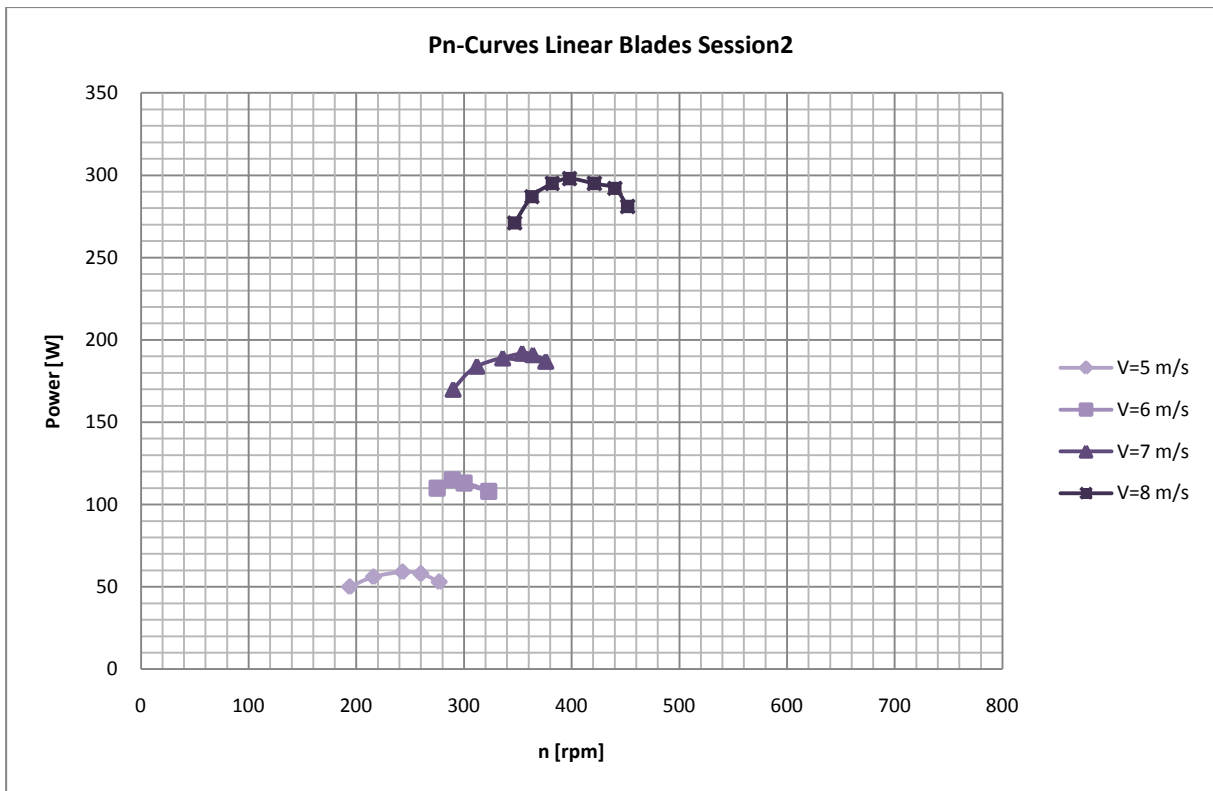


FIGURE 101: PN-CURVES LINEAR BLADE SESSION2 RUN2

Velocity Measurements Old blade

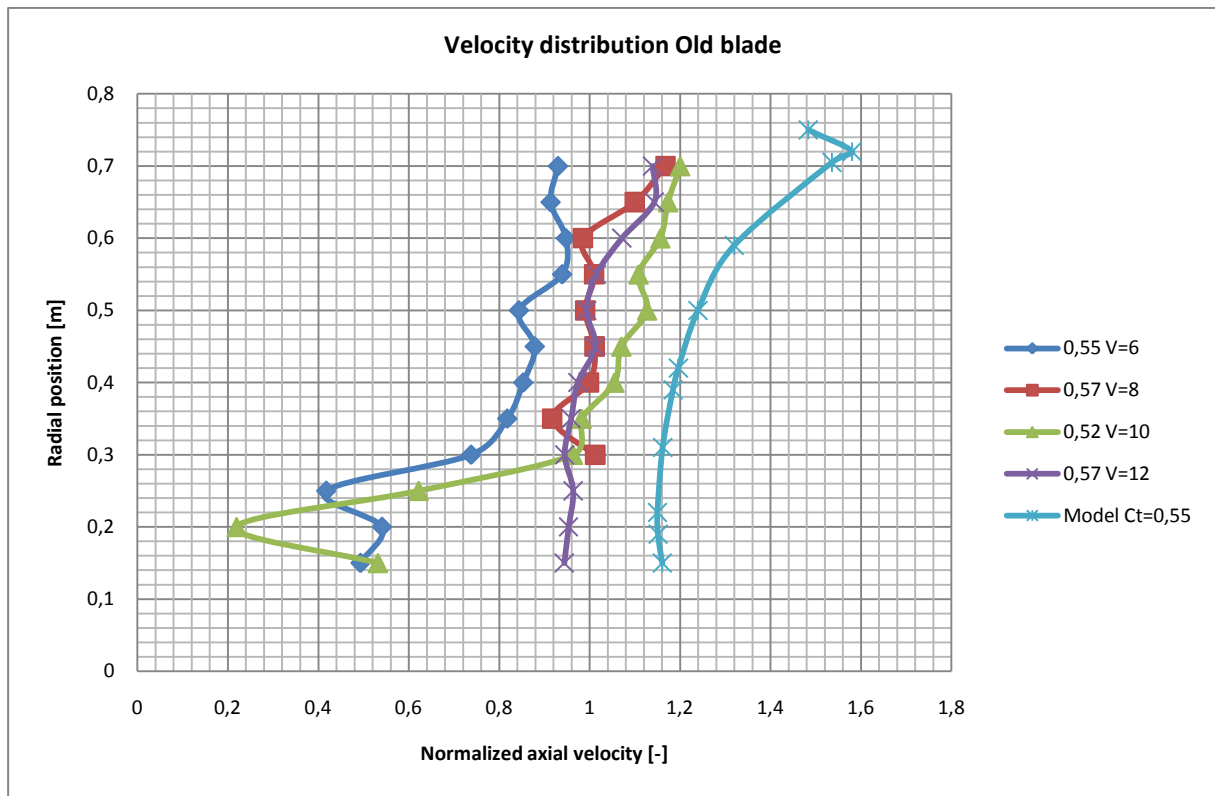


FIGURE 102: VELOCITY DISTRIBUTION OLD BLADE CT=0.55 V=6-12

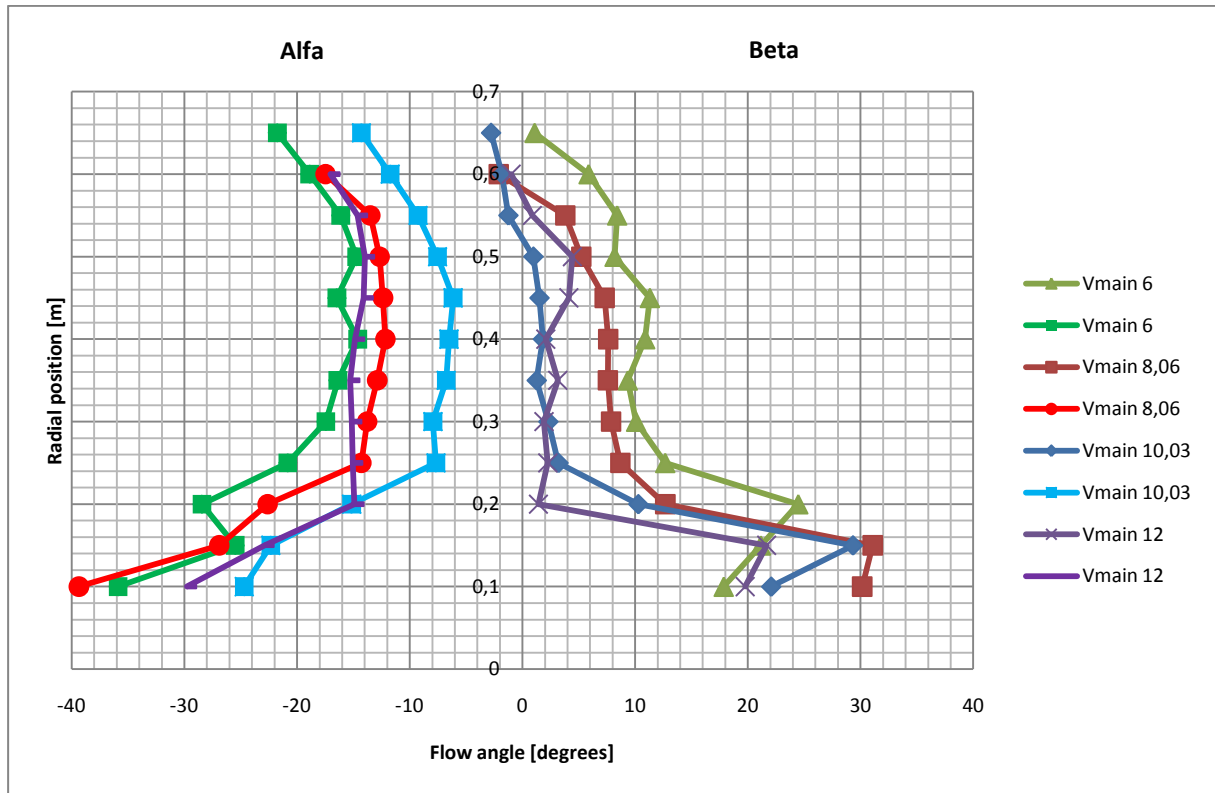


FIGURE 103: FLOW ANGLES OLD BLADE CT=0.55 V=6-12M/S

**Velocity measurements Linear Blade**

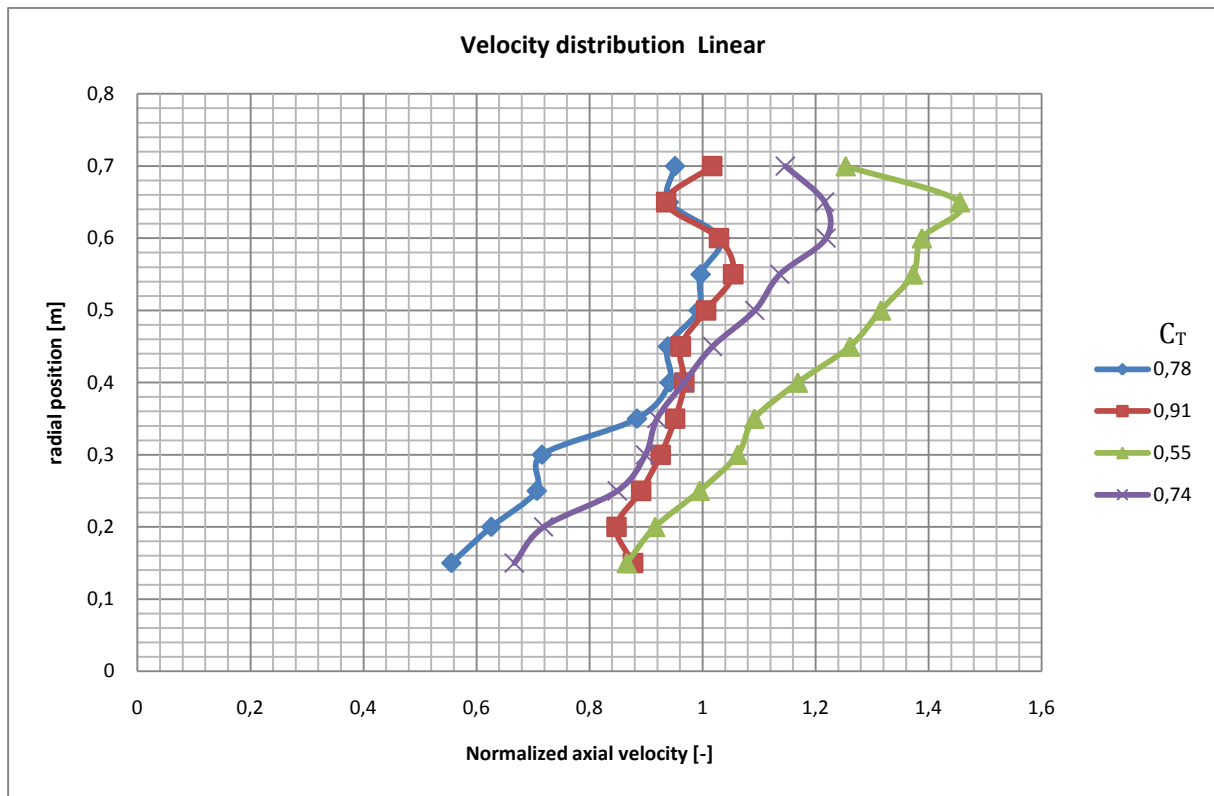


FIGURE 104: VELOCITY DISTRIBUTION LINEAR BLADE, PITCH=12.5

**Velocity Measurements Different blades**

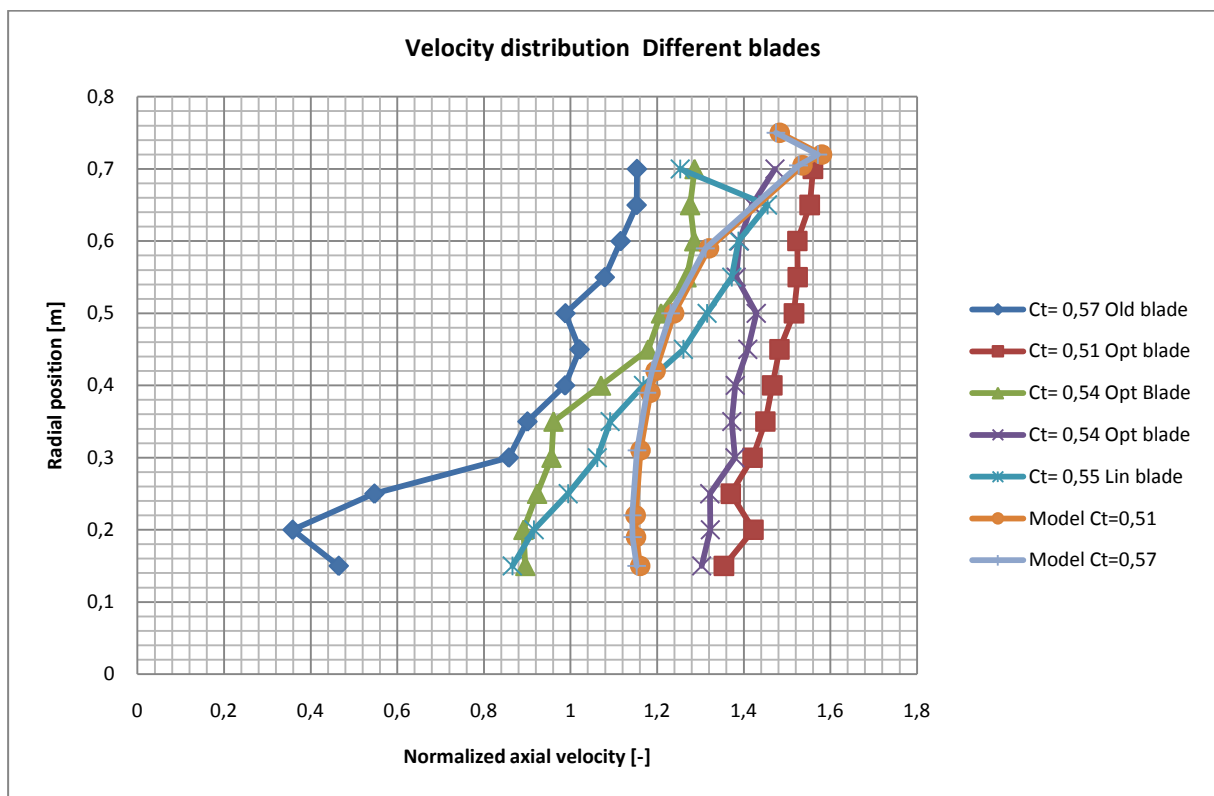


FIGURE 105: VELOCITY DISTRIBUTION DIFFERENT BLADES, CT=0.51-0.57

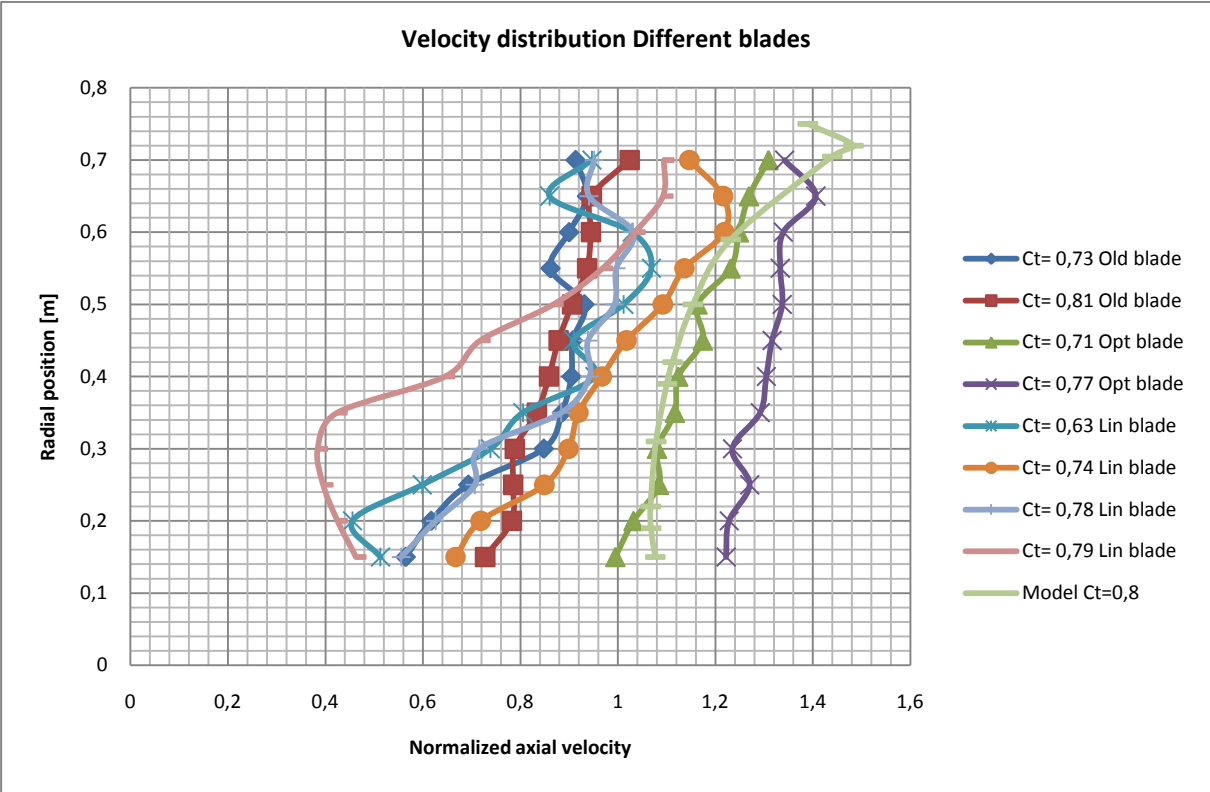


FIGURE 106: VELOCITY DISTRIBUTION DIFFERENT BLADES, CT=0.7-0.9